A First Measurement of the Neutral Current Cross Section at High Q^2 in Longitudinally Polarised e^+p Scattering with the H1 Detector

by

Oliver Michael Henshaw

A thesis submitted to
The University of Birmingham
for the degree of
DOCTOR OF PHILOSOPHY

School of Physics and Astronomy
University of Birmingham
September 2005

Abstract

An analysis is presented of data taken in e^+p collisions at HERA with a longitudinally polarised positron beam at a centre of mass energy of $\sqrt{s} \simeq 320$ GeV. The data were taken in the years 2003 and 2004 and consist of a 20.72 pb^{-1} left-handed sample (with polarisation $P_e = -40.2\%$) and a 26.91 pb^{-1} right-handed sample (with polarisation $P_e = 33.6\%$). The experimental apparatus and the measurement and analysis procedures are described. Particular emphasis is placed on the understanding of the performance of the upgraded H1 detector. The inclusive cross sections for neutral current scattering are presented double differentially in Bjorken x and Q^2 and single differentially in each of these variables. The measurement is made in the range $0.002 < x < 0.65$ and $100 < Q^2 < 20000$ GeV^2. The results are consistent with the predictions of the Standard Model. An asymmetry in the single differential cross sections, $\mathrm{d}\sigma/\mathrm{d}Q^2$, between left-handed and right-handed positron scattering has been measured at the 1σ level in two bins at the highest Q^2, providing tentative confirmation of the polarisation dependence of the neutral current cross section.

for George

A note on contributions by the author

The collaborative nature of modern high energy physics research is such that the analysis presented in this thesis is reliant on the large body of work produced by the H1 collaboration. In particular, the analysis was carried out as part of a larger team within the nELAN physics working group. The hadronic calibration constants were determined by Benjamin Portheault and Emmanuel Sauvan. The final track efficiencies, alignment constants and electromagnetic energy calibrations were calculated in collaboration with Andrey Nikiforov. The generic analysis framework, with which this analysis was developed, was the group effort of the extended H1UK group (in its various incarnations as DUK, DUKz, and MDUK) and was originally designed by Paul Laycock. The studies presented in this work, however, are entirely the work of the author.

A Note on Units

In this work, a system of natural units will be used, whereby $\hbar = c = 1$.

Between October 2001 and September 2004, this work was supported financially by the UK Particle Physics and Astronomy Research Council (P.P.A.R.C.).

"He that breaks a thing to find out what it is has left the path of wisdom."
Gandalf the Grey,
J. R. R. Tolkien, The Lord of the Rings (1954)

Contents

List of Figures

Chapter 1

Introduction

The field of elementary particle physics is concerned primarily with the study of the fundamental constituents of matter and the nature of the interactions between them.

All known matter is built from two types of fermions, the *leptons* and the *quarks*. Leptons exist in three families: the electron (e) and the electron neutrino (ν_e); the muon (μ) and the muon neutrino (ν_μ); and the tau (τ) and the tau neutrino (ν_τ). The quarks likewise fall into three paired groups: down (d) and up (u); strange (s) and charm (c); bottom (b) and top (t).

The fermions interact with each other through the exchange of *gauge bosons*. Four types of interaction are known in nature: these are the gravitational, electromagnetic, weak and strong forces. Gravitation has little or no bearing in the realm of particle physics, since the gravitational interaction is by far the weakest of the four. The electromagnetic interaction is mediated by the photon. The weak interaction involves the exchange of heavy gauge bosons, the Z^0, the W^+ and the W^-. The strong interaction is mediated by gluons. Each of the interactions are characterised by a charge. Quarks are electrically charged, as are the e, μ and τ leptons. The leptons and quarks both carry weak charge. Colour charge, associated to the strong interaction, is carried by quarks and by the gluon itself. The Standard Model of particle physics is built from the unified theory of electroweak interactions together with Quantum Chromodynamics, the theory describing quarks and gluons and the strong interaction.

At the electron-proton collider, HERA, the two experiments H1 and ZEUS study electroweak effects and test Quantum Chromodynamics by probing the structure of the proton at very high energies. The four-momentum transfer, Q^2, between the electron and the proton can be thought of as the resolving power of the electron. Cross sections become very small at large Q^2 such that large luminosities are required for precise measurements.

In this thesis a measurement of the high Q^2 neutral current cross section for the scattering of longitudinally polarised positrons on protons, $\sigma(e^+p \rightarrow e^+X)$, is presented. It is based on data collected by the H1 detector during the years 2003 and 2004. The data consist of a sample taken with left-handed polarised positrons and a sample taken with right-handed polarised positrons. The cross sections measured with the two polarisation values are expected to differ. The coupling of the neutral weak gauge boson, Z^0, to the positron is predicted by the Standard Model to depend on the degree of polarisation. This dependence will only arise, however, at very high Q^2 values comparable to the square of the mass of the Z^0 boson. The asymmetry between the cross sections for left-handed and right-handed positrons is predicted to be dependent on the quark structure of the proton. A measurement of this asymmetry would lead to further insights into proton structure, in particular the rather poorly known ratio of up to down quarks at very large momentum fractions.

In the second chapter of this thesis, the theoretical basis of deep inelastic scattering is reviewed. The cross sections of neutral current scattering and their dependence on the proton structure functions and on electroweak parameters are discussed. In the third chapter, the H1 apparatus is described with particular attention paid to the components used in this analysis. The next two chapters are devoted to Monte Carlo simulation and to the reconstruction of event kinematics. The sixth chapter describes the measurements of the electromagnetic and hadronic energies and the determination of their uncertainties. The seventh and eighth chapters describe the selection and reconstruction of neutral current events. The selection is based on the identification and precise measurement of the scattered electron. Studies of the selection efficiencies and the angular measurement of the scattered electron are presented and the selection criteria reviewed. The subsequent chapter discusses the procedure used to measure the cross section. The penultimate chapter presents the measured cross sections and compares the results for left-handed and right-handed positrons. Finally, the eleventh chapter summaries the work in this thesis and presents an outlook for further improvements and the future prospects of the measurement.

Chapter 2

Theoretical Overview

This analysis is concerned with the measurement of deep inelastic positron proton scattering in which the positron is polarised. The theoretical basics of *ep* deep inelastic scattering (DIS) are discussed in this chapter: a review of the DIS kinematics is followed by a discussion of the relation of *ep* cross sections to the structure functions of the proton with particular emphasis on the case of polarised leptons. These are introduced within the framework of the Quark-Parton Model and the theory of the strong interaction, quantum chromodynamics (QCD). Finally, the evolution of the cross section with the scale is discussed further, and previous fits of parton distributions based on H1 data alone are introduced.

2.1 Deep Inelastic Scattering

DIS is the probing of a nucleon by a lepton, mediated by a gauge boson. The gauge boson coupling to the lepton probes the interior of the proton, and causes it to dissociate. Interactions are classified as either Neutral Current (NC), where the gauge boson is electrically neutral, or Charged Current(CC), involving charged boson exchange. The NC interaction $e^{\pm}p \rightarrow e^{\pm}X$ proceeds either electromagnetically via the photon, γ, or weakly via the massive Z^0 boson. The charged current interaction, $e^{\pm}p \rightarrow \overset{(-)}{\nu}_e X$, is mediated by the weakly interacting $W^{\pm}$ boson. Diagrams for these processes are presented in figure 2.1.

The four-momenta of the particles and particle systems in figure 2.1 are labelled: the four-momenta of the incoming (outgoing) lepton and proton are given by $k(k')$ and $P(P')$,

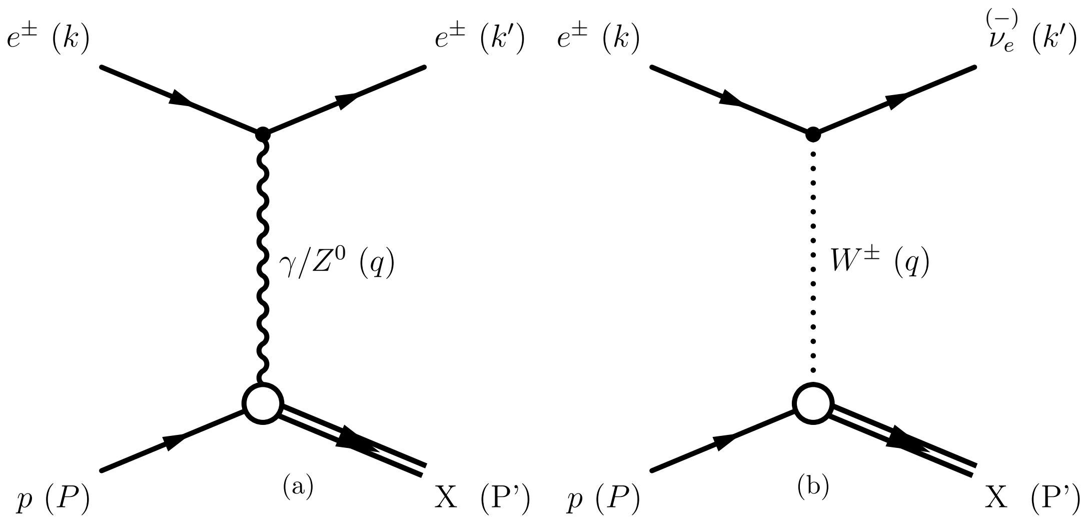

Figure 2.1: Feynman graphs for deep inelastic Neutral Current (left) and Charged Current (right) scattering.

respectively. The exchanged gauge boson carries a four-momentum $q = k - k'$.

The kinematics of DIS at HERA are usually described by the following four variables:

- The four-momentum transfer squared, representing the resolving power of the exchanged boson:
$$Q^2 = -q^2 = -(k - k')^2; \tag{2.1}$$
- The inelasticity, y:
$$y = \frac{P \cdot q}{P \cdot k}, \tag{2.2}$$
which corresponds, in the proton rest frame, to the fraction of the incoming lepton energy carried by the exchange boson;
- The Bjorken scaling variable, x:
$$x = \frac{Q^2}{2P \cdot q}; \tag{2.3}$$
- The centre-of-mass energy squared:
$$s = (k + P)^2 = 4E_eE_p, \tag{2.4}$$
where the masses of the electron and proton are neglected, and where E_e and E_p are the energies of the electron and proton beams.

These kinematic variables are related by $Q^2 = sxy$. With a fixed centre-of-mass energy

($\sqrt{s} \simeq 320$ GeV at HERA), the scattering process can be unambiguously described by two independent kinematic variables. A discussion of kinematic reconstruction methods can be found in chapter 4.

Quark-Parton Model

The Quark-Parton Model (QPM) is the simplest theoretical model in which hadrons, such as the proton, are made up of point-like constituents. These "partons" are identical to the quarks first proposed by Gell-Mann [1]. Deep Inelastic Scattering is interpreted in the QPM as elastic scattering off a quasi-free parton. In the "infinite momentum frame" of the proton, in which quark masses and interactions can be neglected, x is interpreted as the momentum fraction of the proton carried by the struck quark.

Quantum Chromodynamics

The naive Quark-Parton Model is extended by the theoretical framework of Quantum Chromodynamics. QCD is a SU(3) non-Abelian gauge theory describing the interactions of quarks via gluons.

QCD has the following characteristics:

- Each of the quark flavours carries a "colour" charge: denoted as red, green or blue.
- The quarks interact via the exchange of massless bosons known as gluons.
- These gluons carry one of eight different combinations of colour charge and anti-colour charge.
- Since the gluons are themselves coloured, they can self-interact.
- The strong interaction is characterised by the strong coupling constant, α_s.
- Free particles must be colourless; quarks and gluons must be "confined" within bound hadronic states.

The self-interaction of gluons has the consequence that the coupling constant, α_s, depends rather strongly on the characteristic scale of the interaction, μ^2. At large energy scales (corresponding to short distances) the coupling is small. At large distances the coupling strength increases, leading to the confinement of quarks and gluons. The coupling strength, in leading order QCD, is given by:

$$\alpha_s(\mu^2) = \frac{12\pi}{(33 - 2n_f)\ln(\mu^2/\Lambda^2_{QCD})} \tag{2.5}$$

where n_f is the number of active quarks at the energy scale μ^2 and Λ^2_{QCD} is the scale above which perturbative methods can be applied in QCD. The behaviour $\alpha_s \to 0$ as $\mu^2 \to \infty$ is known as "asymptotic freedom". The large energy scale provided by the four-momentum transfer, Q^2, in this analysis means that α_s is small enough that QCD can be treated as a perturbative theory

2.2 Cross Sections and Structure Functions

Deep Inelastic Scattering of leptons from nucleons provides a rich insight into electromagnetic, weak and strong interactions.

2.2.1 Neutral Current Cross Section

The cross section for the neutral current process $e^{\pm}p \to e^{\pm}X$ is given by

$$\frac{\mathrm{d}^2\sigma^{\pm}_{NC}}{\mathrm{d}x\mathrm{d}Q^2} = \frac{2\pi\alpha^2}{xQ^4}\phi^{\pm}_{NC} \tag{2.6}$$

$$\text{with} \qquad \phi^{\pm}_{NC} = Y_+\tilde{F}_2 \mp Y_- x\tilde{F}_3 - y^2\tilde{F}_L \tag{2.7}$$

where $Y_{\pm} = 1 \pm (1-y)^2$ contains the dependence on the inelasticity. The structure function term, ϕ_{NC} is expressed as a linear combination of the generalised structure functions $\tilde{F}_2$, $x\tilde{F}_3$ and $\tilde{F}_L$. The generalised structure function $\tilde{F}_2$ contains contributions from Z^0 exchange (F_2^Z) and γZ^0 interference ($F_2^{\gamma Z}$) as well as pure photon exchange (F_2). In the high Q^2 regime accessible at HERA, the contributions from Z^0 exchange become increasingly important. The structure function $x\tilde{F}_3$ must be introduced due to the parity violating character of the weak interaction. This structure function has contributions from both pure Z^0 exchange ($xF_3^{\gamma Z}$) and γZ^0 interference ($xF_3^{\gamma Z}$). Finally, $\tilde{F}_L$ may be decomposed in a manner similar to $\tilde{F}_2$. This "longitudinal structure function" is zero in the naive QPM, but does contribute, in higher orders of QCD, through gluon radiation.

The contribution of $\tilde{F}_L$ is significant only at high y, due to the factor y^2.

The structure functions for an arbitrary degree of longitudinal lepton polarisation, P[1], can be obtained by the combination of the calculated cross sections for purely left-handed and purely right-handed leptons [2]. The structure function $\tilde{F}_2$ ($x\tilde{F}_3$) can be decomposed into an unpolarised component, $\tilde{F}_2^0$ ($x\tilde{F}_3^0$), and a polarised component, $\tilde{F}_2^P$ ($x\tilde{F}_3^P$), with a linear dependence on P.

$$\tilde{F}_2 = \tilde{F}_2^0 + P\tilde{F}_2^P \tag{2.8}$$
$$\tilde{F}_2^0 = F_2 - \nu_e \chi_Z F_2^{\gamma Z} + (\nu_e^2 + a_e^2)\chi_Z^2 F_2^Z \tag{2.9}$$
$$\tilde{F}_2^P = \mp a_e \chi_Z F_2^{\gamma Z} \pm 2\nu_e a_e \chi_Z^2 F_2^Z \tag{2.10}$$

and

$$x\tilde{F}_3 = x\tilde{F}_3^0 + Px\tilde{F}_3^P \tag{2.11}$$
$$x\tilde{F}_3^0 = \mp a_e \chi_Z xF_3^{\gamma Z} \pm 2\nu_e a_e \chi_Z^2 xF_3^Z \tag{2.12}$$
$$x\tilde{F}_3^P = -\nu_e \chi_Z xF_3^{\gamma Z} + (\nu_e^2 + a_e^2)\chi_Z^2 xF_3^Z \tag{2.13}$$

where

$$\chi_Z = \frac{Q^2}{Q^2 + M_Z^2}\kappa_Z, \quad \kappa_z = \frac{1}{4\sin^2\theta_w cos^2\theta_w} \tag{2.14}$$

contains the Z^0 propagator and θ_w is the Weinberg angle. The axial and vector couplings of the electron[2] to the Z^0, a_e and ν_e are given by the expression for the couplings of fermions:

$$\nu_f = I_{3f} - 2e_f \sin^2\theta_w, \qquad a_f = I_{3f}, \tag{2.15}$$

where I_{3f} is the third component of the weak isospin, and e_f the electric charge, for a fermion f.

In the QPM the structure functions F_2, $F_2^{\gamma Z}$, F_2^Z are related to the sum of the quark (q) and antiquark ($\bar{q}$) parton densities,

$$[F_2, F_2^{\gamma Z}, F_2^Z] = x\sum_q [e_q^2, 2e_q\nu_q, \nu_q^2 + a_q^2]\{q + \bar{q}\} \tag{2.16}$$

[1]The lepton beam polarisation is defined as $P = \frac{N_R - N_L}{N_R + N_L}$, where N_R and N_L are the number of right-handed and left-handed lepton in the beam, respectively.

[2]In this notation, the axial coupling to electrons is given in terms of the e^- coupling: $a_{e^-} \rightarrow a_e = -\frac{1}{2}$ and $a_{e^+} \rightarrow -a_e$.

and the structure functions $xF_3^{\gamma Z}$ and xF_3^Z are related to the difference of quark and antiquark densities, and hence the valence quark densities, q_v:

$$[xF_3^{\gamma Z}, xF_3^Z] = x\sum_q [2e_q a_q, 2\nu_q a_q]\{q - \bar{q}\}. = x\sum_q [2e_q a_q, 2\nu_q a_q] q_v \tag{2.17}$$

Here the summation is over active quark flavours, e_q labels the quark charge, and a_q and ν_q the axial and vector couplings of the quarks to the Z^0, respectively.

Since $I_{3e} = \frac{1}{2}$, the vector coupling of the electron to the Z^0 is small ($\nu_e \simeq 0.04$). Terms containing ν_e in equation 2.8 - 2.13 can be safely neglected at high Q^2. The neutral current DIS cross section for positrons can then be expressed as:

$$\begin{aligned}\frac{\mathrm{d}^2\sigma_{NC}^{\pm}(P)}{\mathrm{d}x\mathrm{d}Q^2} = \frac{2\pi\alpha^2}{x}\Bigg\{ &\frac{1}{Q^4} Y_+ F_2 \mp P a_e \kappa_z \left[\frac{1}{Q^2(Q^2+M_z^2)}\right] Y_+ F_2^{\gamma Z} + a_e^2 \kappa_Z^2 \left[\frac{1}{Q^2+M_Z^2}\right]^2 Y_+ F_2^Z \\ &\pm a_e \kappa_z \left[\frac{1}{Q^2(Q^2+M_z^2)}\right] Y_- xF_3^{\gamma Z} + P a_e^2 \kappa_Z^2 \left[\frac{1}{Q^2+M_Z^2}\right]^2 Y_- xF_3^Z \Bigg\}\end{aligned} \tag{2.18}$$

The charge and polarisation dependencies present in equation 2.18, which arise from the coupling of the Z^0 to the lepton, can be exploited to extract information on the valence quark densities. These effects only become important at very high values of Q^2, comparable with M_Z^2. The techniques used are briefly noted below.

For unpolarised leptons the interference term $xF_3^{\gamma Z}$ enhances the $e^- p$ cross section and reduces the cross section for positrons. The difference between the unpolarised electron and proton cross sections, $\sigma_{NC}^- - \sigma_{NC}^+$ is proportional to $xF_3^{\gamma Z}$, which is dependent on the valence quark densities in the proton (see equation 2.17). This has been measured by H1 at HERA I [3], providing a measurement of valence quark densities down to $x \approx 0.02$. However, the precision of this measurement is limited by the small $e^- p$ sample statistics.

The polarisation asymmetry, $A_\lambda^{\pm}$, between cross sections measured for $P = \pm\lambda$ is approximately proportional to the ratio $F_2^{\gamma Z}/F_2$:

$$A_\lambda^{\pm} = \frac{\sigma_{NC}^{\pm}(\lambda) - \sigma_{NC}^{\pm}(-\lambda)}{\sigma_{NC}^{\pm}(\lambda) + \sigma_{NC}^{\pm}(-\lambda)} \simeq \mp\lambda\chi_Z a_e \frac{F_2^{\gamma Z}}{F_2} \rightarrow \pm\lambda\chi_Z \frac{1 + {}^{d_v}/_{u_v}}{4 + {}^{d_v}/_{u_v}} \tag{2.19}$$

which provides a direct measurement of the ${}^{d_v}/_{u_v}$ ratio for $x \rightarrow 1$, which is so far poorly constrained [4]. The expected size of the charge and polarisation asymmetries is indicated in figure 2.2, which demonstrates the sensitivity of the NC cross section to weak contributions as a function of Q^2 at $x = 0.25$. The size of the weak contributions is shown for electrons and positrons with ±70% polarisation and the statistical sensitivities of each combination of lepton charge and helicity are indicated, with projected samples of 250 pb^{-1}.

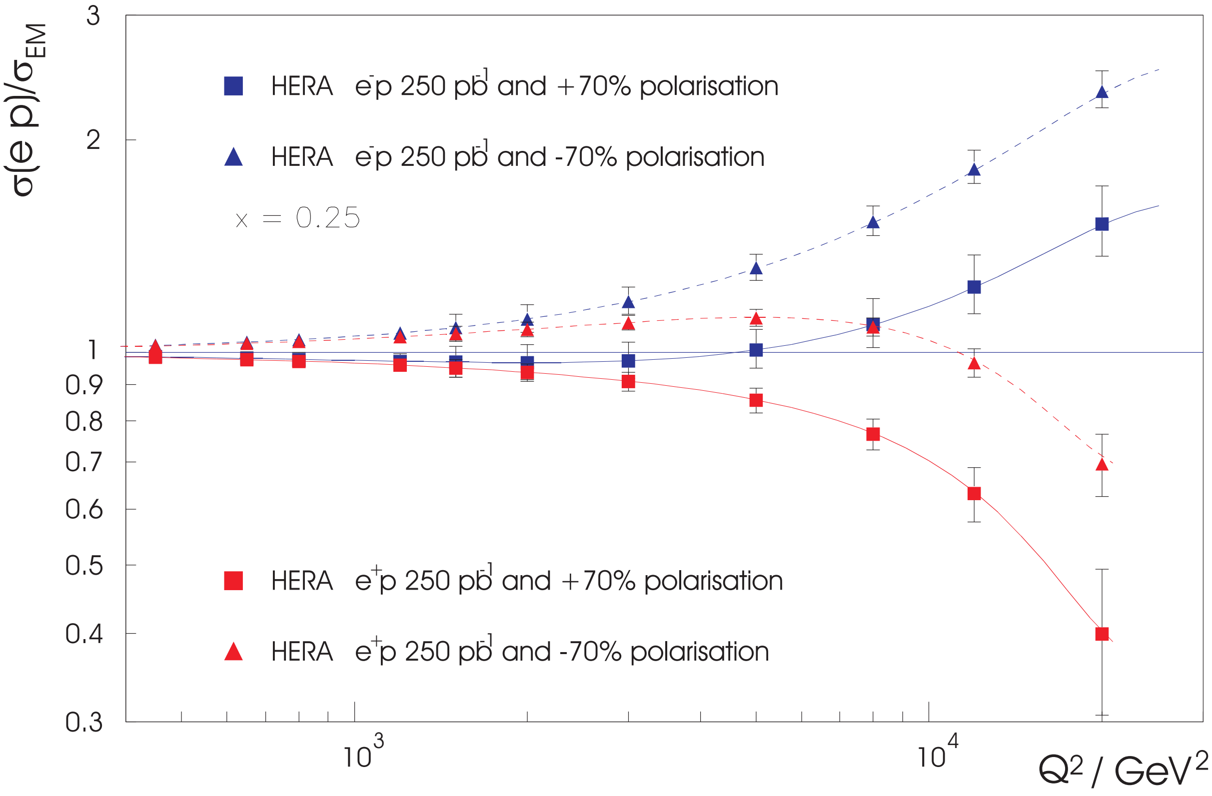

Figure 2.2: The predicted sensitivity of the NC cross section to weak contributions [5]. The ratio of the cross section including Z^0 exchange to that coming from photon exchange alone is shown as a function of Q^2 at $x = 0.25$. All four combinations of lepton charge and helicity are shown.

2.2.2 Charged Current Cross Section

The charged current cross section can be written as

$$\frac{d^2\sigma^{\pm}_{CC}}{dx dQ^2} = (1 \pm P)\frac{\pi\alpha^2}{4x\sin^4\theta_w}\left[\frac{1}{Q^2 + M_W^2}\right]^2 \phi^{\pm}_{CC} \tag{2.20}$$

$$\phi^{\pm}_{CC} = Y_+\tilde{W}_2^{\pm} \mp Y_- x\tilde{W}_3^{\pm} - y^2\tilde{W}_L^{\pm}, \tag{2.21}$$

where M_W is the mass of the W boson and the structure functions $\tilde{W}_2$, $x\tilde{W}_3$, $\tilde{W}_L$ are analogous to the NC structure functions. The coupling term is often written in terms of the Fermi coupling constant, $G_F = \frac{\pi\alpha}{\sqrt{2}\sin^2\theta_w M_W^2}$. The linear polarisation dependence reflects the absence of right-handed charged currents in the Standard Model - the cross sections vanishes for purely right-handed electrons ($P = +1$). This linear dependence on P has already been established by H1 in measurements of the e^-p [6] and e^+p [7] charged current cross sections at several different polarisation values, and by ZEUS [8] [9]. The CC cross section for polarised positrons has been measured at $P = 33 \pm 2\%$ with an integrated luminosity of 15.3 ± 0.4 pb^{-1} and at $P = -40.2 \pm 1.5\%$ with an integrated luminosity of 21.7 ± 0.6 pb^{-1}. The CC cross section for polarised electrons has been measured at $P = -25.40 \pm 0.44\%$ with an integrated luminosity of 17.8 ± 0.2 pb^{-1}. The total CC cross sections are presented in figure 2.3 along with the previous measurements of the e^-p and e^+p cross section with unpolarised leptons [3] and are found to be consistent with the Standard Model prediction of the polarisation dependence calculated from the H1 2000 PDF fit.

Charged Current interactions can also be used to obtain more information on the quark densities in the proton. In the QPM, with $W_L^{\pm} = 0$, the exchanged W boson "picks out" quarks of opposite charge. Therefore, the structure functions are sensitive to sums and differences of quark and antiquark densities, so that:

$$\tilde{W}_2^+ = x(d + s + \bar{u} + \bar{c}) \quad x\tilde{W}_3^+ = x(d + s - \bar{u} - \bar{c}) \tag{2.22}$$

$$\tilde{W}_2^- = x(u + c + \bar{d} + \bar{s}) \quad x\tilde{W}_3^+ = x(u + c - \bar{d} - \bar{s}) \tag{2.23}$$

The charged current cross section then gives information on d at high x in e^+ scattering and on u at high x in e^- scattering.

2.3 Parton Distribution Functions

The parton densities of hadrons cannot be calculated within perturbative QCD. However, it is possible to predict how these parton densities evolve with Q^2 in perturbative QCD. The scale dependence of the parton density functions (PDFs) arises from the self-interaction of quarks and gluons in the strong force: gluon emission from quarks, $q \to qg$, or from gluons, $g \to gg$, or quark pair-production from gluons, $g \to q\bar{q}$. This is described

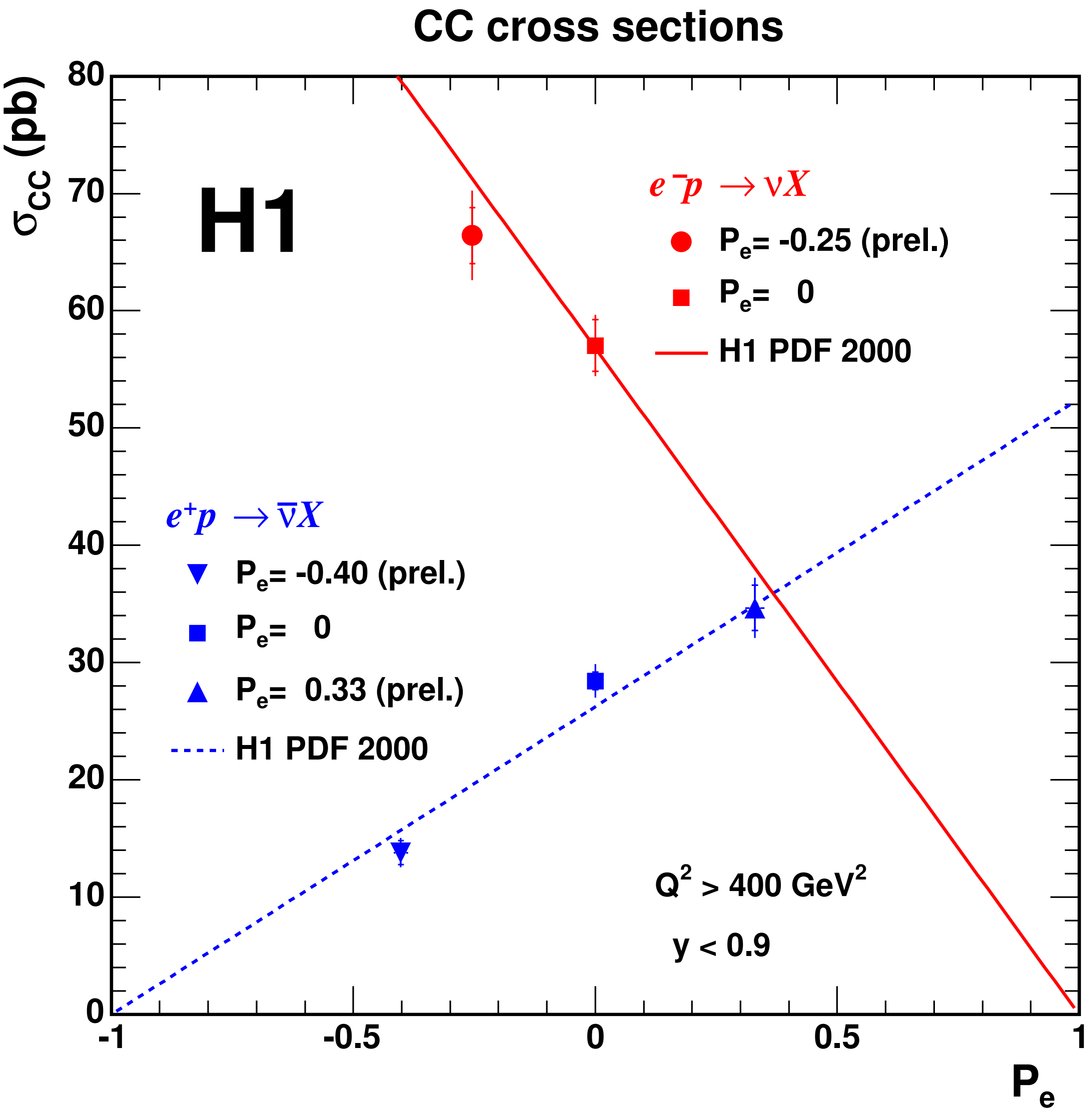

Figure 2.3: The dependence of the $e^{-}p$ and $e^{+}p$ CC cross sections on the lepton beam polarisation, P_e. The data are compared to the prediction from the H1 2000 PDF fit for polarised positrons (dashed line) and polarised electrons (full line)

by the DGLAP [10–13] evolution equations:

$$\frac{\partial q(x,t)}{\partial t} = \frac{\alpha_s(t)}{2\pi} \int_x^1 \frac{dy}{y} \left[q(x,t) P_{qq}\left(\frac{x}{y}\right) + g(x,t) P_{qg}\left(\frac{x}{y}\right) \right] \tag{2.24}$$

$$\frac{\partial g(x,t)}{\partial t} = \frac{\alpha_s(t)}{2\pi} \int_x^1 \frac{dy}{y} \left[q(x,t) P_{gq}\left(\frac{x}{y}\right) + g(x,t) P_{gg}\left(\frac{x}{y}\right) \right] \tag{2.25}$$

at leading order, with $t = \ln(Q^2/\Lambda^2_{QCD})$. Here P_{ij} are the splitting functions, giving the probability for a parton j with momentum fraction y emitting a parton i with momentum fraction x when the scale changes from t to $t + dt$.

The Standard Model cross section predictions used in this analysis are calculated using parton densities obtained from the H1 2000 PDF fit [3]. This is a QCD fit to the unpolarised NC and CC data recorded by H1 at HERA I. As noted earlier, the measurements of neutral and charged current ep scattering are sensitive to quark flavour distributions via the neutral current and charged current structure functions.

By defining sums of up, anti-up, down, and anti-down types of quark distributions,

$$xU = x(u + c) \quad x\bar{U} = x(\bar{u} + \bar{c}) \tag{2.26}$$

$$xD = x(d + s) \quad x\bar{D} = x(\bar{d} + \bar{s}) \tag{2.27}$$

$$\tag{2.28}$$

the equations 2.22 and 2.23 can be re-written as

$$\phi^{+}_{CC} = x\bar{U} + (1 - y)^2 xD \quad \text{and} \tag{2.29}$$

$$\phi^{-}_{CC} = xU + (1 - y)^2 x\bar{D}, \tag{2.30}$$

respectively.

Since the NC cross section is dominated by the electromagnetic structure function F_2 which is, according to equation 2.16, sensitive to the sum of quarks. It can be written

$$F_2 = \frac{4}{9}(xU + x\bar{U}) + \frac{1}{9}(xD + x\bar{D}). \tag{2.31}$$

This choice of parameterisation avoids the need for assumptions about the nature of sea and valence quarks. Thus the valence quark distributions are not fitted directly but are obtained from the difference between quark and antiquark distributions, as obtained from the fits. Figure 2.4 shows parton distributions determined from this fit to H1 data alone, compared with the results of fits to all world data by the MRST [14] and CTEQ [15] groups. The rise of the gluon and the sea quarks at low x can be clearly seen. This rise is much steeper at higher Q^2 and the gluon can be seen to dominate at low x. The contribution from the valence quarks can be seen at $x \approx 0.2 - 0.3$.

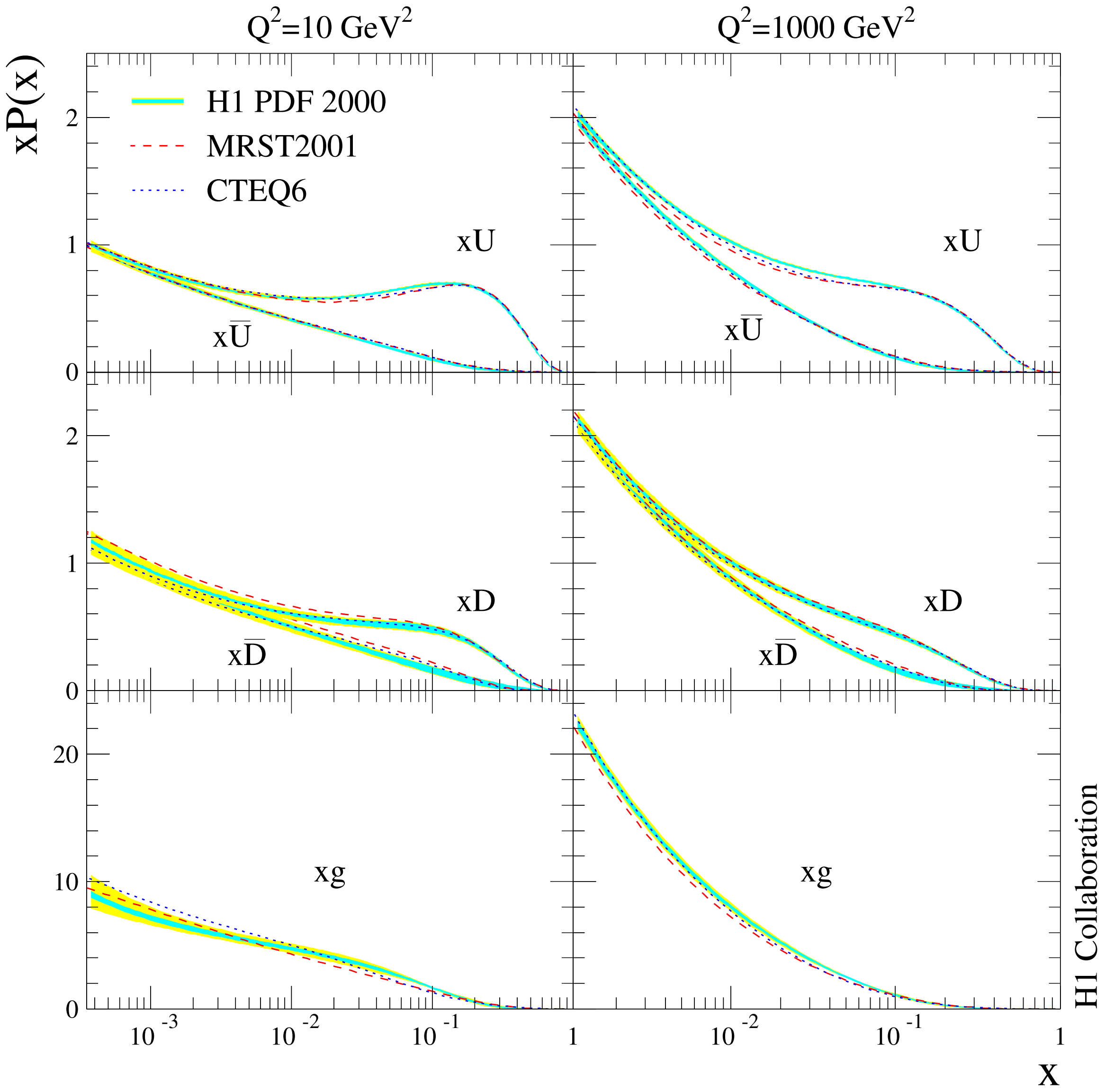

Figure 2.4: Parton distributions determined from the H1 fit to HERA I H1 data alone. Shown from top to bottom are the xU and $x\bar{U}$, xD and $x\bar{D}$, and xg distributions. The distributions are shown at $Q^2 = 10$ GeV^2 (left) and $Q^2 = 1000$ GeV^2 (right). Theoretical predictions from the MRST and CTEQ collaborations are given for comparison.

Chapter 3

The H1 Detector at HERA

3.1 The HERA Ring

HERA, the Hadron-Electron Ring Accelerator, is the world's first and only electron-proton collider. The HERA collider consists of two separate storage rings in which the electrons[1] and protons are accelerated to their respective nominal collision energies and stored. The pre-accelerators PETRA, DESY II and DESY III provide electrons at an energy of 12 GeV and protons at an energy of 40 GeV which are then accelerated to their nominal energies of 27.5 GeV and 920 GeV respectively. The beams are brought into collision at two interaction points (IP) along the ring with a centre of mass energy of 319 GeV. The layout of the HERA accelerator is illustrated in figure 3.1. The electron beam is longitudinally polarised in the region around each of the experimental halls (the polarisation is further discussed in section 3.1.1). The H1 and ZEUS experiments, located in the North and South Halls respectively, are both situated at the interaction points. A fixed target experiment, HERMES, is located in the West Hall. The HERMES experiment is designed to investigate the proton and neutron spin structure functions by colliding the polarised electron beam with a polarised hydrogen, helium or deuterium gas target.

The electrons and protons in the beam are collected into "bunches" to be accelerated to the design energies. The electron beam is made up of 189 (180 for the proton beam) of which 174 are brought into collision at the interaction regions. The remainder, known as "pilot bunches", are not brought into collision but are used to study backgrounds from beam-gas and beam-wall scattering. The bunches, each of which contains of the order of

[1]The term "electrons" will be used to denote both electrons and positrons throughout this thesis, unless otherwise specified.

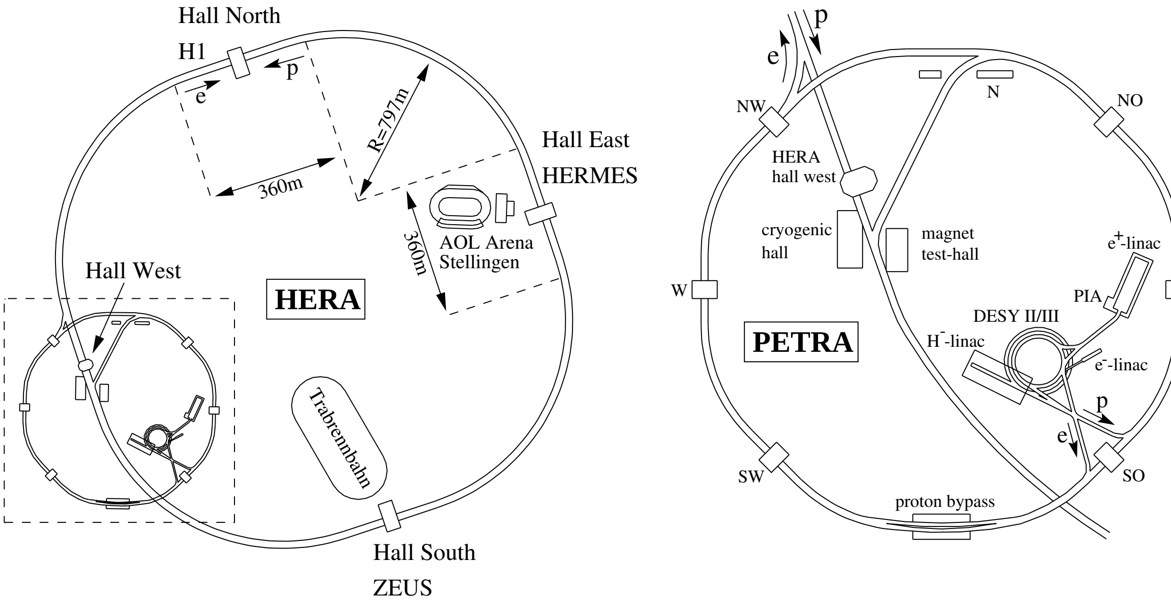

Figure 3.1: The HERA accelerator: the storage ring (left) with the two colliding experiments, H1 and ZEUS, and the fixed target experiment, HERMES, and the an enlarged view of the pre-accelerator (right).

10^{10} particles, are brought into collision every 96 ns, corresponding to a bunch-crossing frequency of 10.4 MHz.

After the conclusion of the HERA I running period in the autumn of 2000, HERA shut down for an extensive upgrade project to increase the specific and instantaneous luminosity delivered by the machine. The instantaneous luminosity, $\mathcal{L}$, is given by

$$\mathcal{L} = \frac{N_p N_e \nu}{2\pi \sigma_x \sigma_y}, \tag{3.1}$$

where N_e and N_p is the number of e and p particles per bunch, ν is the frequency of collision of the bunches and $\sigma_{x,y}$ is the beam cross section. A higher luminosity can be achieved by increasing the number of particles per bunch, N_e or N_p, or by decreasing the cross sectional area of the beams at the interaction point, $\sigma_x \times \sigma_y$. A significant increase in the beam currents was considered and found to be prohibitively challenging [16]. However, a modest increase in the currents was found to be feasible through optimum operation of the HERA accelerator. The design values of the currents at HERA II are $I_e = 55$ mA for the electron beam and $I_p = 135$ mA for the proton beam. The beam cross section was improved by the installation of new superconducting focusing magnets, close to both H1 and ZEUS. Two magnets were installed at H1 to focus the electron beam, one in the (proton) forward region, GO, and one in the backward region, GG. Significant changes had to be made to the inner part of the H1 detector to accommodate the new magnets (see [17] for further details). Section 3.1.2 describes challenges presented by the new HERA geometry around the H1 detector volume.

The beam cross section at the H1 interaction point at the upgraded HERA II is $112 \times 30\ \mu$m for both electrons and protons. The factor 1.5 increase in the maximum beam currents and the factor 2.8 reduction in the beam cross section result in almost a factor five increase in the projected luminosity at HERA II.

3.1.1 Polarisation Measurement

Electrons in a storage ring become transversely polarised through synchrotron radiation in the bending magnets, a process known as the Sokolov-Ternov effect [18]. During the luminosity upgrade for HERA II spin rotators were installed before and after the colliding beam experiments, H1 and ZEUS, to match the spin rotators already installed around HERMES. The rotators provide longitudinally polarised electrons to each of the experiments. The effect of electron beam polarisation on inclusive ep scattering is discussed in section 2.2. The position of the spin rotators and the orientation of the electron polarisation at various points around the HERA ring is illustrated in figure 3.2.

The polarisation is precisely measured at two points along the ring. The Transverse Polarimeter, TPol, measures the transverse polarisation, P_{trans} in the West Hall. The Longitudinal Polarimeter, LPol, measures the longitudinal polarisation, P_{long}, at HERMES. The polarimeters both measure the degree of polarisation via the spin dependent Compton scattering of polarised laser light off the polarised electron beam. The TPol measures spatial asymmetries in the back-scattered laser light and the LPol measures energy asymmetries in back-scattered photons. The polarimeters, described in [19], were modified and upgraded to provide a polarisation measurement with a relative accuracy of 2%. The absolute value of the degree of polarisation is constant everywhere around the ring, $|P_{trans}| = |P_{long}|$. Two independent measurements of the polarisation are necessary, to provide redundancy in the measurement and to explore systematic effects.

3.1.2 Background Conditions at HERA II

The luminosity upgrade described above was achieved partly through the installation of new focusing magnets, GO and GG, close to the IP. The magnets also bend the electron

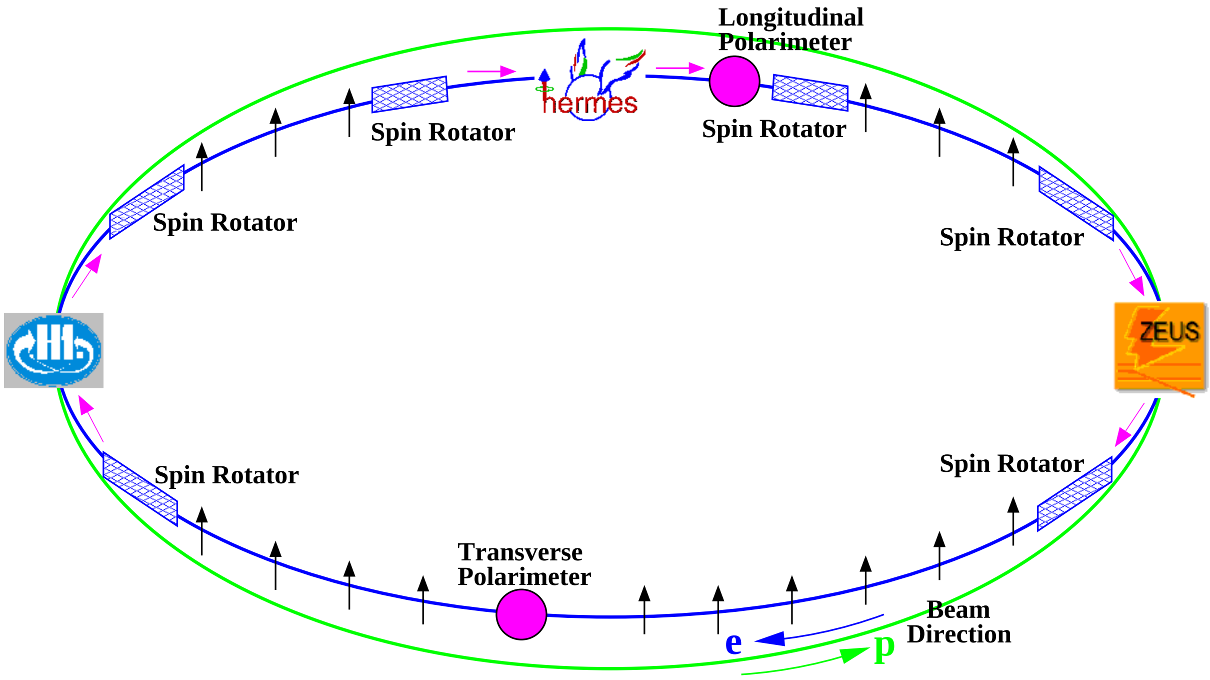

Figure 3.2: The HERA accelerator with the polarimeters TPol and LPol and the spin rotators before and after each of the experiments H1, ZEUS and HERMES. The arrows indicate the orientation of the electron polarisation at each point around the ring.

beam towards the proton beam and then separate them after the interaction point. This procedure prevents the deflection of the electron beam in the GM proton focusing magnets, at ± 10.8 m. The path of the electron beam near the H1 IP is illustrated in figure 3.3 and the resulting synchrotron radiation shown. The electron beam is steered so that no part of any collimator or the beam pipe wall within 10.8 m of the IP is directly hit by synchrotron radiation. However, back-scattered synchrotron radiation primarily from the surface of the GM magnet can enter the H1 detector volume. Additional collimators (C5A and C5B in figure 3.3) were installed to prevent any back-scattered radiation from hitting the H1 detector.

Background rates were higher than expected when HERA was first brought into operation after the upgrade, in 2002. The beam related backgrounds were studied by the collider experiments and by HERA. The causes of the unexpected high backgrounds in the H1 detector are examined in detail in [20] and [21]. The primary source of backgrounds in the H1 detector was identified as proton-gas collisions. Heating from synchrotron radiation and from beam effects at the start of luminosity conditions causes the evaporation of particles from the surfaces of magnets and collimators and from the beam pipe. This

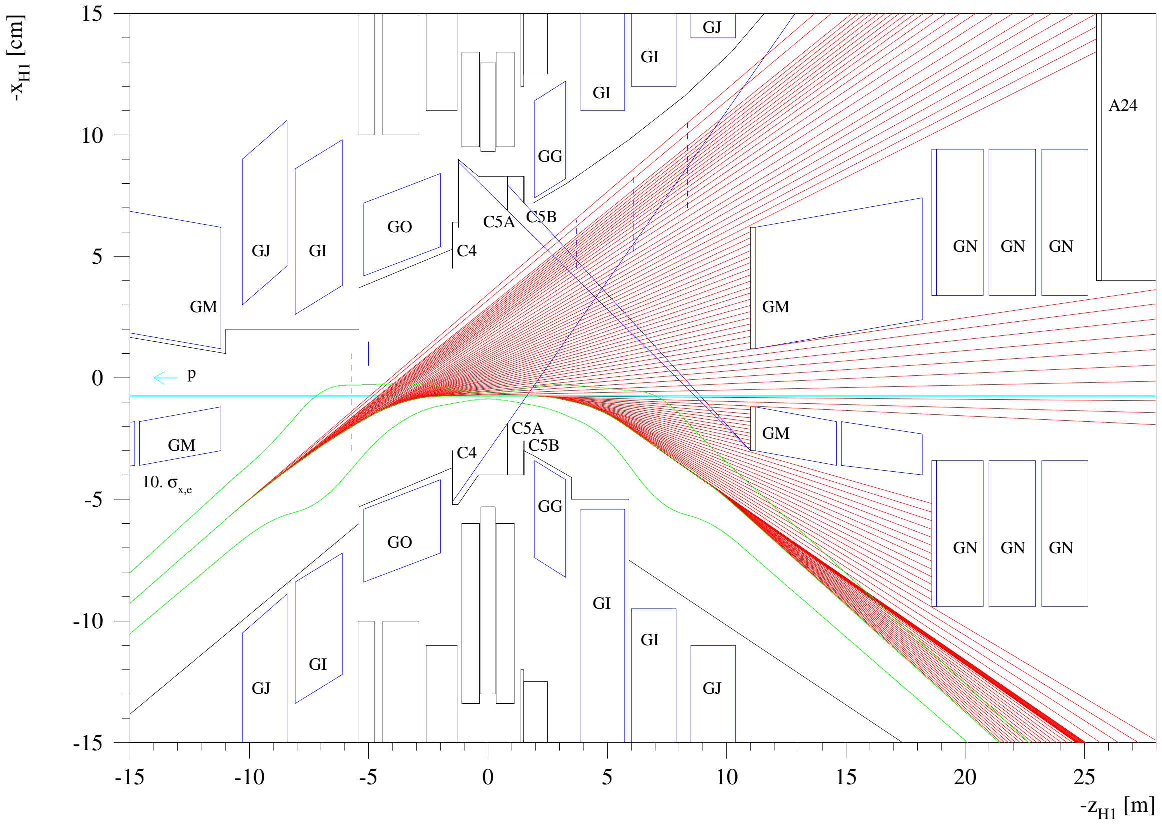

Figure 3.3: Synchrotron radiation in the horizontal plane in the region around the H1 detector. Note the difference in scale between the z axis, defined by the proton beam line, and the x axis, which extends away from the beam axis in the horizontal plane.

causes a deterioration of the vacuum. Protons interact with stray gas particles with a high cross section. Secondary particles from these interactions may re-scatter in the collimators C5A and C5B and enter the detector volume.

Several modifications were made near to the H1 interaction region to reduce the backgrounds before luminosity operation was resumed in the autumn of 2003.

- The collimator C5B was reduced in thickness, decreasing the interaction length for hadrons without compromising the shielding against synchrotron radiation.
- A small amount of lead shielding was installed around the beam pipe to protect the BST from back-scattered synchrotron radiation from the collimators C5A and C5B.
- Pumping around the H1 IP was improved, including the installation of a powerful ion getter pump in the collimator C5B. Residual gas analysers were added to provide

additional feedback on vacuum conditions in the beam.

These actions improved the beam conditions sufficiently that, with constant improvements to the vacuum, data taking close to the HERA II design currents became possible during 2004.

3.2 The H1 Detector

The H1 detector is designed as a general purpose detector to study all aspects of high energy ep scattering. The detector has almost hermetic coverage around the beam axis. A complete description of the H1 Detector can be found in [22] and [23]. The modifications to the detector during the luminosity upgrade are discussed in [16] and summarised in [17].

The H1 detector is cylindrically symmetric about the beam line. Since the incoming proton has a significantly higher momentum than the electron, most particles produced in ep collisions are scattered in the proton direction. The detector is asymmetric in design with finer instrumentation in the "forward" proton direction. Similarly the electron beam direction is referred to as the "backward" direction.

The H1 coordinate system, presented in figure 3.4, is defined relative to the HERA ring: the z axis points along the proton beam direction, the x axis points towards the centre of the ring and the y axis points upwards. The right-handed Cartesian coordinate system thus formed is chosen to have its origin at the nominal interaction point inside the H1 detector. It is sometimes convenient to refer to spherical polar coordinates: the polar angle, θ, is defined relative to the positive z direction and the azimuthal angle, ϕ is defined with respect to the x axis in the xy plane.

A schematic side view of the H1 detector is shown in figure 3.4. The position of the newly installed superconducting focusing magnets, GO and GG, close to the nominal interaction point is shown. The position of the new collimators, C5A and C5B, is indicated. These are designed to protect the H1 detector from back-scattered synchrotron radiation, as discussed in section 3.1.2.

The central tracking system and the forward tracking chambers are arranged around the interaction region with high precision silicon trackers close to the beam pipe. The tracking chambers are surrounded by the liquid Argon calorimeter in the central and forward region, the SpaCal calorimeter in the backward region and the Plug calorimeter, which

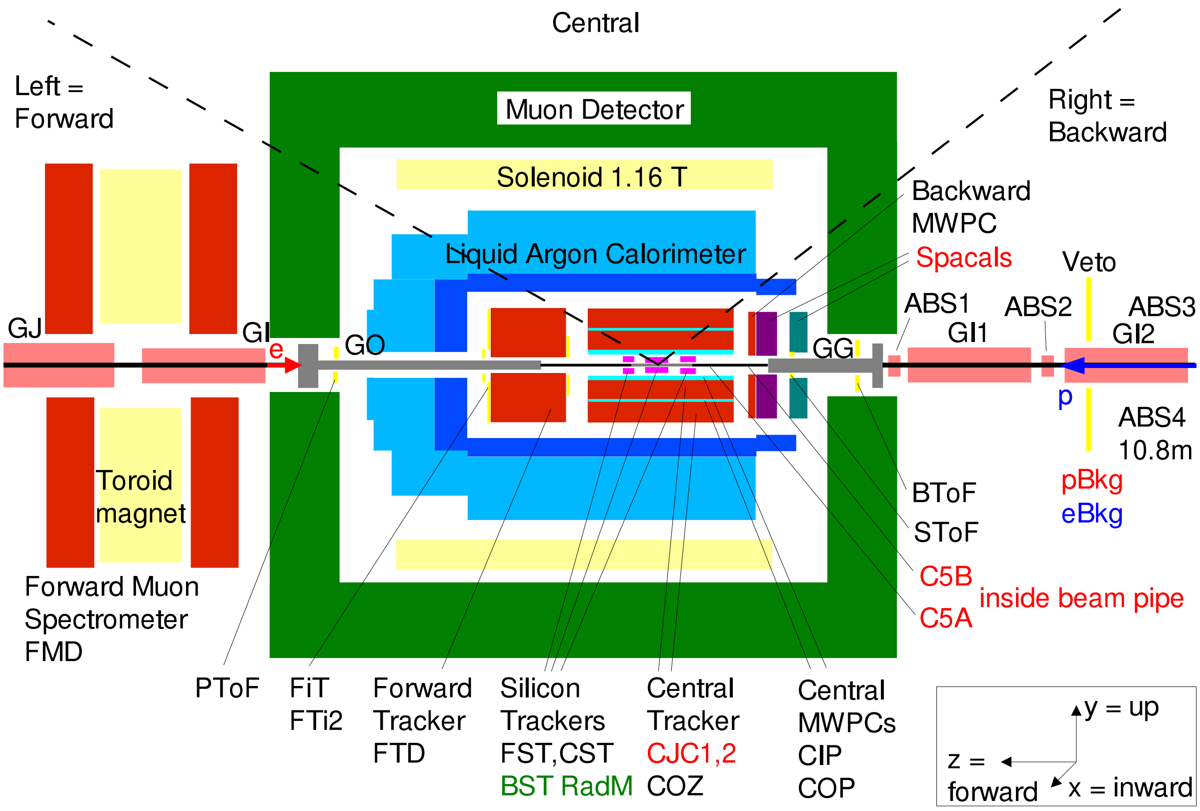

Figure 3.4: A side view of the upgraded H1 detector at HERA II. The final focusing magnets of the electron machine, which extend into the detector volume, are also shown. The H1 coordinate system is indicated in the bottom right.

completes the calorimetric coverage in the forward region. The superconducting solenoid lies outside the calorimeters and provides a 1.15 T field allowing the determination of the momentum of charged particles from the curvature of measured tracks. The iron return yoke of the solenoid is instrumented with streamer tubes that may be used to measure the hadronic energy leakage from the liquid Argon calorimeter and to detect muons. The forward muon detector identifies muons in the forward region. The muon systems will not be discussed further in this thesis. Scintillation counters placed along the beam line make time-of-flight measurements of outgoing particles. The luminosity system is placed upstream in the electron beam (negative z) direction.

3.3 Tracking Chambers

A number of different tracking techniques are used in high energy physics detectors. These are reviewed below and the technical details of some of the tracking detectors in use at

H1 are given.

Silicon Trackers are placed close to the beam pipe in order to precisely measure the *ep* event vertex and to detect secondary vertices. The silicon strip detectors at H1 consist of n-type silicon wafers, etched on one side with thin parallel strips of p-type silicon. A charged particle passing through the wafer creates electron-hole pairs which drift towards the surface on application of a voltage. Since the energy needed to create an electron-hole pair, 3.6 eV, is approximately an order of magnitude smaller than the ionisation energy of a liquid or gas, an adequate signal can be gathered with little sampling material. The low threshold means low noise readout electronics are needed.

Drift chambers consist of anode and cathode wires arranged to create a nearly uniform electric field. Ionisation left by the passage of a charged particle drift in the anode wire plane at nearly constant velocity. A precise spatial measurement is possible in the drift plane through measurement of the electron (and ion) drift velocity. The third space coordinate can be reconstructed by comparing the current read out at both ends of the wire, with a resolution approximately 1% of the wire length. The event timing can be reconstructed from the drift times to the wires.

Proportional chambers provide a fast signal useful for triggering. The multi-wire proportional chambers at H1 consist of many closely spaced anode wires lying between cathode plates. The charged particle ionises the gas as it passes through the chamber. The ionised electrons accelerate towards the closest anode wire, leading to further ionisation and causing an avalanche of secondary ions. The resulting signal is proportional to the initial ionisation. The signals are collected promptly enough for use in triggering and give a spatial precision of the order of the wire spacing (≈ 10 mm).

3.3.1 Silicon Trackers

The Central Silicon Tracker (CST) [24] consists of two layers of silicon strip detectors arranged parallel to the beam pipe. The CST has an angular acceptance of $30° < \theta < 150°$. It was shortened to accommodate the new magnets, GO and GG, in the HERA II upgrade. The CST has an intrinsic resolution of 12 μm in z and 22 μm in the $r - \phi$ plane.

The Backward Silicon Tracker (BST) [25] is intended to improve the reconstruction of the scattered electron at very large polar angles. It has an angular acceptance of $164° < \theta < 76°$. The BST consists of six wheels arranged perpendicular to the beam pipe and has a resolution of 22 μm in r. The BST was redesigned at HERA II to accommodate the new magnets and beampipe.

The Forward Silicon Tracker (FST) [26] was added in the HERA II upgrade in order to improve the tracking in the forward direction. The FST has an angular acceptance of $8° < \theta < 16°$. It consists of five wheels and has a comparable resolution to the BST.

3.3.2 Drift Chambers

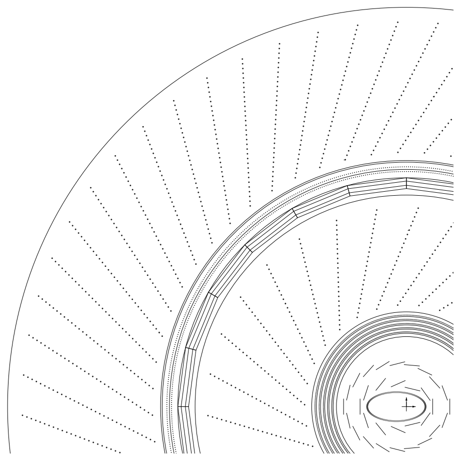

Figure 3.5: An xy view of the H1 Central Tracking Detector at HERA II. Outwards from the elliptical beam pipe are the silicon CST, the CIP2k proportional chamber, the inner jet chamber CJC1, the z chamber COZ, the proportional chamber COP, and the outer jet chamber CJC2.

The Central Jet Chambers [23] are drift chambers with anode sense wires strung parallel to the beam direction. The inner chamber (CJC1) consists of 30 cells with 24 sense wires in each and covers an angular range of $22.5° < \theta < 157.5°$.The outer chamber (CJC2) consists of 60 cells each with 32 sense wires and has an angular acceptance of $39° < \theta < 141°$. The cells are inclined with respect to the radial direction as illustrated in figure 3.5. The CJCs provide an angular resolution of 170 μm in the $r - \phi$ plane and 22 mm in z. The event timing can be determined with a precision of $\approx$ 1 ns from drift times. The CJC allows the measurement of transverse momentum, p_T, with a resolution

$$\frac{\sigma(p_T)}{p_T} = 0.01 p_T \text{ GeV}^{-1}, \tag{3.2}$$

and a measurement of dE/dx with a resolution $\approx 10\%$.

The central outer z chamber (COZ), located between CJC1 and CJC2, can be used to precisely measure the z coordinate. The sense wires in the COZ are mounted perpendicular to the z axis and provide a resolution of $\approx 350\ \mu$m in z.

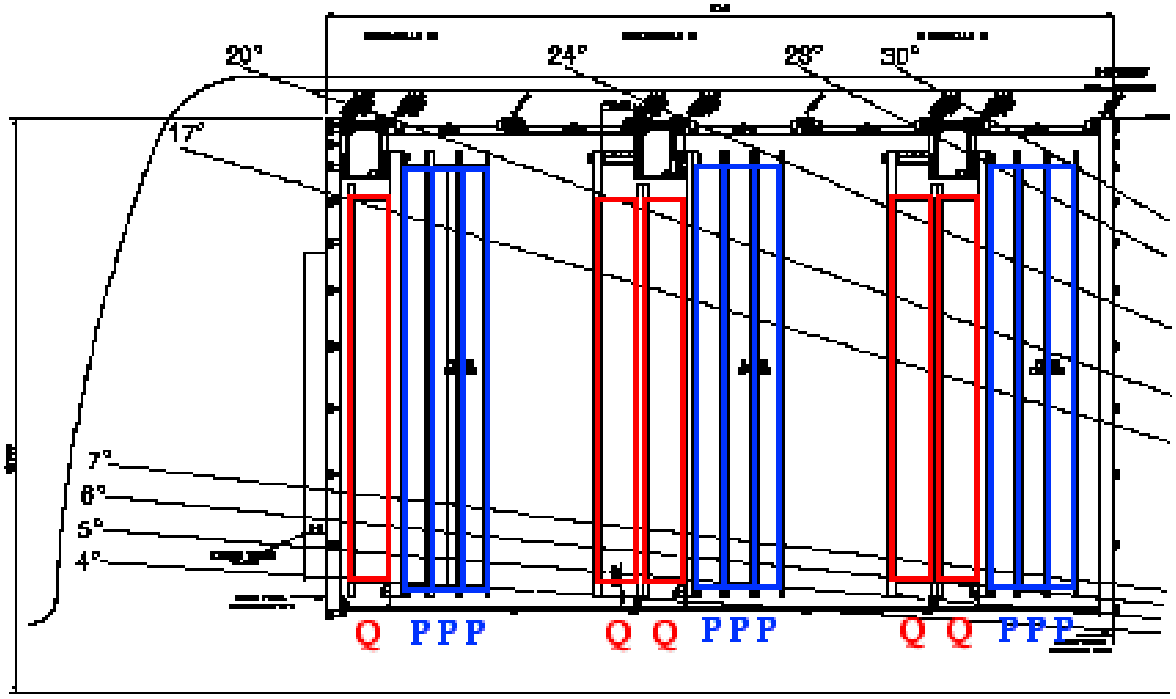

Figure 3.6: A cross section of the Forward Tracking Detector at HERA II in the $r - z$ plane. The old, P, and new, Q, planar drift chambers are labelled.

The Forward Tracking Detector (FTD) extends the tracking coverage of the H1 detector in the forward region, providing a polar angle measurement in the range $5° < \theta < 25°$. The FTD was upgraded for HERA II [27] and consists of nine planar drift 'P' chambers and five new 'Q' chambers collected into three "supermodules", illustrated in figure 3.6. Each supermodule consists of three P chambers, oriented at 0°, 60° and −60°, and two Q chambers (one in the most forward supermodule), oriented at 30° and 90°. The P chambers consist of four layers of wires, each strung in the xy plane, and the Q chambers have eight layers of wires.

3.3.3 Proportional Chambers

The Central Inner Proportional chamber, the CIP2k[2], is the z vertex trigger for the H1 experiment [29]. The CIP provides fast trigger information on the origin of tracks. The track finding performed by the CIP trigger is demonstrated in figure 3.7. Tracks are

[2]The CIP2k replaces the detectors CIP and CIZ [28] at HERA II. For the purposes of this thesis, the acronym CIP refers to the CIP2k.

formed by a combination of hits in up to four layers of the CIP and a line drawn to the beam axis. The z origins of tracks are filled into a histogram with 22 bins. This allows the reconstruction of bins in a range of $\approx$ 380 cm along the z axis (compared to the active length of the CIP of 220 cm). The z resolution of $\approx$ 20 cm is sufficient to identify and reject beam related background originating far from the interaction point (refer to section 3.1.2 for further details). The trigger software is programmable so that the size and position of the z vertex histogram can be adjusted. The CIP trigger logic is discussed in further detail in section 3.7.1.

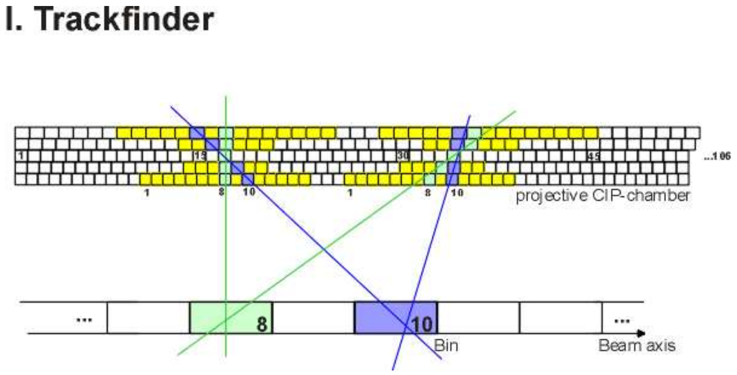

Figure 3.7: The projective geometry of the CIP is shown. The event vertex is reconstructed by building a histogram of the possible z origins of tracks and identifying the event vertex as lying in the bin with the highest population.

The Central Outer Proportional Chamber, the COP, is used in conjunction with the CIP to emulate some of the functionality of the old z vertex trigger at HERA I [30]. The CIP and the COP together can reconstruct the z vertex position with a resolution of $\approx$ 5 cm in a region within $\approx$ 44 cm of the nominal interaction point.

The Backward Proportional Chamber (BPC) consists of three layers of hexagonal proportional chambers overlaid in order to measure the hit coordinate of a particle track with high accuracy. The BPC is installed between the SpaCal and the central trackers.

3.4 Calorimeters

Calorimeters are designed to collect and read out the total energy of incoming particles. They differ from tracking chambers in that they are sensitive to neutral particles. All calorimeters at H1 consist of absorbing material, a sampling medium and a readout system. Incident particles interact with the absorber and produce secondary particles; these interact further in the absorber to produce tertiary particles. The particle cascade, or shower, develops in this way with the initial energy shared over the cascade particles. Finally, the shower particles lose their energy to the sampling medium, causing ionisation or excitation of the atoms; the response of the sampling medium to the shower particles allows a reconstruction of the total energy of the incident particle.

Electrons and photons lose energy in the absorbing material via bremsstrahlung, $ep \rightarrow ep\gamma$, and pair production, $\gamma p \rightarrow e^+e^-p$, respectively. The secondary particles themselves interact electromagnetically; thus showers develop rapidly. The electromagnetic shower development is characterised by the *radiation length*[3], χ_0, of the absorber.

Hadronic particles scatter inelastically from the absorber nuclei. A hadronic shower develops, through subsequent interaction of the secondary particles, with a characteristic length, λ_0. This *interaction length*, analogous to the radiation length, is large compared to χ_0 for the same material. Thus a hadronic calorimeter must extend deeper in the longitudinal dimension than an electromagnetic calorimeter; increased depth provides fuller containment of hadronic showers.

The nature of the interactions of pions in the absorber material determines the progression of the hadronic shower. Charged hadrons, such as the π^+, undergo Coulomb scattering in the absorber; this leads to a lateral spread. On the other hand, an uncharged π^0 can decay to two photons. This leads to a compact electromagnetic component of the hadronic shower. These two effects allow hadronic showers to be topologically distinguished from electromagnetic showers.

Around 30% of the energy of hadronic particles is lost in nuclear excitation and breakup; this energy is not involved in the hadronic shower so that the detector response to hadronic energy is lower than that for electrons. In the absence of a compensation mechanism, the hadronic energy response must be corrected in software [31].

In the H1 detector, the Liquid Argon calorimeter covers the majority of the angular region around the interaction point. This is complemented by the Spaghetti Calorimeter, in the backward region, and the Plug calorimeter in the very forward direction. These detectors allow a total energy measurement over nearly the whole 4π solid angle. The Liquid Argon calorimeter is supplemented by the instrumented iron return yoke of the solenoid. The Iron calorimeter can be used to prevent hadronic energy leakage from the Liquid Argon detector. However, it is not used in this analysis due to its mediocre energy resolution. The Plug Calorimeter, situated near the G0 magnet, provides an angular coverage of

[3]The radiation length is the mean distance over which an electromagnetic particle will fall to $1/e$ of its total energy.

$1.9^\circ < \theta < 3.2^\circ$. This subdetector is not used in this analysis. Neither the Iron nor the Plug will be described in any further detail.

3.4.1 Liquid Argon Calorimeter

The Liquid Argon Calorimeter [32] (often referred to simply as the LAr) provides a coverage of $3^\circ < \theta < 153^\circ$. Liquid Argon based calorimeters are characterised by their stability, homogeneity of response and ease of calibration; in addition, the opportunity for fine segmentation offers excellent e/π separation.

Each cell of the LAr calorimeter comprises plates of absorber material supplemented by High Voltage (HV) electronics and readout electrodes. The rest of the volume of the calorimeter is filled with Liquid Argon; this forms the sampling medium. Particles shower in the absorbing layers and cause ionisation of the Argon. The ionisation is collected by the readout electronics; the total charge obtained can be converted to an energy measurement.

The LAr is divided in z into eight self-supporting wheels; these are illustrated in figure 3.8(a). Each wheel is further divided in azimuthal angle, ϕ, into octants[4] (figure 3.8(b)). The regions between wheels, and between octants, contain dead material; energy losses in these regions are difficult to control experimentally (see section 7.1). The z-cracks and ϕ-cracks, which can be clearly seen as the whitespace in figure 3.8, are positioned to minimise the effect of energy leakage.

The calorimeter wheels each have an electromagnetic section and a hadronic section, with the exception of the BBE (purely electromagnetic) and the OF1/OF2 (purely hadronic) wheels. The electromagnetic section consists of dense lead absorber and has a high cell granularity. The hadronic section has stainless steel absorber plates in each cell with a coarser granularity. The cell structure (size, multiplicity and orientation) is optimised to measure the longitudinal and transverse structure of the shower; this aids in electron identification. The electromagnetic calorimeter is 3-4 cells deep in the central region; this corresponds to 20-30 radiation lengths. The hadronic calorimeter is 4-6 cells deep, so that the LAr calorimeter has a total depth of 5-8 interaction lengths . The forward wheels are much deeper, as can be seen in figure 3.8.

The performance of the LAr calorimeter has been studied with test beams, prior to assembly of the H1 Detector. The energy resolution has been found to be $\frac{\sigma(E)}{E} = \frac{12\%}{\sqrt{E}} \oplus 1\%$ for electrons [33]; the resolution for charged pions is $\frac{\sigma(E)}{E} = \frac{50\%}{\sqrt{E}} \oplus 2\%$ [34].

[4] The octants in the BBE wheel are shaped such that this wheel has a 16-fold geometry.

(a)

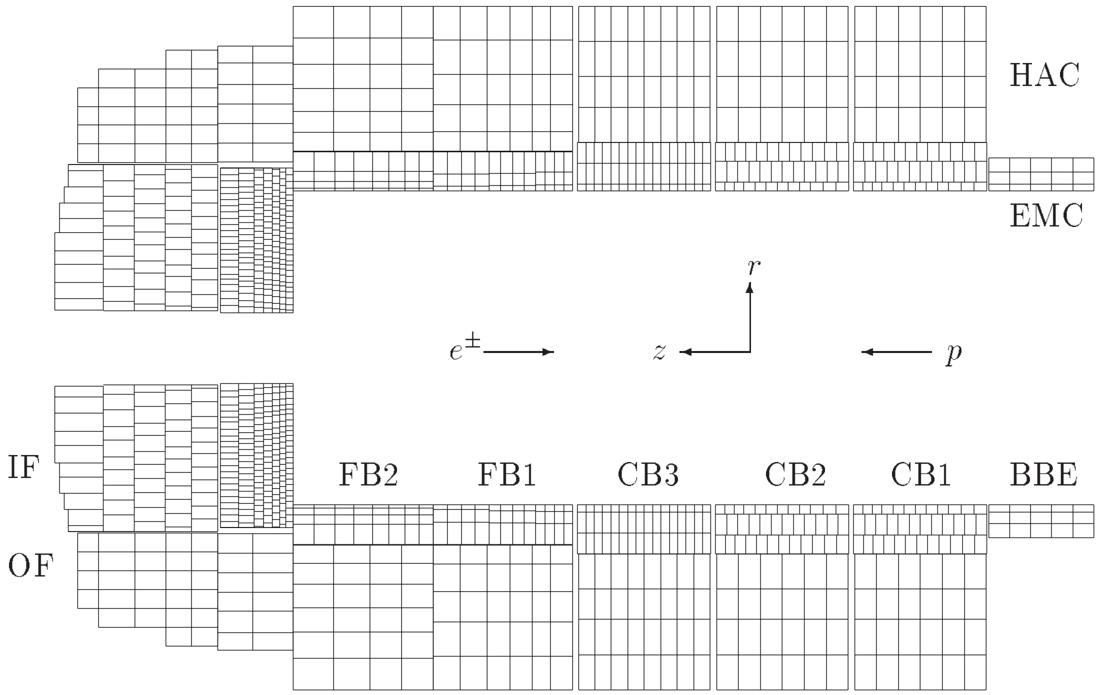

(b)

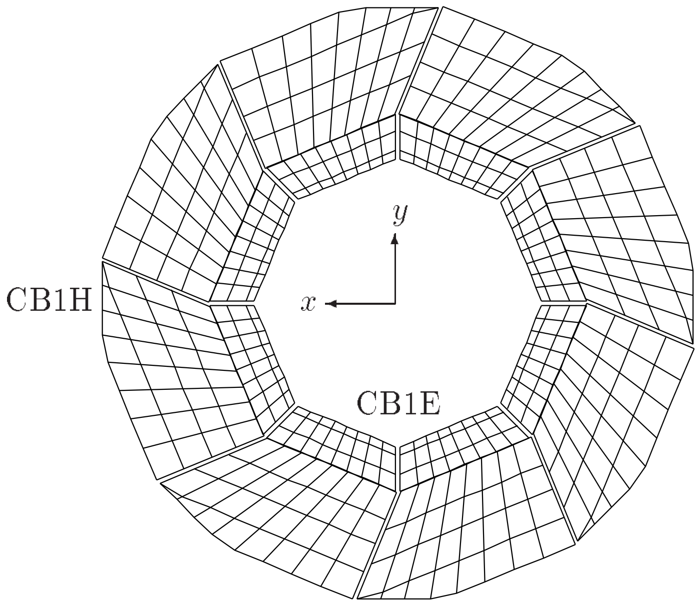

Figure 3.8: The cell structure of the LAr calorimeter: the wheel layout in the $r-z$ plane (a), and the layout of wheel octants in the $r-\phi$ plane (b).

3.4.2 Spaghetti Calorimeter

The Spaghetti Calorimeter (SpaCal) [35] is installed close to the beam-pipe to measure the energies of particles scattered into the backward region. The angular acceptance of the

SpaCal is $153^\circ < \theta < 174^\circ$; this is reduced from the original design value by the installation of the superconducting focusing magnet GG inside the SpaCal (see [36] and section 3.1 for more details), in the HERA II upgrade. The SpaCal has an electromagnetic and a hadronic section, like the LAr calorimeter, but is principally used to measure electrons back-scattered at low angles[5]. Both sections consist of lead absorber, impregnated with scintillating fibres (the sampling material). Charged particle showers from the absorber cause scintillation in the fibres; this light is collected and read out by photomultiplier tubes. The SpaCal has a time resolution of order 1 ns, providing time-of-flight information for background rejection at the L1 Trigger level (see section 3.5 for further discussion.)

The electromagnetic section of the SpaCal is fine grained, having a spatial resolution of a few mm [37]. Furthermore, electromagnetic showers are fully contained in the depth of 28 radiation lengths. The hadronic section, in contrast, has larger cells; their cross section corresponds to the lateral extent of hadronic showers. The electromagnetic and hadronic sections are each $\simeq 1$ interaction length deep. Test beam measurements reveal an electromagnetic resolution of $\frac{\sigma(E)}{E} = \frac{7\%}{\sqrt{(E)}} \oplus 1\%$ and a hadronic resolution of $\frac{\sigma(E)}{E} = \frac{30\%}{\sqrt{E}} \oplus 2\%$.

3.5 Time-of-Flight Detectors

The time-of-flight (ToF) system is used to reject beam-induced background at the trigger level [38]. It exploits scintillators with excellent (< 1 ns) time resolution to discriminate between particles arising from beam-induced background and those from an *ep* interaction. Particles from non-*ep* background will be tagged by an early arrival time in the scintillators relative to the bunch crossing time. The ToF devices are placed close to the beam-pipe, as illustrated in figure 3.9: the PToF inside the Plug calorimeter; the SToF integral to the SpaCal calorimeter; the BToF behind the backward end-cap of the instrumented iron. The FTi system was added during the HERA II upgrade. FTi2 (FTi1) sits in front (behind) the Forward Tracker at z = 2.65 m (1.45 m). The FIT, which has been installed since 1998, can be found just forward of FTi2. Lastly, the Large Veto Wall (LVeto) at z = -6.5 m is used to detect particles from the proton beam halo as well as upstream proton background.

[5]In this analysis the SpaCal is used to extend the backwards acceptance of hadronic energy measurements.

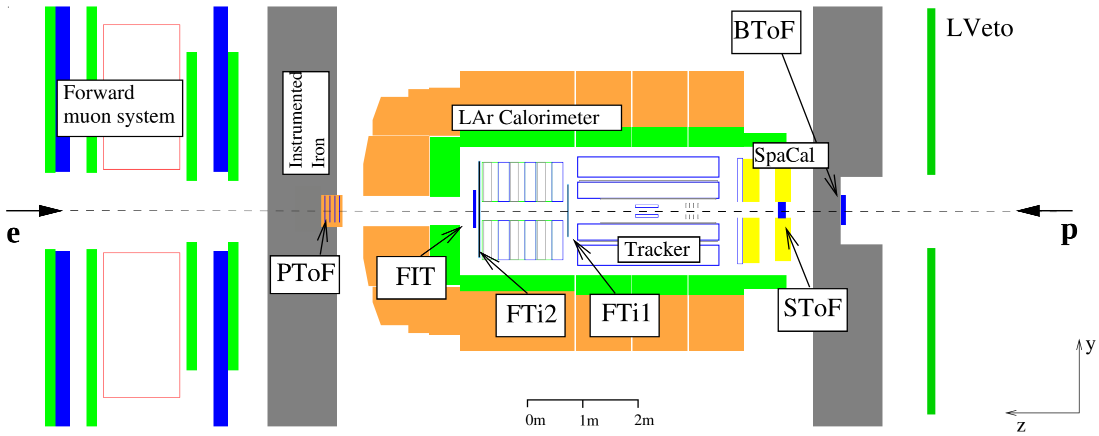

Figure 3.9: The ToF system at HERA II.

3.6 Luminosity System

The luminosity at HERA is measured through the Bethe-Heitler process, $ep \rightarrow ep\gamma$, whose cross section is large and precisely known [39]. The luminosity measurement system at H1 consists of a Photon Detector (PD), far from the interaction point, and Electron Taggers (ET). The luminosity system has several functions:

- Constant online measurement of luminosity and monitoring of the electron beam at the interaction point, for feedback to HERA;
- High precision measurement of integrated luminosity;
- Tagging of $Q^2 \approx 0$ photoproduction events, and energy measurement of the scattered electron;
- Measurement of initial state radiation.

The luminosity system has been substantially modified to deal with the challenges of HERA II [40] [41]. The strong focusing and bending (see section 3.1.2) of the electron beam leads to a significantly higher rate of synchrotron radiation than at HERA I. The photon detector must be sufficiently radiation-hard to function in this hostile environment. The PD is protected by two interaction lengths of absorber with a low atomic number, Z, in order to strongly attenuate the synchrotron radiation while limiting the degradation of the Bethe-Heitler photon energy spectrum. Multiple photons may be produced per bunch crossing at the increased design luminosities at HERA II. For this reason, upgraded electronics are necessary to control photon pileup effects. Finally, the additional focusing magnets close to the beam-pipe, near the H1 IP, restrict the potential placement of electron taggers in the backward region.

The new photon detector is a Cherenkov sampling fibre calorimeter consisting of optical quartz fibres sandwiched between layers of tungsten radiator plates, positioned at -105 m. The PD is preceded by $2\chi_0$ of Beryllium absorber, which attenuates the synchrotron radiation by almost five orders of magnitude. The photon detector provides a luminosity measurement by counting the photons above an energy threshold and comparing to the predicted Bethe-Heitler cross section to determine the instantaneous luminosity. It also measures the x and y position of the photon in order to provide feedback on the beam tilt to HERA. A compact Electron Tagger, ET6, is installed at -6 m, where scattered electrons are directed into its acceptance by beam optics. The ET6 is a lead/tungsten SpaCal-based calorimeter (see section 3.4.2). The electron tagger is used to measure the energies of the scattered electron from Bethe-Heitler and from low Q^2 photoproduction. This detector provides a useful cross check of the luminosity measurements, since the photon and electron share the energy of the beam electron. Another electron tagger, the ET40, is intended to be installed at -40 m.

The luminosity is measured online at 10 second intervals. The luminosity is determined offline with a high level of accuracy. The photon detector energy is calibrated and corrections made for energy losses in the Beryllium absorber. Corrections are applied for pileup from multiple photons and for the acceptance of the PD. Finally, the luminosity is corrected for "satellites bunches" which precede and follow the main proton bunches. The fraction of luminosity in these satellite bunches is smaller at HERA II than at HERA I since the bunches are more tightly focused in z. The final luminosity is determined to an accuracy of 1.3% [42], this provides a global normalisation uncertainty on the cross sections measured in this analysis.

3.7 Trigger System

A challenging aspect of HERA physics is the need for separation of "interesting" events resulting from ep interaction from beam induced "backgrounds". This is exacerbated at HERA II by both a five-fold increase in design luminosity and a more problematic background level in the machine, which can be up to 1000 times the ep interaction rate. A sophisticated "trigger system" is needed to make a fast decision on event quality and reduce the number of events read out to a manageable bandwidth. As the readout time is long compared to the bunch crossing interval of 96 ns (1 BC) the trigger system must be designed to eliminate or minimise the "dead-time" incurred, in which the detector is not sensitive to new events. Thus the need for a multilevel, pipelined trigger system. The details of the H1 implementation are outlined below. The nature of the backgrounds at HERA II is outlined in Section 3.1.2.

3.7.1 Trigger Level One

At the first trigger level (L1) information from each subdetector is evaluated and passed onto the central trigger logic (CTL). Not every subdetector can provide a prompt reconstruction of the event[6], so trigger element decisions are stored in a cyclic buffer, or 'pipeline'. After 24 bunch crossings (2.3 μs) the trigger elements are combined into subtriggers by the CTL. If the event fulfills the conditions of any subtrigger, a "L1 Keep" signal is sent and pipelines for all subdetectors are stopped and the event is passed to the next trigger level. Some subtriggers are prescaled such that not every event fulfilling the subtrigger conditions is kept. Prescales may be applied in order to reduce the rate of triggering of some high cross section processes or so that the performance of "physics" subtriggers may be independently monitored without disturbing data taking.

Some detector subsystems are able to provide coarse event timing information; they set a "T0" trigger bit if they identify an event in a given bunch crossing.

Described here are the Trigger Elements relevant to the Neutral Current analysis, ordered by subdetector.

Liquid Argon Trigger

The 45000 cells of the Liquid Argon Calorimeter are merged into 4844 "Trigger Cells" so that each electromagnetic (hadronic) trigger cell contains 16 (4) calorimeter cells. The trigger cells are arranged into "Trigger Towers" such that they point toward the nominal vertex. At this point, the analogue signal from individual trigger towers can be excluded from subsequent summing if they are below a programmable threshold. Trigger towers are built into so called "Big Towers" so that the LAr is segmented in 12 bins in θ and up

[6]Cable delays introduce a latency of a few bunch crossings, but the long response and readout times of the CJC and LAr dominate the delay.

to 32 bins in ϕ with the finest granularity in the forward region. The arrangement of the big towers in θ can be seen in figure 3.10 as can the projective arrangement of the towers.

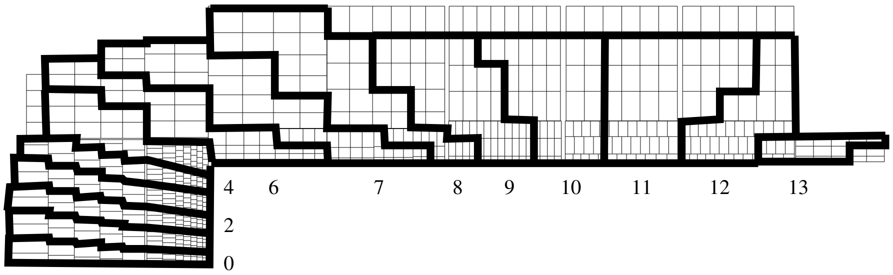

Figure 3.10: Arrangement of Big Towers in the LAr calorimeter. Each tower points toward the nominal interaction vertex.

The electromagnetic and hadronic signals from each BT are digitised by fast ADCs. The digital output is used to identify electron candidates; Big Towers are also combined to form global energy sums and topological quantities. These are encoded in trigger elements and sent to the Central Trigger. The LAr trigger elements important to this analysis are:

- **LAr_el** A potential electron signature is high (above a threshold) electromagnetic energy deposited in a BT, together with low (below threshold) energy in the associated hadronic big tower. The thresholds for the *LAr_el1* Trigger Element range from 5 GeV in the backward region to 25 GeV in the IF [43] while the trigger element *LAr_el2* has looser thresholds.

- **LAr_T0** The analogue signals from the trigger towers are processed in a special branch of the LAr Trigger system. The combined electromagnetic and hadronic signal is evaluated using a constant fraction discrimination technique [44]; this determines the T0 status for each Trigger Tower. A Big Tower T0 is combined (logical OR) from the constituent trigger towers. The *LAr_T0* for that Bunch Crossing is likewise set from a combination of big tower T0 signals[7].

- **LAr_Etmiss** The energy from each BT can be weighted by $\sin\theta$ to form the transverse energy in that big tower. The three thresholds for triggering on the combined transverse energy imbalance are 3.8 GeV (low), 4.4 GeV (medium), and 5.2 GeV (high) [43].

[7] Normally it only takes one BT T0 signal to fire the *LAr_T0*. However, noisy big towers may be excluded from the T0 determination.

The CIP2k z Vertex Trigger

The CIP2k z vertex trigger, described in detail in [29], builds tracks out of hits and follows them back to the beam line to identify the z vertex of each track. The programmable z vertex histogram is divided into central and backward (background) regions. In *ep* data-taking, the backward tracks are defined as those originating from close to the C5A and C5B collimators and are identified as background.

- **CIP_T0** A T0 bit is set if at least one track is seen in the central region. Additionally, a *CIP_T0_nextbc* bit is set in the previous bunch crossing. This can be used to prevent subdetectors with intrinsically poor time resolution, like the LAr calorimeter, from triggering the event too early.
- **CIP_sig** The CIP significance is based on the ratio of central tracks to backward tracks and can take 4 values. If the number of backward tracks is equal to or more than the number of central tracks identified by the CIP, *CIP_sig* is set to zero.
- **CIP_mul** The number of tracks within the CIP acceptance are counted, and encoded in the *CIP_mul* bits. *CIP_mul=7* indicates a threshold of 100 tracks.

Veto Triggers

Some trigger elements identify background. These are used as veto conditions in the NC triggers. The time-of-flight system is described in section 3.5. Scintillators with excellent time resolution are able to place events in either an interaction (IA) or background (BG) time window.

Additionally, the CIP can be used to veto background coming from collimators close to the H1 interaction region. The requirement (*CIP_Sig*==0 && *CIP_Mul*==7) efficiently rejects background by tagging events with a high (> 100) track multiplicity and a majority of background tracks.

3.7.2 Trigger Level Two and Three

The second trigger level (L2) is given 20 μs to make a more sophisticated assessment of the event. The L2 trigger system is able to combine detailed information from various subdetectors to validate L1 subtrigger decisions. The L2 trigger elements belong to either L2TT [45] [46], which identifies topological patterns on a 2D map of the H1 detector, and L2NN [47], in which a neural network employs information from several subdetectors to recognise good *ep* events and reject background. If a subtrigger has a L2 condition, the event may be rejected by an "L2 Reject signal" thus reducing the need to prescale high rate subtriggers.

If the event does not fail L2 verification then readout of the entire detectors starts. A third level of triggering is envisaged, employing a farm of RISC based processors, taking 50 μs, employing the Fast Track Trigger and making more use of correlation between detector subsystems. A "L3 Reject" signal can stop the readout thus reducing the dead-time incurred.

The Fast Track Trigger (FTT) [48], commissioned as part of the H1 upgrade program, performs a fast reconstruction of CJC tracks. The FTT provides some trigger elements for use at L1 and L2 and will be able to perform particle identification at L3.

3.7.3 L45 Processing

The final trigger level (L45) replaces the online L4 trigger and offline event classification scheme used at HERA I. After the $\simeq 270,000$ channels of the H1 detector are read out, the pipelines are cleared for further data taking while the event is processed asynchronously on a dedicated PC farm. The event filtering is achieved by making a full reconstruction of the event and classifying it into categories of potential interest. The L45 reconstruction software, H1REC, is described in [49]. Events that cannot be allocated to any *ep* physics class are rejected; apart from 1% which are kept for monitoring purposes. Futhermore, high rate soft scale processes are downscaled, in favour of more "interesting" events. Remaining events are written to tape at a rate of approximately 5 Hz, from a L45 input rate of $\simeq$ 50 Hz. The raw readout information is stored along with reconstructed data on "Production Output Tapes" (POTs) and reconstructed information is also written to the more compact "Data Summary Tapes" (DSTs). DSTs are used as a starting point for analysis at H1.

3.8 Offline Analysis and H1OO

A complete new software environment for analysis, H1OO, has been developed, to complement the hardware upgrades for HERA II. A new software environment based on RooT [50], written in $C++$ and utilising object oriented programming techniques, was designed and implemented over the course of the HERA luminosity upgrade project. The H1OO project has now reached a high level of maturity and exceeds the capabilities of the pre-existing H1 analysis software in many areas. A summary of the H1OO project can be found in [51].

Data Storage

The physics data scheme consists of three layers of storage. At the lowest level is the Object Data Store (ODS), which is completely equivalent to the DST. The ODS stores the same track, cluster and other detector-level information as the DST, albeit represented as $C++$ objects. These are the classes H1Track, H1Cluster and H1Cell. In practice, to avoid duplication of information on disk, the ODS layer is usually created "on the fly" when accessing the DST. The DST contents are read and an ODS information for the event is created in memory. This has only a small performance penalty compared to accessing persistently stored ODS files. In this way, the transient ODS storage layer functions as an interface from the DST tapes to the H1OO software. The second level, the micro-ODS (μODS), allows fast access to particle level information. The μODS stores identified particle (for example electromagnetic particles, hadronic particle hypotheses) four vectors and associated information. The third event layer, known as the H1 Analysis Tag (HAT), contains event level information such as the reconstructed vertex position, trigger information or kinematic quantities. The HAT is a flat tree, storing only simple variable types rather than collections of objects. This allows a fast pre-selection of events. At each stage, the storage space needed per event decreases and the size of an event on the HAT is significantly smaller than on the ODS. The data storage levels are represented schematically in figure 3.11.

Finally, the H1OO environment allows for further data layers to be added. The "normal" layers of storage described above can be extended by specially filled trees containing user-defined information. These USER trees allow persistent storage of specialised information. Reading USER trees is faster than reading and processing ODS (or POT raw data) information. USER Trees allow for experimental extensions of basic H100 objects, filling of detector level information found only on DST (or in raw data) or more sophisticated

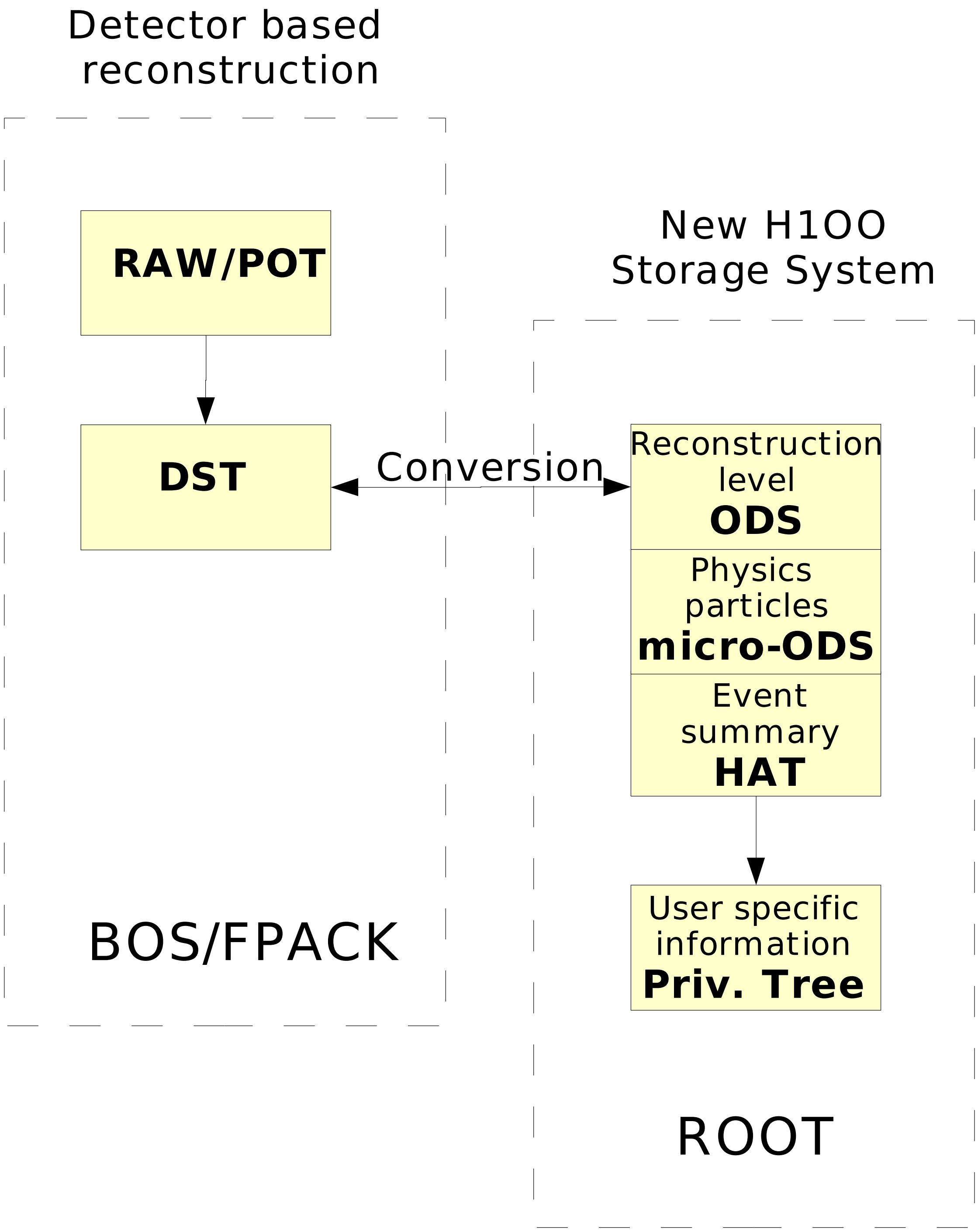

Figure 3.11: A schematic overview of the data storage levels used by the H1OO Project.

physics finders used for only a small subset of analyses.

In this analysis, detailed information on the LAr trigger (see section 3.7.1) is used to evaluate the efficiency of the principal trigger element for high Q^2 Neutral Current, *LAr_el1*. The list of big towers that fired for each selected NC event is stored in a USER tree for convenient offline analysis [52]. See section 8.2.2 for discussion of the results of this study.

Generic Analysis

While the H1OO project provides a common basis for analysis, with expert knowledge available to all users and the ready availability of all quantities suitable for analysis, there still remains a need to standardise common analysis tasks. Hence the need for a generic analysis framework to complement the H1OO software with high level analysis tools. Tasks like event selection book-keeping, histogramming, determination of event weights and binning of kinematic variables are common to all kinds of physics analyses. The H1OO generic analyses framework, described in further detail in [53], provides tools to accomplish all these tasks. The steps required for analysis are further formalised with dynamically steerable[8] analysis objects. This allows users to quickly and simply build, or extend, an analysis code base comprised of objects representing the tasks necessary in the analysis.

The "Calculator" package is an important part of the generic analysis framework, which interfaces to the H1OO data. The Calculator is essentially a transient event layer, lying between the data storage and the high level analysis tools. As well as providing further information calculated from μODS/HAT variables, the Calculator allows the determination and combination of event weights for data and simulation. It also provides a mechanism for the propagation of systematic shifts. The effect of systematic mis-measurements can be accounted for by propagating a shift in, e.g., the scattered electron energy, through the calculation of event kinematics. This is effective, and much less expensive in terms of CPU time and storage space than re-creating data files for each systematic shift.

The analysis presented in this document has been performed in the H1OO analysis framework using the generic analysis tool; both of which are described above. The analysis and the framework have been tested against Fortran based analyses; see [54], [55] and [51] for further details.

[8]The H1OO framework provides a steering mechanism, allowing run time behaviour to be set by text files.

Chapter 4

Kinematic Reconstruction

With fixed centre of mass energies at HERA, the inclusive DIS process can be described by two kinematic variables. The kinematics are over-constrained in NC events since there is redundant information available from the measurement of both the lepton and the hadronic final state. There are then various methods available for the reconstruction of the kinematic variables, the choice of method determining the acceptance of the measurement, the influence of radiative corrections and the sensitivity to detector resolution. The methods of kinematic reconstruction useful for a DIS measurement are introduced in this section.

4.1 Electron Method

In the electron method, the kinematic variables are determined from the energy, E'_e, and angle, θ_e, of the scattered electron as measured in the H1 Detector.

$$Q_e^2 = 4E_e E'_e \cos^2\frac{\theta_e}{2}, \qquad y_e = 1 - \frac{E'_e}{E_e}\sin^2\frac{\theta_e}{2} \qquad \text{and} \qquad x_e = \frac{Q^2}{sy_e}. \tag{4.1}$$

The resolution in y_e, and hence x, degrades with decreasing y due to a $\frac{1}{y}$ dependence in the partial differential:

$$\frac{\delta y_e}{y_e} = \frac{y_e - 1}{y_e}\frac{\delta E'_e}{E'_e} \quad \oplus \quad \frac{y_e - 1}{y_e}\cot\frac{\theta_e}{2}\delta\theta_e \tag{4.2}$$

The resolution in Q_e^2 remains good over the whole kinematic range.

4.2 Hadronic Method

The hadronic final state can be represented by the variables:

$$\tan\frac{\gamma_h}{2} = \frac{\Sigma}{p_{T,h}}, \quad \text{where} \quad p_{T,h} = \sqrt{(\sum_i p_{x,i})^2 + (\sum_i p_{y,i})^2}, \quad \text{and} \quad \Sigma = \sum_i (E_i - p_{z,i}) \tag{4.3}$$

where the sum is over all particles in the hadronic final state[1]. The kinematic variables can be defined as [56]:

$$Q_h^2 = \frac{p_{T,h}^2}{1-y_h}, \qquad y_h = \frac{\Sigma}{2E_e} \qquad x_h = \frac{Q_h^2}{s y_h}. \tag{4.4}$$

The hadronic reconstruction is useful only for a Charged Current analysis, where the final state neutrino is not detected. For a Neutral Current measurement, the degrading Q_h^2 resolution with increasing y, and the comparatively large uncertainty in the hadronic measurement (see section 6.2.3), makes it an undesirable method.

$$\frac{\delta Q_h^2}{Q_h^2}|_{p_{T,h}} \propto \frac{\delta p_{T,h}}{p_{T,h}} \qquad \frac{\delta Q_h^2}{Q_h^2}|_{\Sigma} \propto \frac{1}{E_e}\frac{\delta\Sigma}{1-y_h} \tag{4.5}$$

4.3 Sigma Method

In the case that a photon is emitted from the incident electron, the effective centre of mass energy of the *ep* system is reduced. Such a radiative photon is usually co-linear with the incident electron beam and escapes undetected down the beam-pipe. Three variables are required in order to describe such a radiative event.

The Sigma method [57] is constructed to use both electromagnetic and hadronic variables, and to be independent of the initial state electron beam energy:

$$Q_\Sigma^2 = \frac{(E_e' \sin\theta_e)^2}{1-y_\Sigma} \qquad y_\Sigma = \frac{\Sigma}{E-p_z} \qquad x_\Sigma = \frac{Q_\Sigma^2}{y_\Sigma} \tag{4.6}$$

Here $E - p_z \equiv \Sigma + E_e'(1-\cos\theta_e)$ is the longitudinal "energy balance", which would be equal to twice the energy of the incoming electron in a fully hermetic, perfect, detector. The Sigma method can thus be used to determine the kinematic quantities in a way that is largely insensitive to radiative effects.

[1] The "Hadronic Final State" (HFS) is defined as all particles apart from the scattered lepton.

4.4 Electron Sigma Method

The Sigma method provides good kinematic reconstruction across the whole kinematic range. For example, the y-resolution approaches that of the hadron method at low y and performs like the electron method at high y. It is possible to combine the best features of the electron and Sigma methods, as noted in [58], by choosing:

$$Q^2_{e\Sigma} = Q^2_e \qquad x_{e\Sigma} = x_\Sigma \quad \text{and} \quad y_{e\Sigma} = \frac{Q^2_e}{x_\Sigma s} \tag{4.7}$$

The $e\Sigma$ method gives the best resolution in Q^2 and x across the whole kinematic range accessible at HERA, and has only minor sensitivity to radiative corrections. It is used to determine the kinematic variables for NC events in this analysis.

4.5 Double Angle Method

An alternative is to use only the angles of the electron and the hadronic final state in kinematic reconstruction [59]. This method is, to a good approximation, insensitive to the calorimeter energy scale.

$$Q^2_{DA} = \frac{4 \cdot E^2_e \cdot sin\gamma_h(1 + cos\theta_e)}{sin\gamma_h + \sin\theta_e - \sin(\theta_e + \gamma_h)} \qquad y_{DA} = \frac{\sin\theta_e \cdot (1 - \cos\gamma_h)}{sin\gamma_h + \sin\theta_e - \sin(\theta_e + \gamma_h)} \tag{4.8}$$

The resolution of Q^2_{DA} and y_{DA} perform like $\frac{\delta\gamma_h}{\sin\gamma_h} \oplus \frac{\delta\theta_e}{\sin\theta_e}$ [57]. Thus the DA reconstruction method performs badly for small and large angles of the electron and the hadronic final state.

Since this reconstruction method uses only the measured angles in the final state, and so is not directly sensitive to the momentum measurement, it is suited to the calibration of the calorimeters. The energy of the scattered electron can be predicted as

$$E_{DA} = \frac{2E_e \sin\gamma_h}{sin\gamma_h + \sin\theta_e - \sin(\theta_e + \gamma_h)}. \tag{4.9}$$

This prediction is used to determine the electromagnetic energy scale (see Section 6.1.)

Chapter 5

Monte Carlo Technique and Detector Simulation

The Monte Carlo (MC) technique [60] has been invaluable in making well controlled physics measurements. A cross section measurement requires corrections for detector acceptance and an understanding of the influence of the resolution of detector components. These are difficult to determine from data, due to the complex interplay of different detector effects.

Thus the detector behaviour must be correctly simulated in this analysis. The selection efficiencies, detector calibration and resolution are generally determined directly from data. The MC simulation is corrected as necessary in order to correctly model observed detector effects in data. The Monte Carlo is also used to model the inevitable smearing due to finite detector resolutions.

The simulation of the H1 Detector is briefly discussed first. Then the Monte Carlo programs used to simulate the signal process are described. Finally, processes that can contribute background are noted, and the event generators used to model these backgrounds are noted.

5.1 Detector Simulation

The detector response to generated particles (in either a background or a signal event) is simulated in detail using the package H1SIM, which utilises the GEANT program

[61] to model the passage of particles through the detector. The parameters used by this package were determined in test-beam measurements and optimised during *ep* data taking. A fast parameterisation of the development of electromagnetic and hadronic showers, as implemented in H1FAST, is used in the simulation of the energy response of the calorimeters. The simulated detector readout for each event is finally fed into the reconstruction software, H1REC [49]. Here, as for data, the H1REC software provides a summary of the event. The programs used in the subsequent offline analysis are described in section 3.8.

5.2 Generation of Neutral Current DIS

The signal DIS events are generated using the DJANGO program package [62]. The version used in this analysis, DJANGOH 1.2, contains the HERACLES [63] 4.6.2 event generator and the LEPTO 6.5.1 [64] package to simulate the complete event. HERACLES gives the hard subprocess and first order QED corrections. In DJANGO, HERACLES is interfaced to LEPTO, which provides a description of the complete event including QCD radiation and QCD cascades. The JETSET [65] package provides an implementation of the Lund String Model [66], used to model the hadronisation process.

The events are generated using the MRSH [67] PDFs as input. The simulated DIS cross-section is then re-weighted to a NLO QCD fit of HERA I data (the H1 2000 PDF) [3].

5.3 Backgrounds to Deep Inelastic Scattering

Monte Carlo simulations can also be used to help define variables and tune cuts in order to discriminate signal events from background, and estimate the remaining background contamination. Backgrounds to NC DIS are categorised into those that can arise from *ep* physics and non-*ep* background sources.

The main sources of non-*ep* induced background are:

- Hadronic showers from interactions of the proton beam with residual gas or beam-pipe material.
- "Beam-halo muons" originating far up-stream from the H1 Interaction Point, and passing through the calorimeters parallel to the proton beam direction.

- Muons from cosmic rays

These events can be rejected by timing and vertex requirements. Remaining background events are identified by topological filters designed for this purpose (see section 8.3.1) and rejected, leaving negligible contamination.

Backgrounds from ep induced processes can have detector signatures indistinguishable from NC DIS events. Therefore there is no alternative to estimating the contributions with Monte Carlo.

- **Photoproduction** ($ep \to \gamma p$) is the dominant background process for NC DIS. At very low four-momentum transfer squared ($Q^2 \approx 0$ GeV^2), the proton interacts with a quasi-real photon and the cross section is high. Generally, the electron is scattered through a small angle such that it is not detected in the central part of the H1 Detector. However, a particle from the hadronic final state may be mis-identified as the scattered electron. The photoproduction process is modelled by the PYTHIA 6.2 [68] event generator, using the GRV LO [69] parton densities for the proton and the photon.

- **Elastic QED-Compton scattering** ($ep \to ep\gamma$) is treated as a background process since the exchanged photon has a low Q^2. A large four-momentum transfer between the final state electron and photon can scatter both particles into the central part of the detector. Further discussion of the dynamics of the QED Compton process at H1, simulated by the WABGEN MC generator [70] in this analysis, can be found in [71]. These events are also used to cross-check the electron energy calibration (see section 6.1.1.)

- **Lepton-pair production** [72] contributes background to the Neutral Current DIS process, particularly when the final state lepton pair is electrons: $e^+p \to e^+pe^+e^-$ or $e^+p \to e^+Xe^+e^-$. Lepton-pair events are generated by LPAIR [73].

- **Real W^{+-} production** occurs at HERA [74] with a small cross-section, $\sigma \simeq 1$ pb via $ep \to eXW^{+-}$. The scattered electron is not usually detected. However, the process could fake an NC event if the W boson decays leptonically. This process is simulated by the MC generator EPVEC [74], but does not contribute significantly to the NC sample.

Chapter 6

Energy Calibration

6.1 Electromagnetic Energy Calibration

The calibration of the LAr calorimeter energy can be performed using DIS data by exploiting the over-constrained kinematics of the H1 detector. The measured angle of the scattered electron and the hadronic final state, together with the precisely known beam energies, can be used to predict the energy of the scattered electron, using equation 4.9. The prediction of the electron energy from the Double Angle (DA) method provides an independent reference scale against which to calibrate the calorimeter energy measurement using a subset of the full NC data sample. The calibration is cross-checked with QED Compton events. The energy calibration in the forward wheels of the detector is examined using low statistics event samples from $ep \rightarrow epe^+e^-$, $ep \rightarrow ep\gamma$, and DIS events.

The energy prediction E_{DA} is compared to the "true" electron energy, E_{Gen}, in Monte Carlo events in figure 6.1(a). The energy is well reconstructed by the DA method, with a resolution $\lesssim 2\%$ for $y_\Sigma < 0.3$. The degradation of the resolution with increasing y_Σ is due to the less precise reconstruction of γ_h and the larger influence of radiative corrections.

The energy calibration is studied with a sub-sample of the inclusive selection given in section 8.4. Additional cuts are applied to select a very well measured final state and hence a more precise prediction E_{DA}.

- $y_\Sigma < 0.3(0.5)$ for $z_{impact} < 20$ cm($20 < \mathrm{z_{impact}} < 100$ cm) ensures a precise reconstruction of E_{DA}.

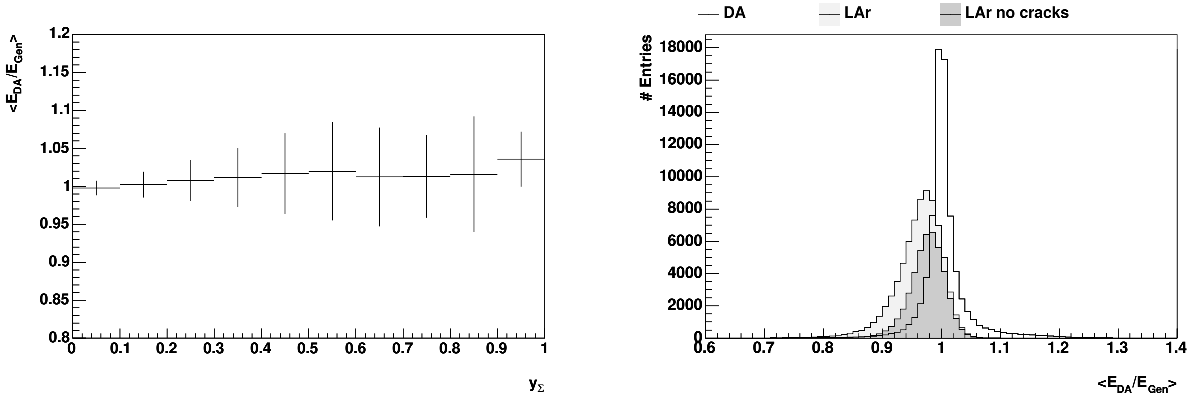

(a) (b)

Figure 6.1: The reconstruction of the scattered electron energy using the DA method is compared to the generated energy for Monte Carlo events. The mean and resolution (denoted by the error bars) of the ratio E_{DA}/E_{Gen} is shown in (a) as a function of y_{Σ}, while the distribution of E_{DA}/E_{Gen} (histogram) is compared to E_{LAr}/E_{Gen} for all events (light grey area) and outside z cracks (dark grey area) in (b). The distributions on the right are produced with the sub-sample used for calibration.

- $\gamma_h > 8°$ requires that the hadronic final state is well contained in the detector and therefore well measured.
- $44 < E - p_z < 66$ GeV reduces the influence of radiative effects on the DA reconstruction.
- $0.5 < p_{T,h}/p_{T,e} < 1.5$ ensures a good reconstruction of the hadronic final state.
- The region near ϕ-cracks, where electrons are poorly contained, is not calibrated. See section 7.1.1.

The energy reconstruction by the DA method is compared with that by the LAr calorimeter in figure 6.1(b) for the sub-sample defined above. The mean value of E_{LAr} is shifted from the "true" energy and the distribution has a significant tail to low values. The extent of the tails is reduced when excluding events in z cracks, where showers may not be fully contained. The Double Angle energy prediction agrees very well with the "true" energy and has a resolution superior to the calorimeter measurement, with the above selection. Thus E_{DA} is well suited to providing a reference scale for calibration of the electromagnetic energy response of the LAr.

The calibration procedure is based on that of previous analyses [75]. The measured calorimeter energy, E_{LAr}, is compared to the predicted Double Angle energy, E_{DA}, as a function of electron impact position in the LAr. The calorimeter is segmented by wheels in the z direction and by octants in ϕ. The electron impact position is defined from track and cluster measurements following the procedure outlined in section 7.4.4.

Calibration factors are obtained by locally constraining the ratio E_{LAr}/E_{DA} to one. The calibration is a two stage process: calibration factors are initially determined as a function of ϕ, and subsequently as a function of z. This calibration procedure is performed for both data and Monte Carlo in order to correct for any biases in the reconstruction.

Octant-wise Calibration In the first stage of the calibration the binning is per octant within each wheel. The regions are enumerated by $N_{stack} = 8 * N_{wheel} + N_{octant}$. Here $N_{octant} = 0..7$ for $\phi = 0...360°$, and the wheels are enumerated by $N_{wheel} = 0..3$ for BBE...CB3. No attempt is made to calibrate the z cracks between wheels, or the backward half of the BBE, at this stage. The mean values of E_{LAr}/E_{DA} are taken from fits to the distribution in each N_{Stack} bin. These mean values form the calibration constants, summarised in figure 6.2. The data exhibit structure in ϕ within each wheel which is

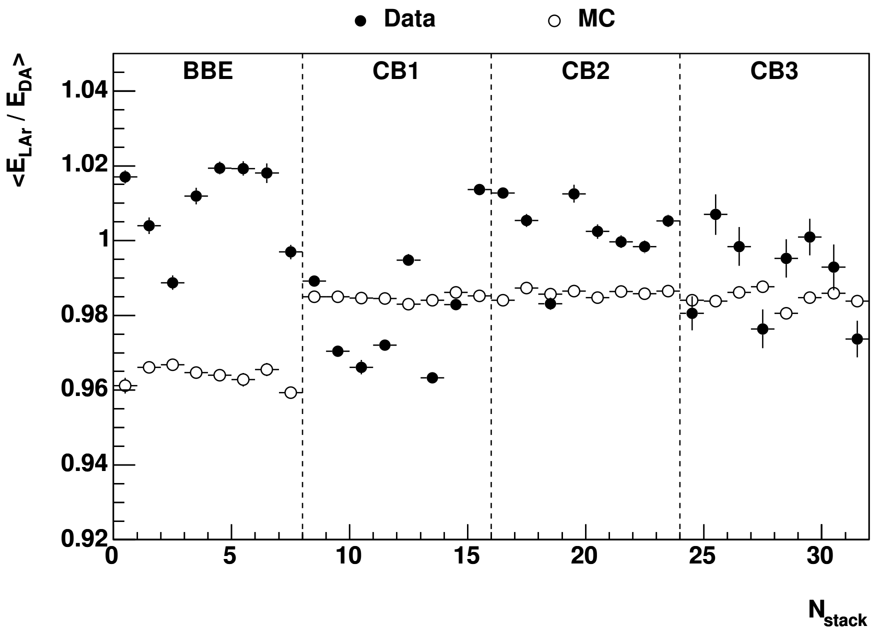

Figure 6.2: $< E_{LAr}/E_{DA} >$ as function of stack number in the backward part of the calorimeter for data (full circles) and MC (open circles).

not reproduced in the MC. However, these ϕ dependent variations are within $\pm 3\%$ in all wheels.

Z-wise Calibration After applying the octant-wise calibration factors, the energy calibration is studied as a function of z_{impact}. Bins are chosen to be 1 cm wide in the most backward barrels, and 10 cm wide in the CB3 wheel, where statistics are limited. The calibration factors are shown as a function of z in figure 6.3. The calibration factors are large and differ between data and simulation in the regions between wheels, where energy leakage is significant. Away from these regions, the factors are close to unity.

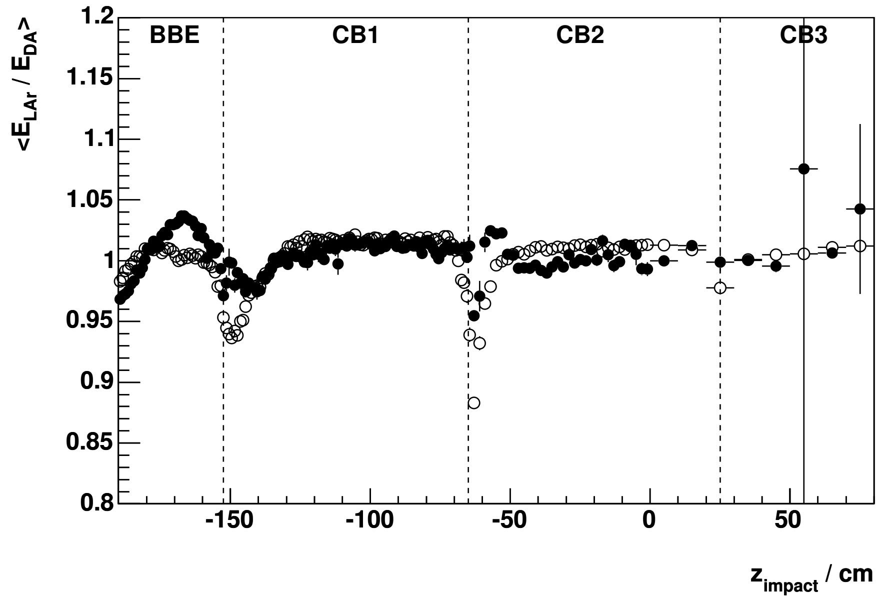

Figure 6.3: The final calibration constants, demonstrated by $< E_{LAr}/E_{DA} >$ as a function of impact position of the electron for data (full circles) and MC (open circles).

After applying these calibration factors to events in both data and simulation, the mean value $< E_{LAr}/E_{DA} >$ is shown as a function of z_{impact} in figure 6.4. It is everywhere close to unity, with only small mis-calibrations of $\simeq 1\%$ near cracks and in the most backward part of the BBE. A good agreement, to well within 1% on average, between data and simulation is observed. Control of the electron energy is poorest in the z crack between the CB2 and CB3 wheels, where energy leakage becomes important. Therefore the region $15 < z < 25$ cm is cut from the analysis.

Energy Resolution The energy resolution of the LAr for electromagnetic deposits has been studied with test beams at CERN [33] and found to be $\frac{\sigma(E)}{E} = \frac{12\%}{\sqrt{E}} \oplus 1\%$. The good resolution of the DA energy allows for the electron energy resolution to be studied in situ. The z dependence of the resolution, obtained from Gaussian fits to the E_{LAr}/E_{DA} distribution, is summarised in figure 6.5. The best energy resolution can be seen in CB1

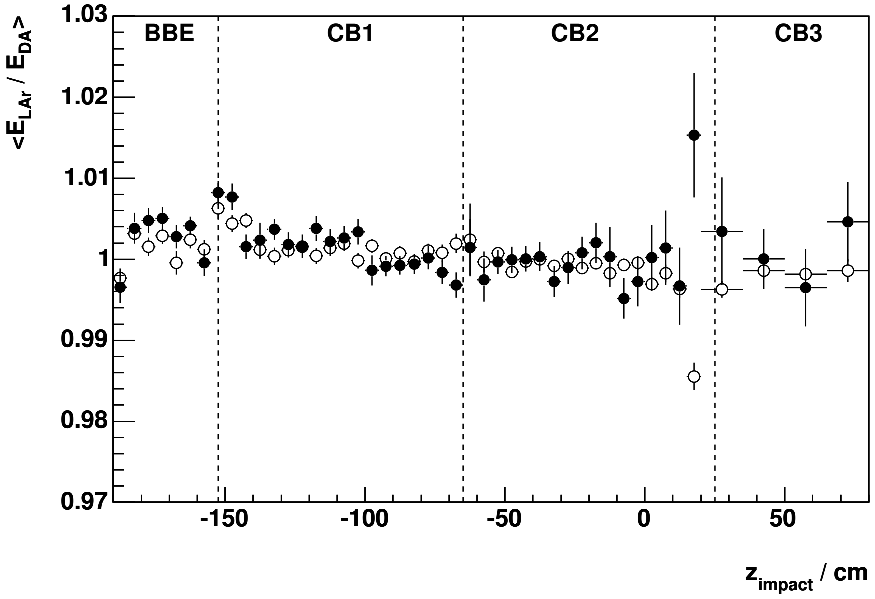

Figure 6.4: $< E_{LAr}/E_{DA} >$ vs. z_{impact} after calibration for data (full circles) and MC (open circles) simulation.

and CB2, where it is typically $\simeq 3-4\%$. It degrades in the BBE region, as the electron moves backwards, and reaches almost 6%. The resolution is also significantly worse near to the z-cracks, at $z \simeq -65$ cm and $z \simeq -150$ cm. This behaviour is not fully reproduced by the simulation. The description of the energy resolution by the simulation is improved by applying an additional Gaussian smearing with a width equal to the difference between the resolution in data and simulation, $\sigma_{smear} = \sigma_{data} - \sigma_{MC}$. This difference is determined for every z bin used in the z-wise calibration. The improved description of the data by the MC after this last correction can be seen in figure 6.6.

Calibration in Forward Wheels The calibration procedure described above cannot be applied to wheels in the forward direction: FB1, FB2 and IF. The statistics available fall off rapidly with scattering angle so that it is not possible to study the energy response of these wheels with any granularity. Calibration constants determined per wheel in previous analyses of HERA I data [75] are used here.

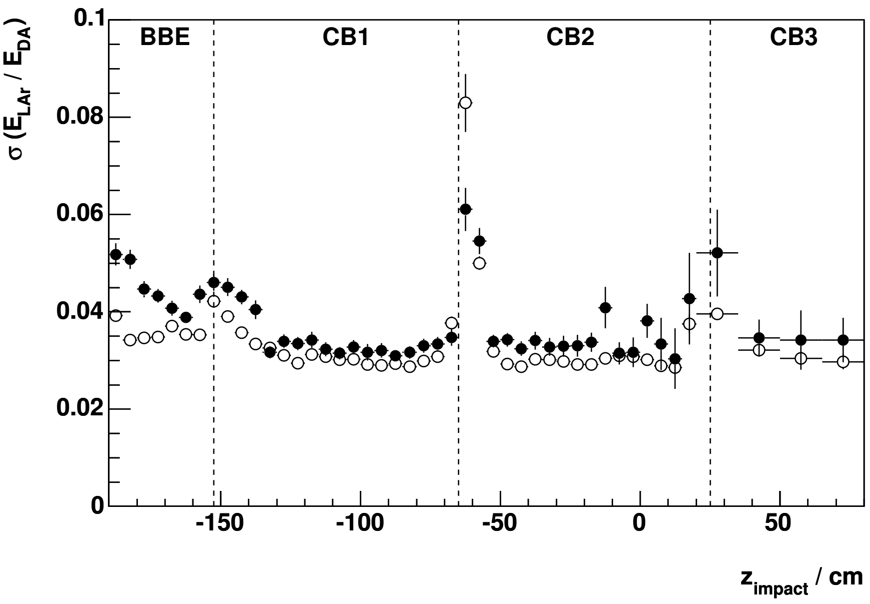

Figure 6.5: The resolution of the electron energy as a function of z_{impact} after calibration for data (full circles) and MC (open circles).

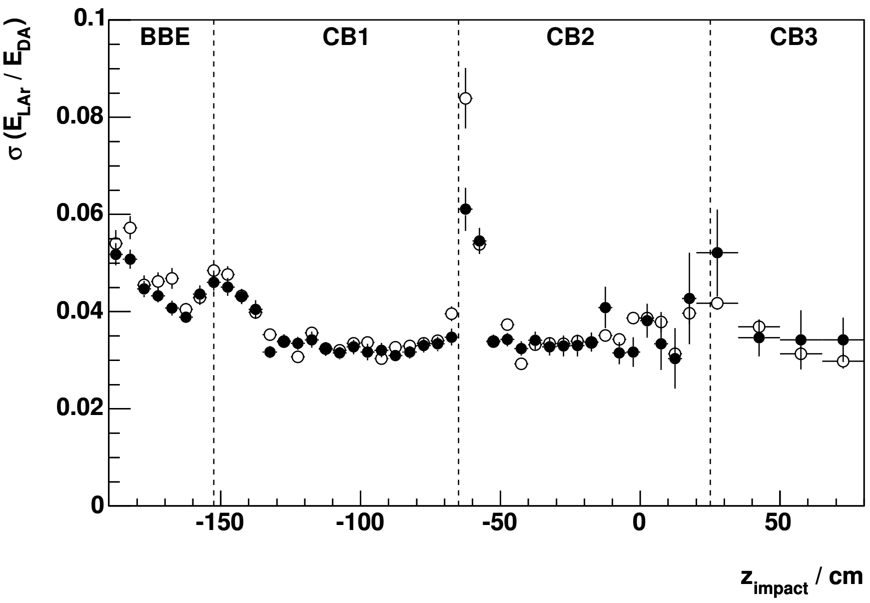

Figure 6.6: The resolution of the electron energy as a function of z_{impact} after calibration and a Gaussian smearing of the energy for the simulation.

6.1.1 Calibration Checks

QED Compton Calibration The universality of the calibration is checked with an independent physics sample. The QED Compton process, $e^+p \rightarrow e^+p\gamma$, can lead to a final state consisting of two electromagnetic particles and no other activity in the detector. The energies of each electromagnetic particle can be predicted by the Double Angle method, in the same way as in the inclusive NC sample. This cross-check has the benefit that lower electron energies can be accessed; the y_Σ cut applied to the Neutral Current sub-sample is effectively an electron energy cut. The linearity of the calorimeter response to electrons can thus be tested.

QED Compton events are selected by the following criteria.

- Two isolated electromagnetic particles found in the LAr calorimeter
- Both electromagnetic clusters have an energy > 11 GeV
- Neither electromagnetic clusters are found near z or ϕ cracks
- The electromagnetic clusters are found with a back-to-back topology
- There is only one charged track in the event
- No hadronic energy deposits are measured in the detector
- $\eta_{max} < 3$ (see section 8.3)
- The event is well-balanced in longitudinal momentum, $45 < E - p_z < 65$ GeV
- The same good run selection (and accompanying polarisation quality selection) is made as for the inclusive NC sample.

This selection is henceforth referred to as the QED Compton sample. The electromagnetic particles in the selected sample are ordered by scattering angle, and no attempt is made to distinguish photons from electrons for the purposes of this study.

The results of the study of the energy dependence of $< E_{LAr}/E_{DA} >$ are shown in figure 6.7. Data and simulation are consistent, within the quoted systematic uncertainty, for both the NC DIS and QED Compton sample. The QED Compton points demonstrate the linearity of the electron calibration down to low energies.

Cross Checks of the Calibration Finally, the performance of the calibration is investigated wheel-wise using two independent data samples. The forward wheels FB1, FB2

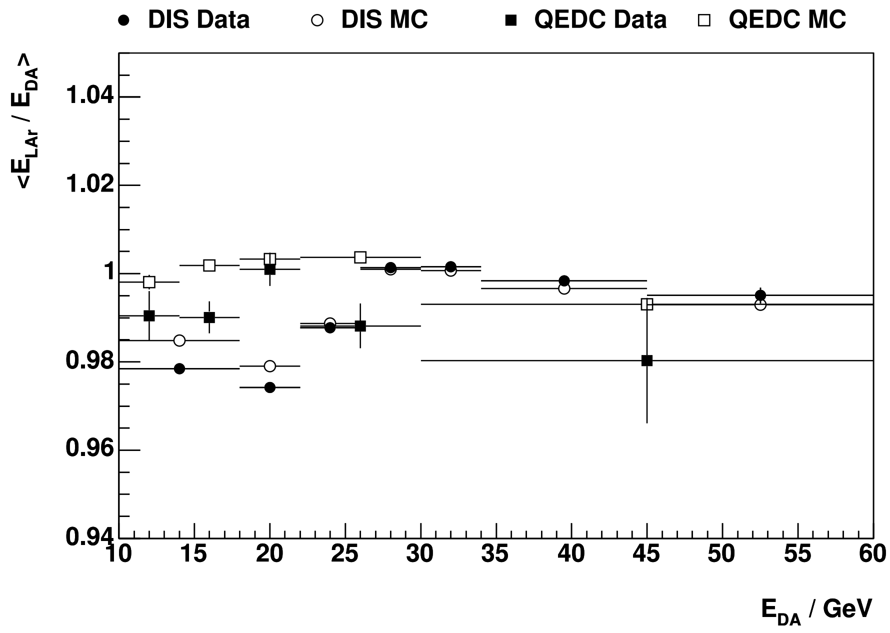

Figure 6.7: Dependence of the mean ratio $< E_{LAr}/E_{DA} >$ on the electron energy, reconstructed with the DA method. Shown here are both NC DIS events and QED Compton.

and IF will be treated as one entity due to the limited statistics available. The calibration is studied using the DA reconstruction method for both the inclusive NC and QED Compton samples, and using the ω method [76] for the NC sample.

The ω kinematic reconstruction method implicitly quantifies the mis-calibration of the electromagnetic, δE_{LAr}, and hadronic, $\delta\Sigma$, energy scales. With the assumption that the mis-measurements in Σ and $p_{T,h}$ are the same, conservation of longitudinal and transverse momentum give the results:

$$(y_e - 1)\frac{\delta E_{LAr}}{E_{LAr}} - y_h \frac{\delta\Sigma}{\Sigma} = y_e - y_h \qquad \text{and} \tag{6.1}$$

$$p_{T,e}\frac{\delta E_{LAr}}{E_{LAr}} - p_{T,h}\frac{\delta\Sigma}{\Sigma} = p_{T,e} - p_{T,h} \tag{6.2}$$

which lead to

$$\frac{\delta E_{LAr}}{E_{LAr}} = \frac{p_{T,h}\, y_e - p_{T,e}\, y_h}{[\, p_{T,h}\,(1 - y_e) - p_{T,e}\, y_h\,]} \qquad \text{and} \tag{6.3}$$

$$\frac{\delta\Sigma}{\Sigma} = \frac{p_{T,h} - p_{T,e}\,(1 - \frac{\delta E_{LAr}}{E_{LAr}})}{p_{T,h}} \tag{6.4}$$

The relative mis-calibration between data and simulation, as estimated by the DA and ω methods, is compared in figure 6.8. There are too few QED Compton events to provide an estimate of the mis-calibration in the forward wheels.

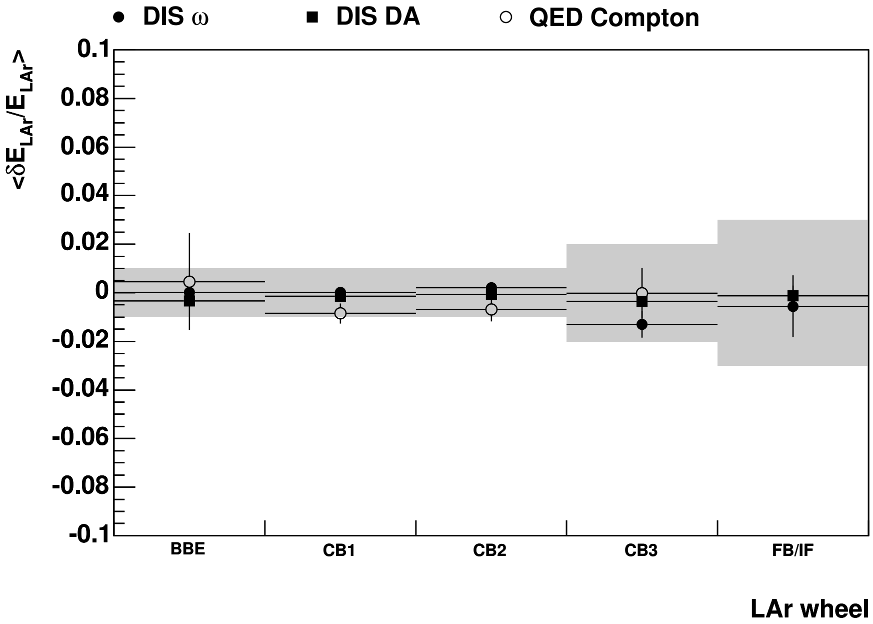

Figure 6.8: Cross check of the electromagnetic energy scale in the LAr using different energy reconstruction methods. The relative mis-calibration between data and simulation is shown for each calorimeter wheel. The error band demonstrates the systematic uncertainty attributed to the energy, which varies from 1% to 3%.

A 1% systematic uncertainty is assigned on the electron energy determination in the BBE, CB1 and CB2 wheels. The control of the electromagnetic energy is limited by the available statistics in the more forward wheels. A 2% uncertainty on the energy is assigned in the CB3 wheel, and a 3% uncertainty is assigned in the FB and IF wheels.

6.2 Hadronic Energy Measurement

The reconstruction of the hadronic final state (HFS) is performed by the HFS Finder in the OO Framework. The algorithm, HADROO2 [77], is an "energy flow" algorithm, combining measurements from different sub-detectors. The HADROO2 algorithm has an improved calorimetric noise rejection, compared with previous implementations. There is also an accompanying absolute jet calibration, suitable for high Q^2 analyses.

The treatment of tracks and clusters used in the HADROO2 algorithm is briefly reviewed below. In particular, the weighting of hadronic energy deposits and noise suppression techniques in the calorimeter are discussed. Then the HADROO2 algorithm itself will be described. Finally, the jet calibration is discussed and the hadronic energy calibration tested.

6.2.1 Hadronic Reconstruction

Track Selection

Tracks used by the HFS algorithm must fulfill the standard track quality selection (see section 7.4.) The reconstruction of Forward Tracker tracks is not yet well understood at HERA II and so only central tracks are selected for input.

Cluster Treatment

Calorimeter clusters are aligned to the Central Tracker using the same alignment factors applied to the scattered electron. Hadronic clusters are also corrected for the beam tilt, on a run-dependent basis. The alignment and beam tilt correction of calorimeter clusters is discussed in sections 7.4.3 and 7.4.2. Only LAr and SpaCal clusters are considered for inclusion in the hadronic final state: neither Iron nor Plug clusters are used[1]. Clusters dominantly in the LAr, yet with cells in the Iron or Plug have those cells removed.

Weighting Liquid Argon calorimeters are non-compensating: their response to hadronic showers is lower than the response to an electromagnetic shower of the same energy. This is compensated for in software [31] at the reconstruction level, with a weighting applied to clusters identified as hadronic. This classification is modified in HADROO2: clusters with at least 95% of their energy in the electromagnetic calorimeter and 50% deposited in the first two layers are classified as electromagnetic in origin and are taken at the electromagnetic scale. All other clusters are taken at the hadronic scale.

[1]The inclusion of Iron clusters connected to activity in the LAr could improve the determination of high p_T jet energy. However, the mediocre energy resolution of the Iron streamer tubes coupled with the significant fraction of Iron clusters originating from noise or background make its inclusion difficult.

Noise Noise in the calorimeters can bias the reconstruction of $\Sigma = (E - p_z)_{hadrons}$ (see equation 4.3): Σ is small when the hadronic final state is scattered at small angles. Thus a small "fake" energy deposit in the central barrel or SpaCal can bias the reconstruction for an event at low y. HADROO2 utilises a succession of algorithms to identify and remove noisy calorimetric clusters. These are described in [78]. Unlike the dedicated topological background finders discussed in section 8.3.1, these noise suppression algorithms are designed to remove fake energy deposits and cosmic overlays while keeping the event. The noise finders utilised by HADROO2 are discussed below. Note that a further "topological noise suppression", ETNS [22], is applied earlier at the reconstruction level (by H1REC).

Clusters consisting of only one cell are removed, as are very low energy clusters (less than 0.2 GeV in the LAr or 0.1 GeV in the SpaCal). Then further noise finders are applied, as listed below together with a brief description of their function.

- **FSCLUS** suppresses low energy clusters unless they are close to more energetic ones.
- **NEWSUP** is a development of FSCLUS, with higher thresholds in the central region of the LAr in order to further reduce noise levels. To avoid suppressing real energy deposits, clusters are kept if they can be linked to a vertex-fitted track
- **HALOID** is devoted to the suppression of energy deposits from beam halo muons on top of real physics events.
- **HNOISE** is designed to combat cosmic muons and coherent noise. Although these kinds of overlays do not have a characteristic signature, genuine hadronic deposits should in general be either connected to electromagnetic activity or linked to charged tracks.

The noise is added, on a random basis, to the simulated energy deposits in MC. This noise is taken from periodic dedicated noise runs.

6.2.2 HADROO2 Algorithm

The HADROO2 algorithm realises the creation of HFS particles from input tracks and clusters, without double counting. The algorithm aims to combine track and cluster measurements, both of which may exist for a charged particle, in order to gain the best measurement. The relative resolution of each charged track is compared to the expected resolution for a calorimeter deposit of the same energy, and used to form a decision on which measurement to take. The details of the decision are informed by a comparison of the measured track energy with the summed energies of clusters close to the track. Particles may be defined by the track measurement, the track and cluster together or the cluster measurement alone. After all tracks have been considered, particle candidates are built from remaining unassigned clusters.

Identified electrons and muons not flagged as isolated[2] are considered a part of the hadronic final state; but their four-vectors remain unchanged and their associated tracks and clusters are excluded from any treatment by the HADROO2 algorithm.

Comparison of Resolutions Tracks are hypothesised to originate from a pion and the energy is formed from the momentum and pion mass. The relative error on the energy measurement of each track is obtained by standard error propagation as

$$\frac{\sigma_{E_{track}}}{E_{track}} = \frac{1}{E_{track}} \sqrt{\frac{p^2_{T,track}}{\sin^4\theta} \cos^2\theta \sigma^2_\theta + \frac{\sigma^2_{p_T}}{\sin^2\theta}}, \tag{6.5}$$

where σ_{p_T} and σ_θ are the error on the measurement of p_T and θ by the track. The corresponding error on a LAr cluster of the same energy, $\sigma_{E,LArexpect}$, is given by the hadronic energy resolution [34] as

$$\left(\frac{\sigma_E}{E}\right)_{LArexpect} = \frac{\sigma_{E,LArexpect}}{E_{track}} = \frac{0.5}{\sqrt{E_{track}}}. \tag{6.6}$$

Each track is extrapolated to the surface of the calorimeter and a volume is defined corresponding to the intersection of a cone emanating from the track impact point and a cylinder inside the calorimeter, centred around the track impact point. Clusters inside this volume, hereafter referred to as the "cylinder", are associated to the track. The energy of clusters in the cylinder are summed to $E_{cylinder}$, with a resolution

$$\frac{\sigma_{E_{cylinder}}}{E_{cylinder}} = \frac{0.5}{\sqrt{E_{cylinder}}}. \tag{6.7}$$

Measurement Compatibility The relative resolution of the track measurement is compared to the relative resolution of the LAr expectation. The compatibility of the track measurement and the calorimeter measurement is then tested. HFS particles are

[2]The isolation criteria of electrons against clusters are defined in section 7.1. The isolation criteria of muons against tracks and clusters are defined in [51].

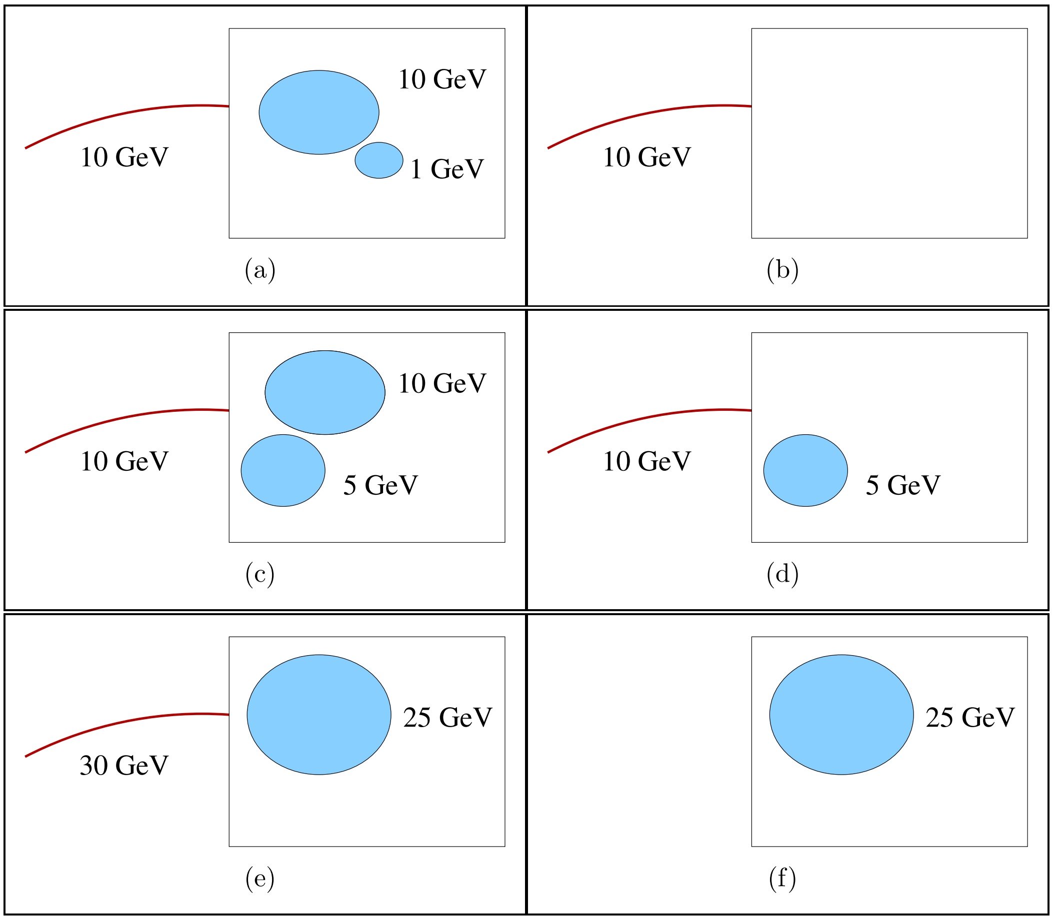

Figure 6.9: The behaviour of the HADROO2 algorithm is illustrated with three examples involving tracks and clusters. On the upper row, a 10 GeV track, which is measured with a 4% error, is kept and all calorimetric information removed. On the middle row, the track information is again kept but the energy deposited inside the calorimetric cylinder is determined to have a neutral component and only the track energy is subtracted from the calorimeter response. On the bottom row, the track is only measured with a 15% accuracy and the calorimetric information is used. This diagram is taken from [77].

formed in one of the following ways:

1. **Track measurement** The track measurement is used to define a particle candidate if it has the superior error. The energy in the cylinder is then compared to the measured track energy, taking into account possible fluctuations of both measurements within their standard errors. The well-measured E_{track} provides a constraint on the energy deposited by charged particles; so the calorimeter measurement is discarded unless $E_{cylinder}$ fluctuates more than 1.96σ (the 95% Confidence Level) above E_{track}. In this case, the discrepancy is attributed to neutral particles with energy $E_{cylinder} - E_{track}$, and the remaining calorimetric energy is suppressed.

2. **Calorimeter measurement** If the calorimeter measurement is favoured by the comparison of resolutions, the energy in the cylinder is compared to the measured energy of the track and:

   - if $E_{cylinder}$ is compatible with E_{track} within $\pm 1.96\sigma_{E_{cylinder}}$ then the better measurement from the calorimeter is used to define a HFS particle;
   - if $E_{track} < E_{cylinder} - 1.96\sigma_{E_{cylinder}}$, the track measurement is used and calorimetric energy is subtracted as in case 1 above;
   - if $E_{track} > E_{cylinder} + 1.96\sigma_{E_{cylinder}}$, the track is assumed to be poorly measured, and the calorimeter clusters alone are used to define the particle four-vector.

3. **Residual Cluster** Once all tracks have been considered, particle candidates are made out of remaining clusters. These particles correspond to either neutral particles with no associated track or to charged particles with a badly measured track.

The behaviour of this algorithm is illustrated in figure 6.9 with three examples of input tracks and clusters and the decision made by HADROO2.

The y-fraction contributed by each of the detector sub-systems is shown in figure 6.10 for data and MC. This demonstrates the division of the hadronic final state between LAr, SpaCal and Tracks by the algorithm described above. The fraction of y_h attributed to noise and removed (see section 6.2.1) is also shown. The fractional contributions by these subdetectors, and the y-fraction of subtracted noise, are well described by the simulation.

6.2.3 Hadronic Calibration

The determination of a well understood absolute hadronic energy scale is crucial to the analysis presented in this thesis, as the $e\Sigma$ kinematic reconstruction method requires a well measured hadronic final state. The response of the LAr calorimeter to hadrons is found to be dependent on their transverse momentum. The energy dependencies of the calibration are studied on the basis of reconstructed jets [77]. The jet finding algorithm used in this analysis is described by [79] and the implementation discussed in [51].

The implementation of the jet calibration is described in [77]. Briefly, the double angle kinematics (see equation 4.9) determine the reference scale, $p_T^{DA} = E_{DA} \sin\gamma_h$, in an analogous way to the electron calibration discussed in section 6.1. Calibration factors may be determined using DIS NC events in which the hadronic final state is formed by one jet.

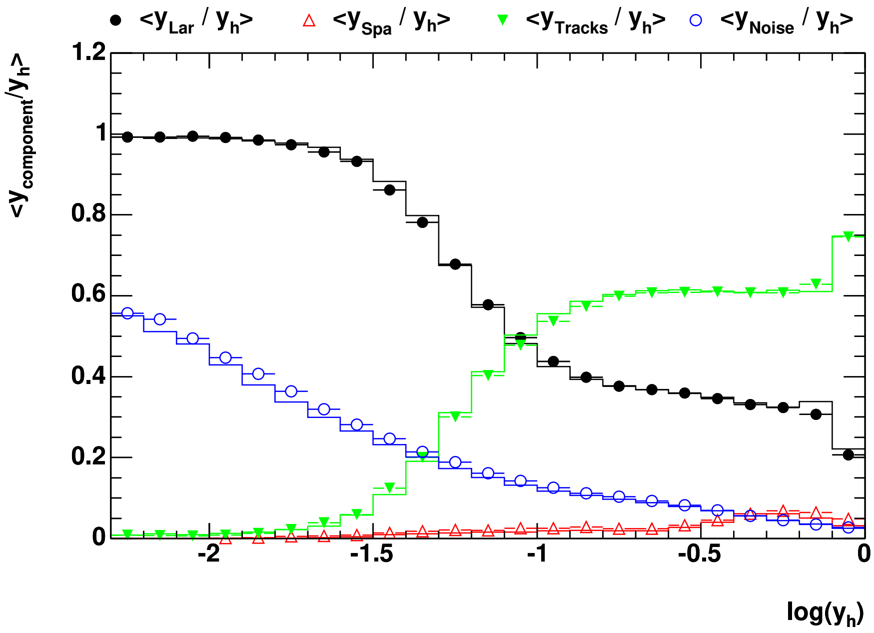

Figure 6.10: The fractional contributions to y_h by the tracks, the LAr and SpaCal calorimeters and the fractional contribution of subtracted noise.

The evolution of the momentum balance, $p_{T,Bal}^{DA} = p_T^h / p_T^{DA}$, with p_T^{DA} is parameterised by

$$F(\gamma_h, p_{T,Bal}^{DA}) = A_{\gamma_h}(1 - \exp^{-B_{\gamma_h} - C_{\gamma_h} p_T^{DA}}) \tag{6.8}$$

in several γ_h regions. This provides an absolute calibration of both data and MC.

However, a different choice must be made for the reference scale in the inclusive selection. The double angle prediction is only reliable in a subset of events and the total transverse momentum is, in general, shared between different jets. As a result, the calibration factors are applied jet-by-jet as a function of the jet polar angle, θ_{jet}, and the jet transverse momentum, $p_{T,jet}$. To approximate the "true" transverse momentum, an iterative procedure must be used. The uncalibrated jet transverse momentum is used in equation 6.8 to obtain the corrected $p'_{T,jet}$. This is then used to determine the final calibration factor for the jet.

A separate calibration must be applied to hadrons not belonging to reconstructed jets. A relative calibration is applied to the remaining hadrons in data to bring the hadronic response to that in the simulation.

The hadronic energy scale after calibration is demonstrated by figure 6.11. The calibrated hadronic final state is compared to the electron and double angle reference scales for the inclusive selection, listed in section 8.4. Agreement between data and MC is found to be within 2%.

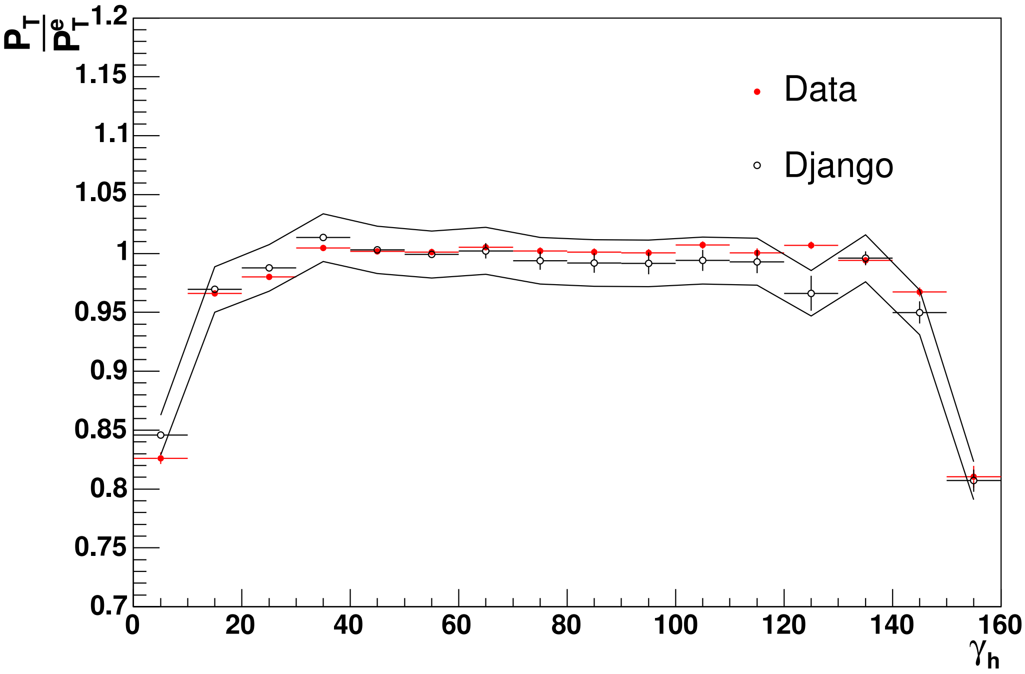

(a)

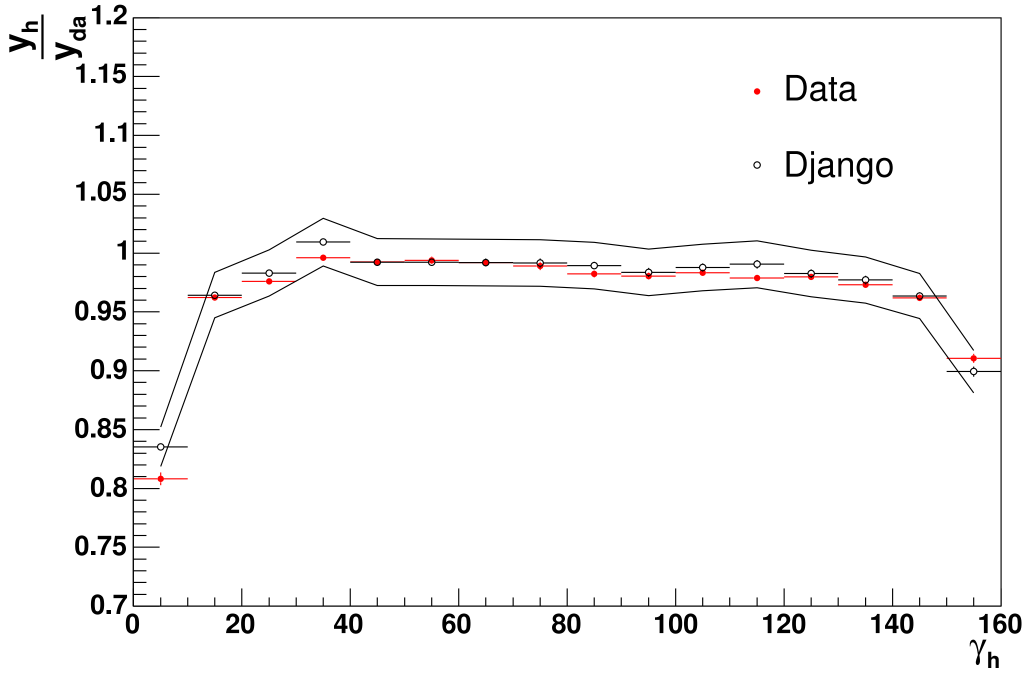

(b)

Figure 6.11: The mean values of (a) $p_{T,h}/p_{T,e}$, and (b) y_h/y_{DA} as a function of γ_h. The error bands correspond to a 2% variation around the simulation.

Chapter 7

Electron Measurement

The basis of the measurement of high Q^2 neutral current DIS at HERA is the identification of the scattered electron. The electron identification criteria in the LAr calorimeter are reviewed and the procedure for validating the scattered electron with a charged track originating from a well-defined event vertex is discussed. The efficiencies of each of these requirements are studied, and the results presented below. Finally, the precise measurement of the angle of the identified scattered electron is discussed.

7.1 Electron Identification

Electron candidates are identified on the basis of the clear characteristic signature of high energy electrons in the LAr calorimeter. That is compact, isolated clusters with a high transverse momentum. Identified electron candidates are tested for isolation against hadronic deposits, to flag electrons in jets. The electron finding algorithm [51] used in this analysis is an implementation of the QESCAT algorithm [80].

An electron shower envelope is defined by a cone of 7.5° around the centre of gravity (CoG) of each pre-selected cluster in the electromagnetic part of the calorimeter. The cone extends from the interaction vertex out to the first layer of the hadronic section. Any clusters within this envelope are merged with the "seed" cluster. Electron candidates are then identified on the basis of estimator variables, which quantify the shape and size of the electromagnetic shower. These seven estimator variables are described below, and summarised in table 7.1.

Electron candidate clusters are first required to be energetic and well defined:

- **EATOT** The electron cluster must have a minimum energy, $E_{tot} > 5$ GeV, together with high transverse momentum, $p_T > 3$ GeV.
- **NCEL** The cluster must consist of at least four calorimeter cells.

The next three estimator variables describe the compactness of the electron cluster.

- **EAEM** is the electromagnetic fraction of the cluster, defined as E_{em}/E_{tot}. Here E_{em} is the electromagnetic energy deposited in the first two (three in the forward region) layers of the electromagnetic part of the LAr. The minimum value for EAEM is θ dependent.
- **EAHN** is the energy fraction in the N hottest neighbouring cells, E^N_{Hot}/E_{em}. The value of N varies through the LAr and is 4 in the BBE, 8 in CB3 and in FB, and 12 in the IF wheel. EAHN is required to be greater than 0.8 (0.4) in the backward (forward) region.
- **EATR** is the transverse dispersion of the electron cluster, a measure of the cluster radius. $\sigma(R) = \sqrt{<r^2> - <r>^2}$, calculated from the energy-weighted transverse distances of all cells in the cluster, r_i.

Then an isolation cone is defined in $\eta - \phi$ space[1], with radius $R_{\eta-\phi} = \sqrt{(\Delta\eta)^2 + (\Delta\phi)^2} = 0.25$.

- **EAIF** is the fraction of deposited energy in the isolation cone, E_{iso}, that is associated with the electron candidate, E_{tot}/E_{iso}. EAIF must be at least 0.98.
- **EAHD** is the total hadronic energy deposited in the isolation cone. The EAIF cut can be lowered to 0.95 if EAHD < 300 MeV.

The chance of the electron finder mis-identifying a hadron as an electron is smaller than 1% [75]. However, an electron in a jet may still fake the scattered electron. The isolation of identified electromagnetic particles against other calorimeter deposits is tested by examining the total calorimetric energy not belonging to the electron, E_{cone}, in a cone of radius $R_{\eta-\phi} = 0.5$; electrons are flagged as isolated if $E_{cone}/E_{tot} < 5\%$. The highest p_T "isolated" electron is regarded as the scattered electron.

[1] $\eta = -\ln(\tan\frac{\theta}{2})$ is the pseudo-rapidity.

<table>
<tr><th>Estimator</th><th>Description</th><th>Cut</th></tr>
<tr><td>EATOT</td><td>Energetic cluster</td><td>$E_{tot} > 5$ GeV && $\mathrm{p_T} > 3$ GeV</td></tr>
<tr><td>NCEL</td><td>Cells assigned to electron candidate</td><td>> 3</td></tr>
<tr><td>EAEM</td><td>Electromagnetic fraction</td><td>$> 0.94 + 0.05\cos(2\theta)$</td></tr>
<tr><td>EAHN</td><td>Energy fraction in hot core</td><td>> 0.8 (0.4) in bwd (fwd) region</td></tr>
<tr><td>EATR</td><td>Cluster radius</td><td>θ dependent</td></tr>
<tr><td>EAIF</td><td>Energy fraction in isolation cone carried by electron candidate</td><td rowspan="2">> 0.98 $||$ (0.95 && EAHD $<$ 300 MeV)</td></tr>
<tr><td>EAHD</td><td>Hadronic energy in isolation cone</td></tr>
</table>

Table 7.1: The estimator variables used by the electron finding algorithm. Each estimator is briefly described and the cut values noted.

7.1.1 Electron Finding Efficiency

The efficiency of the electron finder must be high and well modelled in the signal MC. Since the electron finding algorithm is based on shower shape estimators, its efficiency must be studied with an electron finder that is independent of the shower shape. For this reason, a track-based electron finder has been developed [81]. Electrons identified by this track-based finder are used to monitor the efficiency of the default, cluster-based, electron finder. The efficiency is presented in figure 7.1 as a function of the extrapolated impact position of the electron track in the LAr. In this study, the background contribution in the data is removed through the subtraction of wrongly-charged tracks (refer to section 8.3.2 for a discussion of photoproduction background). The efficiency is generally very high, well above 99%, but drops in the cracks between octants, $|\phi_{wheel}| < 2°$. The efficiency can also be expected [75] to fall in the very backward part of the LAr BBE wheel, $z_{LAr} < -190$ cm, and in the crack between CB2 and CB3 wheels, $15 < z_{LAr} < 25$ cm.

Efficiency losses in z-cracks and ϕ-cracks are explained by electrons entering the crack and partially or completely bypassing the electromagnetic section of the calorimeter. Electron measurement is further complicated by showering in dead material inside the crack. Electrons entering the most backwards part of the BBE are also difficult to control experimentally; in this case the electromagnetic shower is not fully contained inside the calorimeter volume. While the inefficiencies are well reproduced by the simulation over most of the ϕ range, deviations inside the ϕ-crack exceed 5%. The inefficient z regions are harder to map in detail, due to the limited statistics provided by the track-based finder.

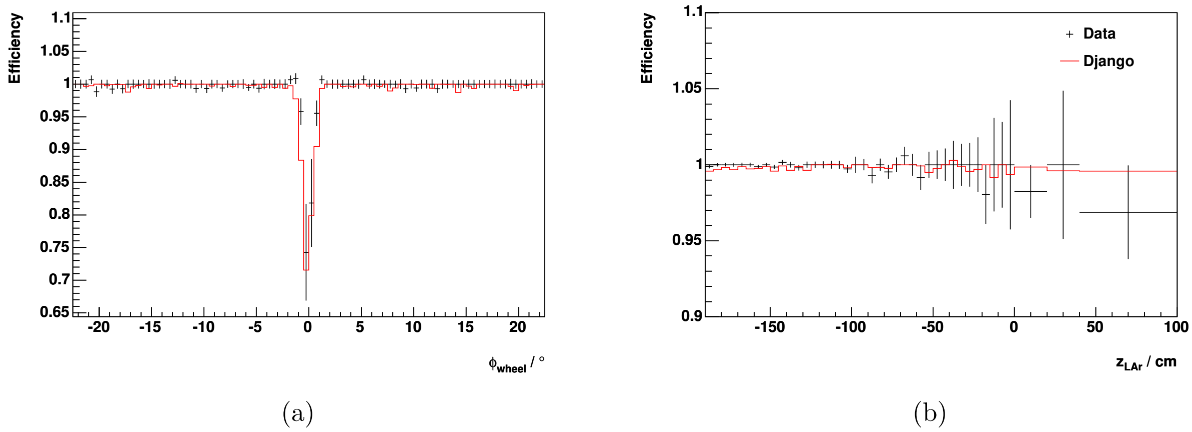

Figure 7.1: The electron finding efficiency, shown as a function of the impact position of the electron track in the LAr calorimeter: the ϕ_{wheel} position within the calorimeter octants in (a) and the z impact position in (b). The regions $\phi_{wheel} = 0 \pm 2°$ are excluded in (b), and the regions $z_{LAr} < -180$ cm and $15 < z_{LAr} < 25$ cm are excluded in (a).

However, as noted in section 6.1, the energy calibration is compromised in these regions. Therefore they are cut from the analysis.

7.2 Interaction Vertex

A well defined interaction vertex is required in order to discriminate against non-*ep* background and accurately reconstruct the event kinematics. In particular, the measurement of the polar angle, θ, of the scattered electron from the cluster relies on the reconstructed z position of the vertex. The behaviour of the vertex position must be modelled in detail by the simulation. Furthermore, the vertex reconstruction efficiency must be well described in the Monte Carlo.

7.2.1 Vertex Reconstruction Efficiency

The interaction vertex in an event is reconstructed from the origin of well-measured tracks. The track and vertex finding procedure is explained in more detail in section 7.4. For this analysis, the vertex is required to be reconstructed with a z_{vtx} position within 35cm of the mean vertex position over the whole run period, $|z_{vtx} - < z_{vtx} > | < 35$ cm where $< z_{vtx} >= 2.2$ cm.

The efficiency for finding an interaction vertex is studied with a special "clean NC" sample. The final NC selection listed in section 8.4 is modified; track and vertex requirements are relaxed, while additional cuts are added to eliminate background contamination. Events are required to be well balanced in both longitudinal momentum, $45 < E - p_z < 65$ GeV, and transverse momentum, $0.5 < p_{T,h}/p_{T,e} < 2.0$, in order to suppress non-ep and γp background. QED Compton background is almost completely eliminated by requiring exactly one electron in the event. Finally, the requirement $\eta_{max} > 3$ positively selects DIS events, as noted in section 8.3.

The vertex finding efficiency, defined as the proportion of events passing the selection that have a reconstructed vertex, is shown in figure 7.2 as a function of y_h. As can be seen from equation 4.4, y_h is a good estimator of the polar angle of the hadronic final state. The efficiency drops from 100% below $y_h \simeq 0.1$ where the tracks from the hadronic final state are beyond the acceptance of the central trackers; hence only the track associated to the electron is available to constrain the vertex. The vertex reconstruction efficiency could be improved at low y by making use of the forward tracker. Tracks caused by hadronic final state particles measured by the FTD could be used to define an interaction vertex; However, the behaviour of the upgraded forward tracker is not yet well understood, so this is not possible at this time. In order to model the central vertex reconstruction efficiency in this analysis, the simulation is down-weighted by 3% at low y ($\log(y_h) < -1.5$). No attempt is made to describe the falling edge of the efficiency in data, instead a 2% systematic uncertainty is assigned on the vertex reconstruction efficiency at low y ($y_h < 0.05$).

7.2.2 Vertex Reweight

The z position of the ep interaction depends on the beam optics and may change from fill to fill. The variation of the mean z vertex position with time is demonstrated in figure 7.3.

This causes the mean z vertex position to be shifted from zero; this can be seen in figures 7.4(a) and 7.4(b), which demonstrate the z vertex distribution for the LH and RH datasets, respectively. The Monte Carlo events are simulated with a broad Gaussian z_{vtx} distribution centred around 0.0 cm, so do not reproduce the behaviour of the data. A good level of agreement between data and Monte Carlo can be achieved by reweighting the MC vertex distribution to that seen in data, for each of the sub-periods identified in figure 7.3. After the reweight is applied, the distribution is well described by the MC

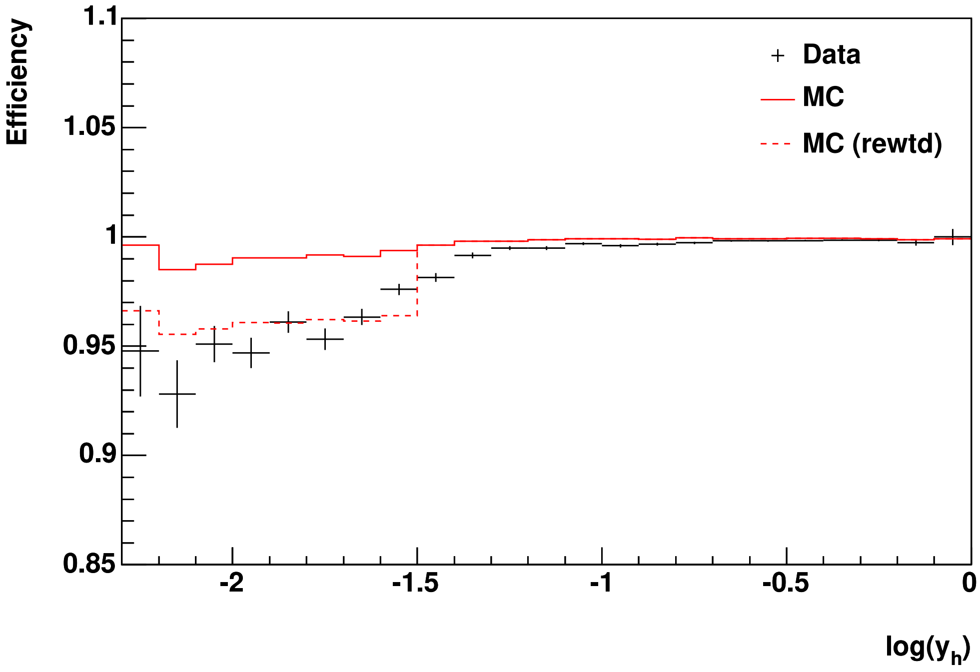

Figure 7.2: The efficiency for reconstructing an interaction vertex with the central tracker. The inefficiency seen in the data at low y_h is roughly modelled the down-weighted MC (dashed line).

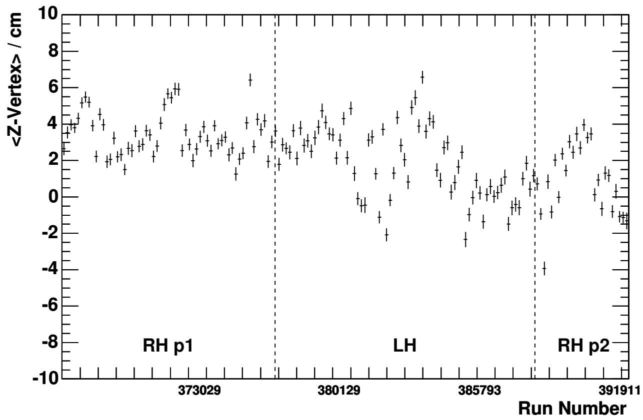

Figure 7.3: The time dependence of the mean z_{vtx} position.

as can be seen in figure 7.4. As noted above, events are cut from the analysis if the interaction vertex is reconstructed with $|z_{vtx} - < z_{vtx} > | > 35$ cm. Contributions from late satellite bunches(see section 3.6) cause long tails outside this region. These are hard to control, and are not modelled in the Monte Carlo.

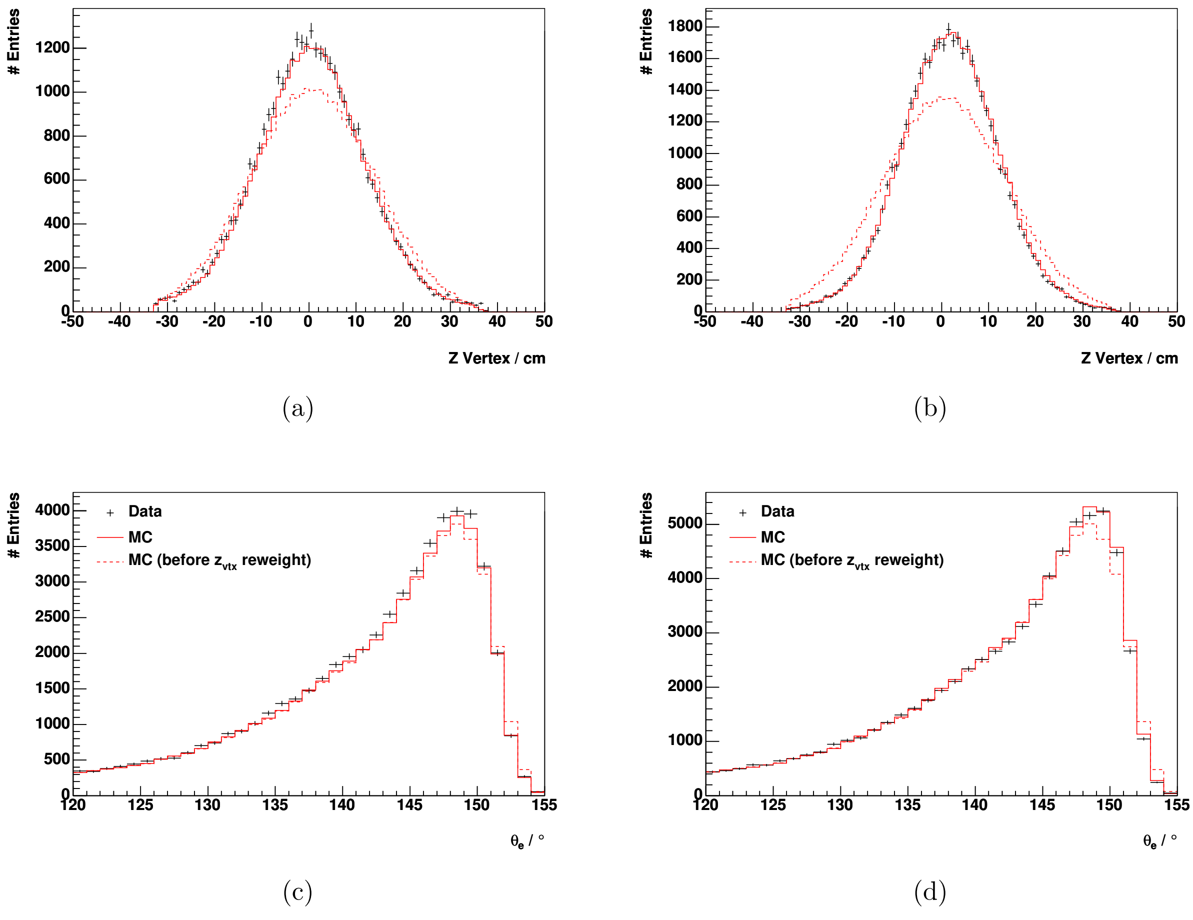

(a) (b) (c) (d)

Figure 7.4: The z vertex distribution in the LH (a) and RH (b) data-sets. The MC (histogram) is simulated with an ideal Gaussian distribution, so does not reflect the behaviour of the data. After a reweight, the Monte Carlo describes the data in both datasets well. The z_{vtx} distributions are made for events with $\theta_e < 145°$ only to avoid biases due to the z_{LAr} cut. The improvement in the description of the θ_e behaviour of the data by the reweighted MC is illustrated for the LH (c) and RH (d) datasets.

The importance of correctly modelling all the features of the z vertex distribution is illustrated by the θ_e reconstruction. The value, z_{LAr}, of the impact point of the electron in the LAr depends on the vertex position. Events at high z_{vtx} correspond to higher values of θ_e, and hence lower Q^2, at a given z_{LAr}. Thus an excess of MC events in the tails of the z_{vtx} position results in an excess of events passing the $z_{LAr} > -190$ cm cut, at the lowest Q^2. The improved description of θ_e after the z_{vtx} reweight is seen in figure 7.4.

7.3 Track Validation

Once an electron candidate is identified by the electron finder, it is validated by requiring a track link to the cluster. This requirement efficiently rejects background due to an energetic π^0 faking the scattered electron.

Track measurements that can be fitted to the interaction vertex are referred to as DTRA tracks. Non-vertex-fitted track segments are referred to as DTNV tracks. The scattered electron is validated by extrapolating a track to the LAr surface, following the procedure outlined in section 7.4.1, and demanding the smallest distance of closest approach (DCA) to the centre of gravity of the electron cluster. The behaviour of the DCA of the nearest DTRA track to the cluster is demonstrated in figure 7.5. The distribution peaks at low values for NC DIS and is rather flat for background processes.

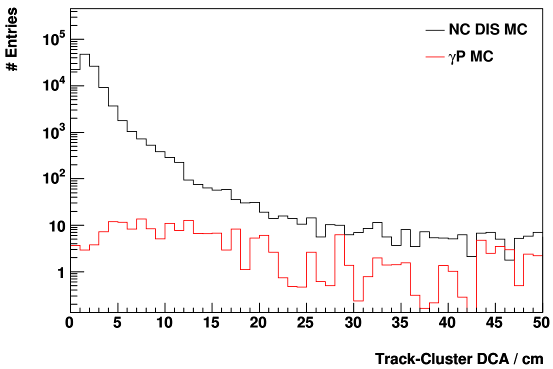

Figure 7.5: The distance of closest approach between the electron track and the LAr cluster, for vertex-fitted tracks.

The scattered electron is validated by a DTRA track if the DCA to the cluster is less than 12 cm. Otherwise, non-vertex fitted tracks validate the electron if they have a DCA to the cluster less than 12cm, and a DCA from the track to the vertex of less than 5cm.

No track validation requirement is made for $\theta_e < 30^\circ$ as this falls outside the geometrical acceptance of the central tracker.

The efficiencies of the DTRA and DTNV track validation are studied with the "clean NC" sample defined in section 7.2.1. The measured inefficiencies [82] are applied to the MC in order to correctly model the data. The efficiency for finding DTRA tracks, shown in figure 7.6(a) as a function of ϕ_e, is about 94%. The track finding efficiency is improved if both DTRA or DTNV tracks are used and the combined efficiency, shown in figure 7.6(c), is around 98%. The θ_e dependence of the combined efficiency, shown in figure 7.6(d), is well described by the MC. The combined track efficiency is also shown as a function of y_e in figure 7.6(b).

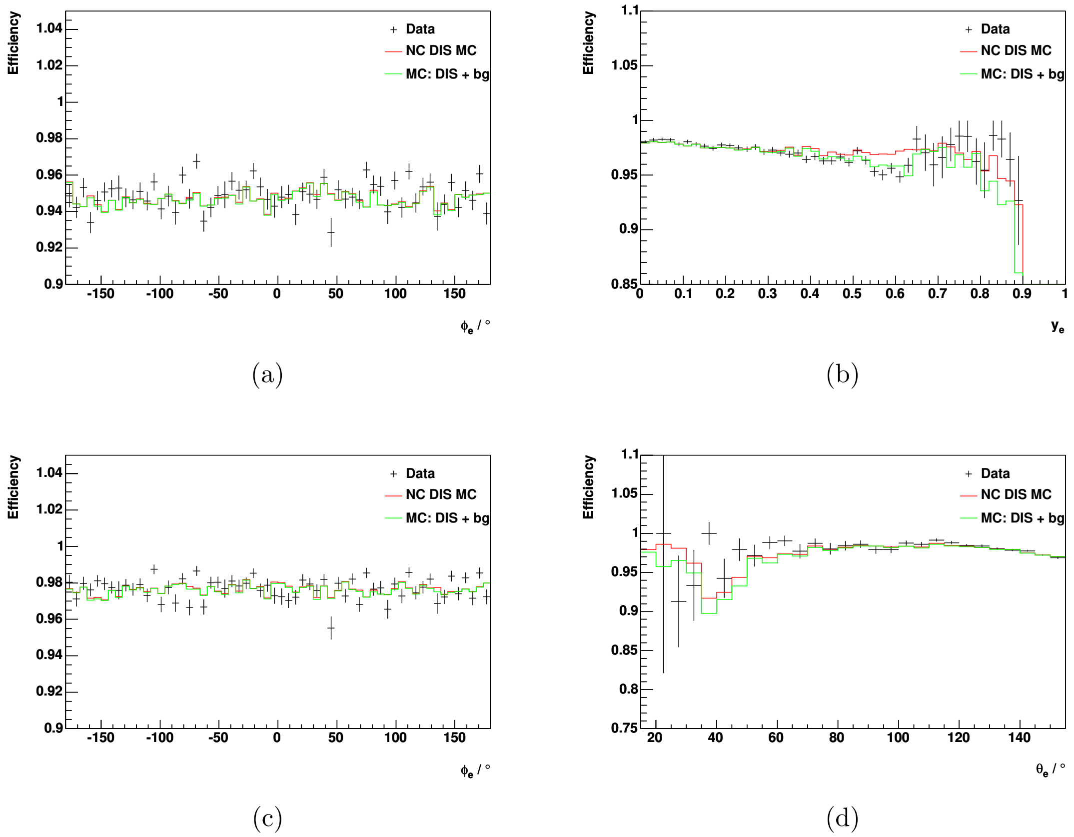

Figure 7.6: The efficiency for linking a DTRA track to the scattered electron is shown as a function of θ_e in (a). The combined efficiency for linking either a DTRA or DTNV track is shown as a function of (b) y_e, (c) ϕ_e and (d) θ_e. The efficiencies are shown for events with $E'_e > 18$ GeV.

7.4 Electron Angle Measurement

The polar, θ_e, and azimuthal, ϕ_e, angles of the scattered electron at the interaction vertex can be obtained from either (a) the position of both the cluster measured in the LAr calorimeter and the interaction vertex, or (b) the track associated to the electron, if there is one. For case (a), the LAr calorimeter has to be aligned with respect to the central tracking system. The central tracking system defines the H1 coordinate system.

The reconstruction of charged particle tracks is described in [23]. Briefly, track segments are found by fitting a helical path to hits in CJC wires. The track fitting can be improved by introducing the vertex as a constraint. The ep interaction region extends over a few tens of μm in the xy-plane with a mean value that typically stays constant over several runs. The known x and y position of the interaction vertex can then be used to improve the track fit by providing an extra constraint. The z position of the vertex is obtained from these vertex fitted tracks. The tracks that can be fitted to the interaction vertex are known as DTRA tracks. Non-vertex-fitted tracks are known as DTNV tracks. Vertex-fitted tracks that fulfill further quality criteria [51] are referred to as "Selected" tracks.

7.4.1 Track Extrapolation

Charged particles follow a helical trajectory in the H1 detector due to the 1.16 T solenoidal magnetic field. The determination of the impact position of the track in the LAr calorimeter is necessary in order to compare track measurements with energy deposits in the calorimeter. The track extrapolation method used in this analysis is briefly described below and is documented in [51].

The track trajectory is described by five parameters: the x, y, z coordinates of the track starting point, the polar, θ, and initial azimuthal angle, ϕ, of the track vector with respect to the vertex, and the curvature of the track. The progression of x and y and ϕ as the track moves outwards in the $r - \phi$ plane can be calculated.

The track position is extrapolated out to the nominal radius of the LAr calorimeter at 105 cm and an iterative approach is used to find the intersection of the track with the octagonal LAr surface. A complication arises from the BBE wheel, which has a 16-fold geometry. Some particles may enter the BBE through the front face of the wheel, in a region where there is no overlap with the CB1 wheel (these regions are illustrated in figure 7.7). It may then not be possible to determine an unambiguous point of impact

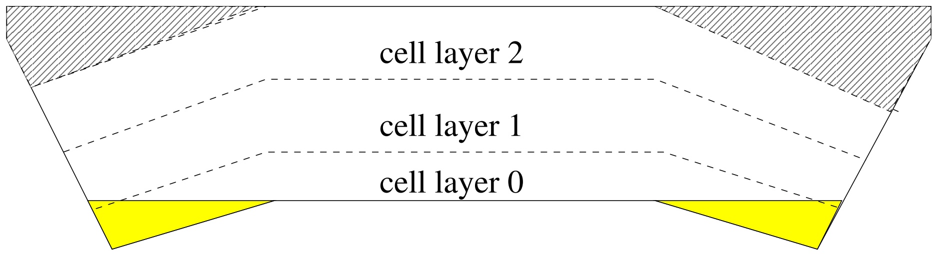

Figure 7.7: Schematic view of a BBE octant. The shaded areas indicate the regions where there is no overlap with the CB1 wheel.

with either wheel and the z impact position is assigned to the front face of the BBE, at -152.5 cm.

7.4.2 Beam Tilt

The ep interaction axis does not coincide with the z axis of the H1 coordinate system. The beams are inclined at a small angle, σ_x and σ_y in the x and y direction. This "beam tilt" is corrected in the data, effectively aligning the central tracking system to the beam.

7.4.3 Alignment of the LAr calorimeter

The alignment of the LAr calorimeter to the central tracking system is described below.

The alignment is performed following the procedure used in previous analyses as outlined in [83]. Briefly, the alignment consists of two steps. First, a correction is made for the shrinkage of the LAr calorimeter due to the low temperature of the liquid Argon. Then the position of the LAr calorimeter is adjusted to conform with the H1 coordinate system. This adjustment consists of a rotation about and a shift of each axis.

Shrinkage of the LAr calorimeter

The dimensions of the calorimeter have been determined at room temperature. The operating temperature of 72 K causes a contraction of the calorimeter in the z direction, which has been parameterised as

$$z_{cold} = 23.67 \text{ cm} + (\mathrm{z_{warm}} - 23.67 \text{ cm}) \cdot (1 - 0.027). \tag{7.1}$$

Alignment of the LAr calorimeter to the CJC

The calorimeter is aligned to the central tracking system by three rotations and three translations, defined in equations 7.2-7.4 and 7.5 respectively. These are determined from comparison of the extrapolated impact position of the tracks with the centre of gravity of the calorimeter cluster. Central Tracker tracks are extrapolated to the nominal calorimeter surface using the method described in section 7.4.1 and the cluster position is taken from a projection along the line between the vertex and the cluster CoG, where it meets the nominal calorimeter surface.

rotations:

$$x_1 = x_0 \qquad y_1 = y_0 \cos\alpha - z_0 \sin\alpha \qquad z_1 = z_0 \cos\alpha + y_0 \sin\alpha \tag{7.2}$$

$$x_2 = x_1 \cos\beta + z_1 \sin\beta \qquad y_2 = y_1 \qquad z_2 = z_1 \cos\beta - x_1 \sin\beta \tag{7.3}$$

$$x_3 = x_2 \cos\gamma - y_2 \sin\gamma \qquad y_3 = y_2 \cos\gamma + x_2 \sin\gamma \qquad z_3 = z_2 \tag{7.4}$$

where the subscript 0 refers to the unaligned coordinate system,
and the subscripts 1, 2 and 3 refers to the coordinates after a rotation about the x, y and z axis respectively.

translations

$$x_f = x_3 - \Delta x, \qquad y_f = y_3 - \Delta y, \qquad z_f = z_3 - \Delta z. \tag{7.5}$$

The alignment constants obtained [82] are summarised in table 7.2 and applied in the order given. They are demonstrated in figure 7.8.

rotations:		
α	0.0 mrad	around x axis
β	-1.0 mrad	around y axis
γ	0.0 mrad	around z axis
translations:		
Δx	$+0.16$ cm	in x direction
Δy	-0.36 cm	in y direction
Δz	0.00 cm	in z direction

Table 7.2: The parameters for the alignment of the LAr calorimeter.

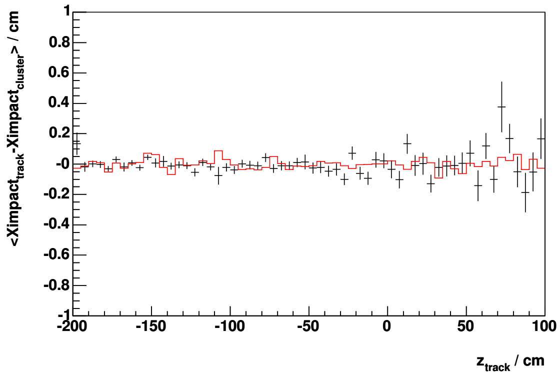

(a)

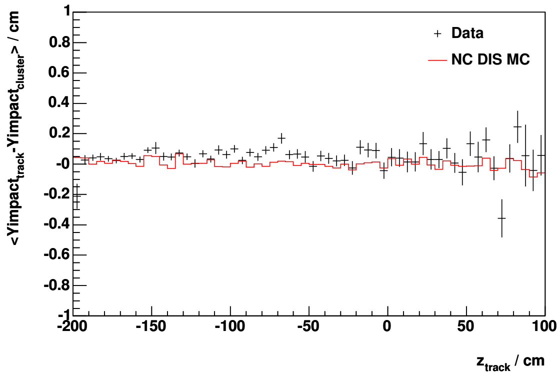

(b)

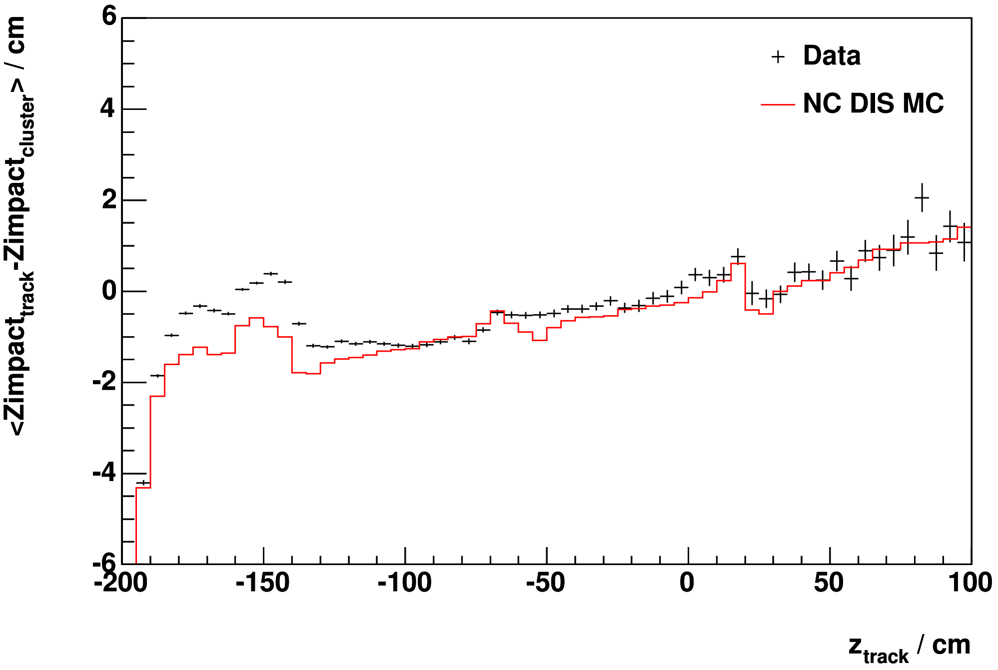

(c)

Figure 7.8: The shifts between track and cluster measurements after alignment of the LAr calorimeter.

After this alignment the remaining mis-alignments, δx and δy, between the track and cluster measurements, displayed in figure 7.8, are small. The track - cluster discrepancy δz is not yet fully understood. There is a ≈ 1.0 cm discrepancy between the data and the simulation in the region near z cracks and in the BBE. Additionally, these is a z dependent mis-alignment observed in both the data and the simulation. This is attributed to the bias of the calorimetric measurement due to shower evolution in the cells [75]. This effect is not corrected for in this analysis.

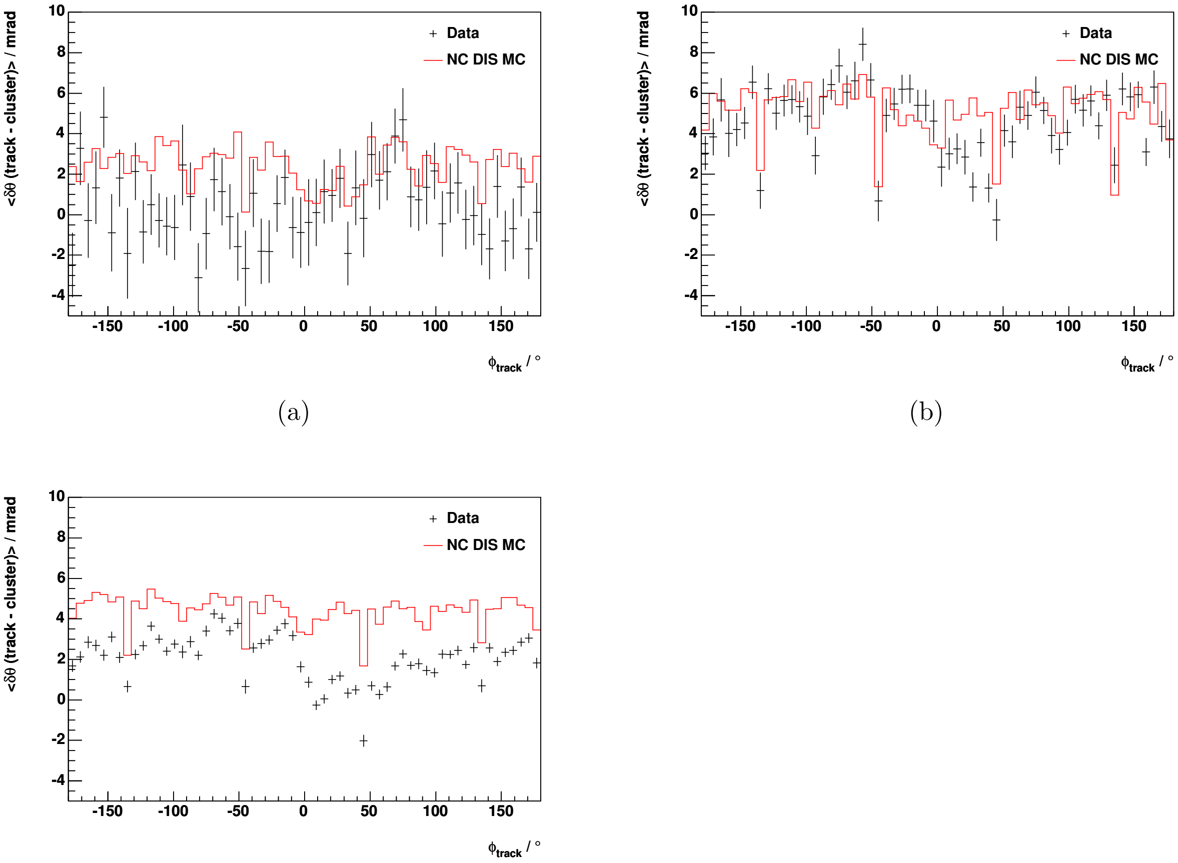

(a) (b) (c)

Figure 7.9: The track-cluster θ_e difference as a function of ϕ_e in different regions of the detector: (a) $\theta_e < 120°$, (b) $120° < \theta_e < 135°$, (c) $\theta_e > 135°$.

The CJC and LAr measurements of the scattered electron polar angle, θ_e, are compared after alignment in figure 7.9, as a function of ϕ_e, in several regions of the detector. They are in reasonable agreement within the quoted systematic uncertainty of $3 \oplus 3$ mrad and are consistent between data and simulation in the central (figure 7.9(b)) and forward (figure 7.9(a)) parts of the detector. The imperfect alignment of the LAr to the CTD may be attributed to the lack of precise z measurements from the CJC alone. The CIP and the COZ are presently unable to provide a precise θ determination. Hence the correlated part of the systematic uncertainty arises from the estimated uncertainty on the polar angle measurement. Studies into the central tracking performance are ongoing.

7.4.4 Angle Determination

The polar angle measurement provided by the CJC is poor compared to that of the LAr, due to the inferior z resolution[2]. The θ_e measurement is taken from the LAr.

The CJC is optimised for track measurement in the $r - \phi$ plane. Therefore the superior resolution of the CJC is used to provide ϕ_e if there is a DTRA track linked to the scattered electron. Otherwise, the azimuthal angle is determined from the position of the LAr cluster (and the interaction vertex).

As noted elsewhere, the Forward Tracker does not provide a reliable track measurement. Tracks entering the Forward Track Detector are difficult to control. Forward going tracks tend to shower in the dead material between the CJC and the FTD. Then, in the forward region, $\theta_e < 30°$, the calorimeter cluster must provide both the azimuthal and polar angle measurement.

7.5 Summary

The identification and validation of the scattered electron in neutral current DIS has been discussed in this chapter. The electron identification algorithm was discussed and the electron finding efficiency found to be excellent. The electron candidate is validated by linking the calorimeter cluster to a charged track. The optimum track finding efficiency was gained by allowing tracks not fitted to the vertex to validate the electron if no well measured track exists. The overall track linking efficiency was studied and found to be $\approx 98\%$ and the simulation was corrected to match the small inefficiencies found in the data.

A well measured event vertex is needed for the best electron polar angle measurement by the calorimeter. The vertex finding efficiency was studied and found to be excellent in the central region, but to fall off as tracks from the hadronic final state leave the acceptance of the central tracker. The simulation was adjusted in this region to better model the data, but a 2% systematic error is needed at low y to cover this effect. The Gaussian behaviour of the z vertex position in the simulation has been reweighted to match that found in data since the ep interaction point depends on the beam conditions in HERA.

[2]Tracks measured in the COZ may have a superior z resolution. However the performance and efficiency of this subdetector has not yet been studied at HERA II.

Finally, the polar angle measurement of the scattered electron was discussed. The LAr calorimeter must be aligned to the Central Tracker, which defines the H1 coordinate system. The residual discrepancies in the x, y and z coordinate measurements between the trackers and the aligned calorimeter were studied and used to assign a 3 mrad systematic uncertainty to the polar angle measurement. An additional 3 mrad systematic uncertainty is assigned to the limited z precision of the CJC alone.

The identification and precise measurement of the scattered electron is critical to the measurement of neutral current cross sections. Now that the scattered electron measurement in the H1 detector is well understood, the next chapter will concentrate on global event selection issues and background rejection.

Chapter 8

Selection

In this chapter the neutral current event selection used in this analysis is summarised. The selection is based on that used in previous analyses, [75] and [83], of HERA I data [3]. This analysis builds on the work of [55] and was developed in parallel with [84].

Events are selected from periods when the subdetectors essential to this analysis were operational and the integrated luminosity of the data sample calculated accordingly. The triggers used to obtain the data are reviewed, and their selection efficiency studied. Then the procedures used to combat contamination from background processes are discussed. Finally, the event selection criteria discussed in this chapter and previous chapters are summarised. The control of the event sample is demonstrated by plots of the most important kinematic quantities.

8.1 Run Selection

During data taking, events are collected into runs with nominally stable detector conditions. However, detector and beam conditions can vary from run to run, so a *Good Run* Selection is necessary. Runs are accepted into the Neutral Current analysis if all subdetectors essential to the analysis were supplied by high voltage (HV) over the course of the run. The HV status of each subdetector is recorded at 10 second intervals and an event in a selected run is kept only if it occurred at a time when all subdetector HV requirements were met. Runs are rejected if any of the required subdetectors were off for the whole of the run, or not enabled in the data acquisition output stream. The luminosity associated with a run is adjusted for periods in which the HV conditions are not met. More detail on the luminosity measurement can be found in section 3.6.

The required subdetector components for this analysis are the central jet chambers (CJC1 and CJC2), the central proportional chamber (CIP) and the LAr calorimeter, which trigger and measure the final state and reject background events. Also required are the ToF system, vital to reducing background, and the Luminosity detectors (see section 3.6) and the Polarimeters (see below for further details). Runs are also rejected if the high Q^2 triggers, described in section 8.2, are not enabled.

8.1.1 Polarisation Selection

The technical aspects of the polarisation measurement are discussed in section 3.1.1. The polarisation is primarily measured by the LPol polarimeter. If no LPol measurement is available, then the TPol is used. If neither polarimeter operational at the time an event is taken, the event is rejected. The luminosity is adjusted for the portion of collected luminosity over which a polarisation measurement is available, in a similar manner to the HV luminosity correction.

8.1.2 Event Yield

The stability of the event yield per nb^{-1} integrated luminosity is demonstrated in figure 8.1. The demarcations between helicity periods are shown as dotted lines in figure 8.1.

The corresponding values of electron polarisation can be seen in figure 8.2. The Left-Handed (LH) dataset amounts to 20.72 ± 0.27 pb^{-1} with a mean polarisation of $-40.2 \pm 1.1\%$, and the Right-Handed (RH) dataset consists of 26.91 ± 0.35 pb^{-1} integrated luminosity with $33.6 \pm 0.7\%$ mean polarisation. The Right-handed data was collected over two run periods, denoted as "RH p1" and "RH p2". The mean event yield for data taken in RH p2 is $\approx 2\%$ lower than the event yield in the bulk of the data-taking. This effect has not yet been traced to any known source, however it is of a comparative size to the uncertainty on the luminosity measurement, 1.3% (see section 3.6).

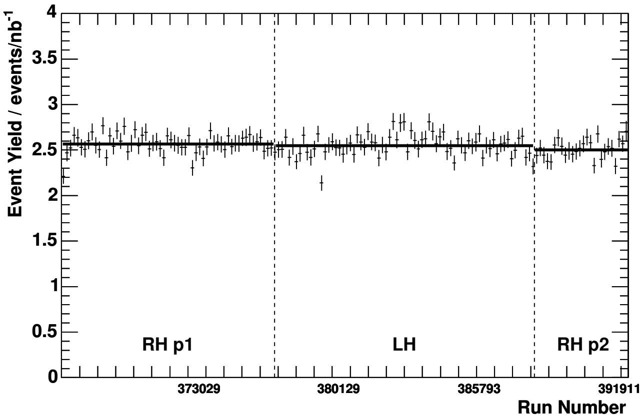

Figure 8.1: The event yield per nb^{-1}, shown as a function of run number. The boundaries between helicity periods are indicated by dotted lines. The mean yield in each of the helicity periods is depicted by the full lines

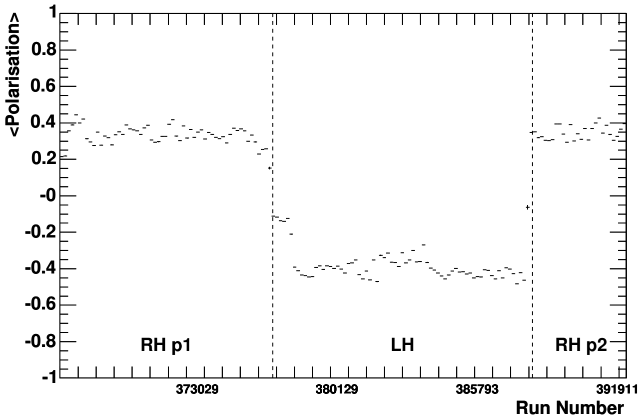

Figure 8.2: The time dependence of the electron polarisation. The binning is the same as that in figure 8.1.

8.2 Event Triggering

8.2.1 Neutral Current Trigger Elements

The triggering of neutral current events is based on the identification of a high energy deposit in the LAr calorimeter. Timing information from the LAr or the CIP reduces the chance of triggering on electronic noise in the calorimeter. Combined with vetoing of beam-related background by ToF systems and the CIP, NC events are triggered with a reasonable rate of a few Hz. Thus the Neutral Current subtriggers are run without any prescales. The trigger elements used in the subtriggers below[1] are described in section 3.7.1.

s67 LAr_electron1 && (CIP_T0 || (LAr_T0 && !CIP_nextbc))

s77 (CIP_sig>0 && LAr_Etmiss>1) && (CIP_T0)

The main NC subtrigger, **s67**, is based on the *LAr_electron1* trigger element, which identifies a high energy deposit in the electromagnetic LAr calorimeter, together with an absence of energy in the hadronic section behind it. Subtrigger **s77** complements **s67** as very high energy calorimetric deposits which saturate the FADCs are recognised as missing energy. The CIP trigger elements demand that the majority of tracks are consistent with an *ep* event; this combats the fake rate from LAr noise coincident with non-*ep* background. As noted above, both subtriggers mentioned here carry veto conditions. These are discussed in further detail in section 8.2.4.

The efficiency of each Trigger Element comprising **s67** is studied using an independent monitor trigger (MT). The TE efficiency is

$$\varepsilon_{TE} = \frac{\text{number of events triggered by TE and MT}}{\text{number of events triggered by MT}} \tag{8.1}$$

Two mutually independent trigger efficiencies, condition A and condition B, can be combined, using equation 8.2, to form the efficiency of A OR B:

$$\begin{aligned} \varepsilon_{AB} &= \varepsilon(A \quad || \quad B) \\ &= \varepsilon(A) \, + \, [\, 1 \, - \, \varepsilon(A) \,] \, \cdot \, \varepsilon(B) \end{aligned} \tag{8.2}$$

8.2.2 Energy Condition

The efficiency of the *LAr_electron1* TE rises steeply with electron energy above the trigger threshold [75] and plateaus at $\simeq 100\%$ for energies $E'_e > 11$ GeV. This is therefore taken as the minimum electron energy cut and local inefficiencies of the trigger element are studied further.

Since there were no independent subtriggers available to monitor the efficiency of the *LAr_electron1* trigger element the efficiency has to be evaluated with an alternative

[1]Here && symbolises a logical AND, || a logical OR

method. Trigger level information on the calorimeter Big Towers (see section 3.7.1 for an overview of the LAr trigger system) can be exploited to study the trigger efficiency [52]. The efficiency of the LAr triggering on an electron deposit is evaluated using those Neutral Current events in which the hadronic final state caused the *LAr_electron1* TE to fire. In turn, the efficiency for triggering on the hadronic final state is studied with events in which an electromagnetic deposit cause *LAr_electron1* to fire. The efficiency for triggering on hadrons is independent of the efficiency for triggering on electrons, so that the combined trigger efficiency can be estimated using equation 8.2.

The *LAr_electron1* trigger efficiency is evaluated as a function of z_{LAr} and ϕ_{LAr} and found to be very high over most of the detector volume, but less in some regions. The efficiency is mapped on a $z - \phi$ grid in figure 8.3. Inefficient regions, highlighted by red boxes, are excluded from the analysis. After these fiducial cuts, the *LAr_electron1* efficiency is consistent with 100%.

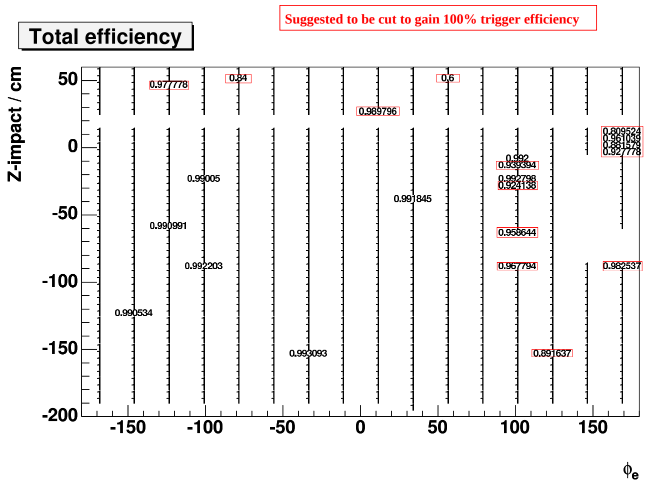

Figure 8.3: The efficiency of the trigger element *LAr_electron1*, presented in a $z - \phi$ grid [85]. Inefficient regions, highlighted by red boxes, are cut from the analysis.

8.2.3 Timing Condition

The T0 trigger elements allow events to be triggered on the basis of the bunch crossing of the interaction. The high Q^2 subtriggers use T0 information from the LAr calorimeter and the CIP proportional chamber. The efficiency of the T0 trigger elements can be seen in figure 8.4. The efficiency of *LAr_T0* depends strongly on the scattered electron energy (see figure 8.4(a)) rising from $\approx 85\%$ at 11 GeV to $\approx 95\%$ at 27.5 GeV. The efficiency drops at around $E'_e = 32$ GeV, corresponding to the electron scattering into a part of the LAr central barrel where some trigger towers are deactivated, but continues to perform well at higher electron energies. The *CIP_T0* has a consistently high efficiency across the whole kinematic range.

Under the assumption that the T0 trigger elements are mutually independent, the combined Trigger Efficiency (given by equation 8.2) is everywhere close to 100%.

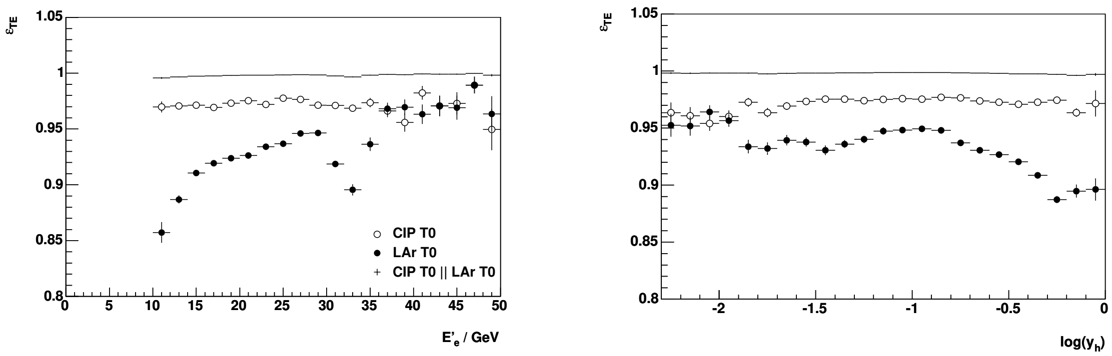

(a) (b)

Figure 8.4: T0 trigger efficiencies as a function of (a) Electron Energy, and (b) $\log(y_h)$.

8.2.4 Veto Condition

The veto conditions in subtriggers **s67** and **s77** are described in section 3.7.1. The veto conditions use time-of-flight (ToF) information to reject out of time background events. In addition, the CIP is able to veto background from beam-collimator interactions on the basis of the z vertex origin of tracks.

The signal inefficiency due to these veto conditions, i.e. the chance of rejecting good ep events is continuously monitored with the subtrigger **s57**. This monitor trigger is a copy of **s67** without the veto conditions applied, and a prescale to keep the rate manageable. For most of the data period under study, **s57** monitors the *CIP_veto* condition only. For the last part of the running, however, **s57** was loosened so that it contained no veto conditions[2]. The inefficiency was found to be quite high - $0.28 \pm 0.04\%$ from the CIP-Veto, and $1.4 \pm 0.1\%$ for all veto conditions[3].

[2]The ToF-based vetos are ideally monitored using dedicated runs with no veto conditions applied. Unfortunately, there are no such runs available for high Q^2 events in the data period under study.

[3]The largest contributor to the inefficiency among the ToF systems was the BToF [86].

A correction of 1.4% is applied to the Monte Carlo. Additionally, a systematic uncertainty of 0.5% is assigned on the trigger efficiency determination due to this effect.

8.3 Background Rejection

Two distinct classes of background can contribute to the NC event sample. These are non-*ep* background, induced by muons from cosmic rays or beam-halo muons, and background arising from *ep* collisions. The methods used to efficiently reject these sources of background are discussed in this section.

DIS events are typically characterised by forward hadronic activity, due to the proton remnant and colour string to the struck quark. For this reason, events with a very forward cluster, $\eta_{max} > 3$, are not considered as potential background[4].

8.3.1 Non-*ep* background

Cosmic and beam halo muons can cause electromagnetic showers in the calorimeters, faking an electron. Requiring an interaction vertex and track-cluster linking alone reduces this background to a small level. Additional discrimination can be made on the basis of the timing of the event, as obtained by the central jet chamber, and by topological background finders.

The Central Jet Chamber (described in section 3.3) can measure the event timing from the drift time of charged tracks to the CJC wires, with a resolution of ~ 1 ns. An event coming more than 5 ns from the bunch crossing time[5] is unlikely to have arisen from an *ep* interaction, and is rejected if $\eta_{max} < 3$. The inefficiency of this cut is estimated, from the "clean NC" selection outlined in section 7.2.1, as $0.016 \pm 0.001\%$.

The majority of the remaining background events are identified by a set of dedicated topological finders [87]. These background finders identify non-*ep* background from beam-halo or cosmic muons on the basis of their topological signature. While the finders are designed to identify non-*ep* background for charged current analysis, a subset of the finders that efficiently reject background without rejecting NC events is used in this analysis [88].

[4] η_{max} is defined as the η of the most forward cluster in the calorimeter with at least 400 MeV deposited energy.

[5] Due to problems with the HERA clock in 2003, the $T0$ timing recorded by the CJC was shifted by $\simeq 10$ ns for some events. This is taken into account in the CJC timing selection

The finders are applied when an event does not exhibit the ideal NC characteristics: being well balanced in transverse momentum, $0.5 < p_{T,h}/p_{T,e} < 2.0$ or having non-negligible forward activity, $\eta_{max} > 3$.

8.3.2 *ep* background

Background processes that arise from *ep* interactions cannot be rejected on the basis of event timing. Processes such as photoproduction, QED Compton scattering, lepton pair production and W Production can fake a Neutral Current event; see section 5.3 for more details on these processes and how they may enter the NC selection.

Photoproduction events enter as background when the scattered electron escapes down the beam-pipe, and part of the hadronic final state fakes an electron. The contribution of photoproduction events is efficiently reduced by requiring a track-cluster link for the scattered electron, as can be seen in section 7.3. The background is further reduced by constraining the "longitudinal energy balance" in the event, $E - P_z$, as defined in section 4.3. HERA kinematics are such that $E - P_z = 2E_e = 55$ GeV, and this would be measured in a hermetic detector with perfect resolution. A requirement $E - P_z > 35$ GeV removes photoproduction events, in which the final state is not well constrained by the detector due to the escaped electron.

Remaining photoproduction events are found at high y_e, as can be seen in figure 8.5. Photoproduction dominates at $y_e > 0.9$, so this region is cut in this analysis. The high y region is kinematically forbidden at $Q^2 < 890$ GeV by the cut $E'_e > 11$ GeV (see section 9.1).

Elastic QED Compton and $\gamma\gamma$ events have the distinct signature of two electromagnetic particles together with no hadronic deposit, accompanied with either one or two tracks. Potential background events are identified by the low hadronic fraction in the LAr, $E_{Had}/E_{Tot} < 10\%$. These events are rejected if they have a low track multiplicity, or if they do not have forward hadronic activity (see discussions on η_{max}, above).

W Production events, from γp interactions, contribute a tiny background, when the W particle decays leptonically in this small cross-section process. As the contribution to the background is tiny, no action needs to be taken to discriminate against these events.

The residual background from all these processes is small, and well understood. The background contamination can then be modelled by the Monte Carlo simulations listed

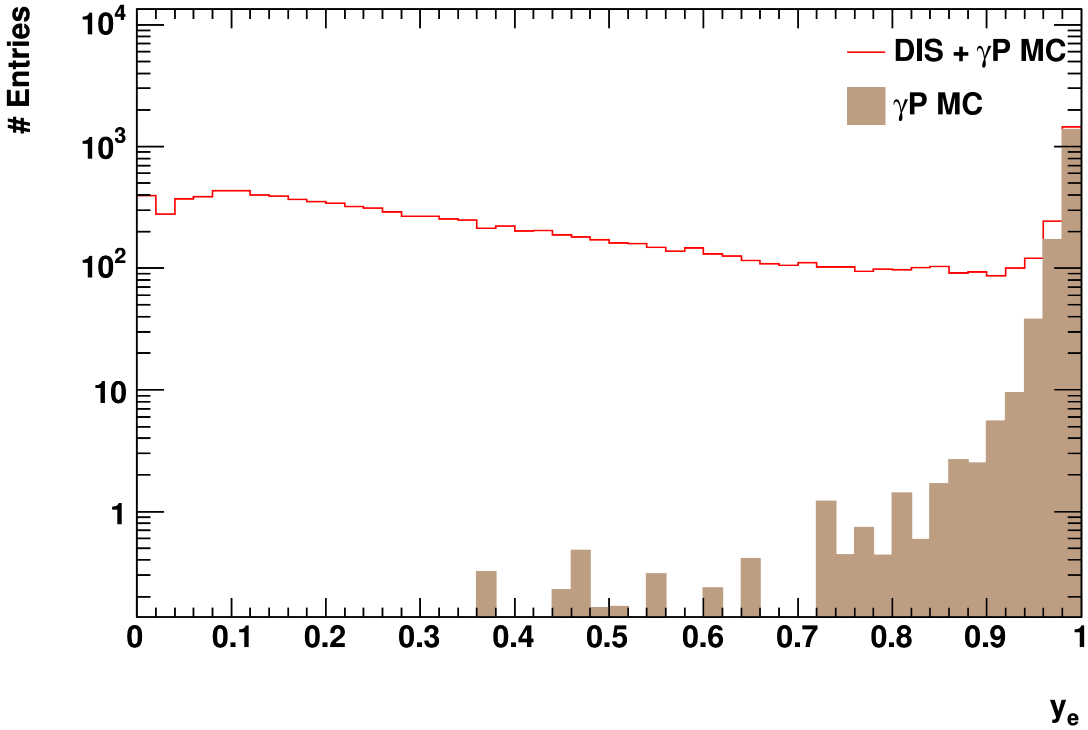

Figure 8.5: The y_e distribution in Monte Carlo. The background contamination by photoproduction events is shown to rise with y and to exceed the signal prediction at the highest y. This distribution is for events with $Q_e^2 > 890$ GeV.

in chapter 5. The background contribution is subtracted bin by bin, following the cross-section measurement procedure described in section 9.4. The background contamination is overall $< 1\%$ and smaller than 5% in any $x - Q^2$ bin.

8.4 Final Selection

The event selection, applied to both the LH and RH datasets, is summarised below.

- Run Selection **§8.1**
- Polarisation Quality **§8.1.1**
- Triggered by subtrigger **s67** or **s77** **§8.2.1**
- Fiducial volume cuts: inefficient trigger regions removed **§8.2.2**
- Scattered electron in LAr: isolated electron ID'd by electron finder **§7.1**
- $E'_e > 11$ GeV ($Q^2_e > 890$ GeV^2 $||$ $\mathrm{y_e} < 0.63$) **§8.2.2** and **§9.1**
- Remove z-cracks: $z_{LAr} < -190$ cm, $15 < z_{LAr} < 25$ cm **§7.1.1** and **§6.1**
- Remove ϕ cracks: $-2^\circ < \phi_{wheel} < 2^\circ$ **§7.1.1**
- $Q^2_e > 100$ GeV^2
- "Longitudinal energy balance", $E - P_z > 35$ GeV **§8.3.2**
- $ye < 0.9$ **§8.3.2**
- Validation by DTRA or DTNV track (for $\theta_e > 30^\circ$) **§7.3**
- Central Vertex with 33.8 cm $< \mathrm{z_{vtx}} <$ 37.2 cm **§7.2**
- CJC T0 timing **§8.3.1**
- Topological background finders **§8.3.1**
- Anti-Compton/l-pair cuts **§8.3.2**

The control of the high Q^2 NC DIS event sample is exhibited by the following distributions. The energy spectrum of the scattered electron is shown in figure 8.6 and demonstrates the good understanding of the electromagnetic energy calibration, described in section 6.1; control is particularly good above the kinematic peak (at $E'_e \simeq E_e$) corresponding to higher values of Q^2. The energy distribution for the events at very high Q^2, > 5000 GeV^2, is shown in figure 8.6(b) and is well described by the Monte Carlo. The dramatic reduction in statistics in the higher Q^2 sample is due to the $^1/_{Q^4}$ dependence of the cross section.

The contribution by ep background, dominated by photoproduction, is illustrated in figure 8.7(a). The contamination by mis-identified electrons with low energy at high polar angles, θ_e, can be clearly seen on the logarithmic scale. Figure 8.7(a) and 8.7(b) show the polar and azimuthal angles of the scattered electron, respectively. The structure in ϕ_e arises from regions of the detector removed from the sample due to energy leakage in cracks or

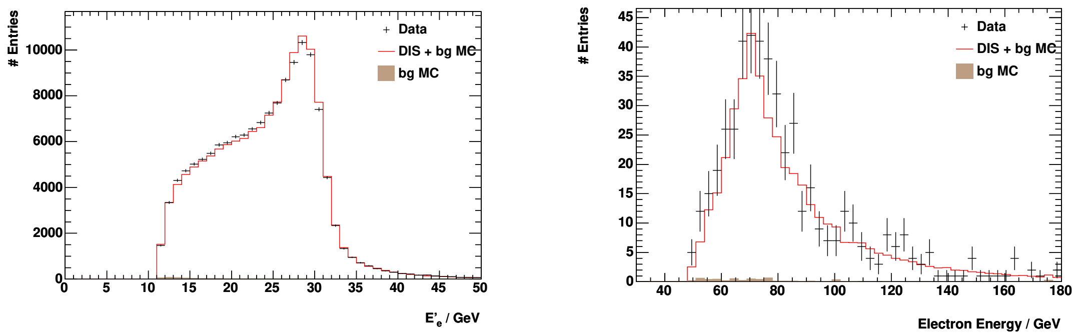

(a) (b)

Figure 8.6: Distribution of the reconstructed scattered electron energy for (a) $Q^2 > 100$ GeV^2 and (b) $Q^2 > 5000$ GeV^2.

trigger inefficiencies (see sections 7.1.1 and 8.2.2, respectively). The z impact position of the scattered electron in the calorimeter is displayed in figure 8.8 and is well modelled in the MC. The z crack at $15 < z_{LAr} < 25$ cm can be distinctly seen, as can the forward edge of the BBE at $z_{LAr} = -152.5$ cm. The BBE has different structure in the $r - \phi$ plane to the central barrel wheels. Thus it is not always possible to make an unambiguous assignment of the electron position (further details can be found in section 7.4.1.)

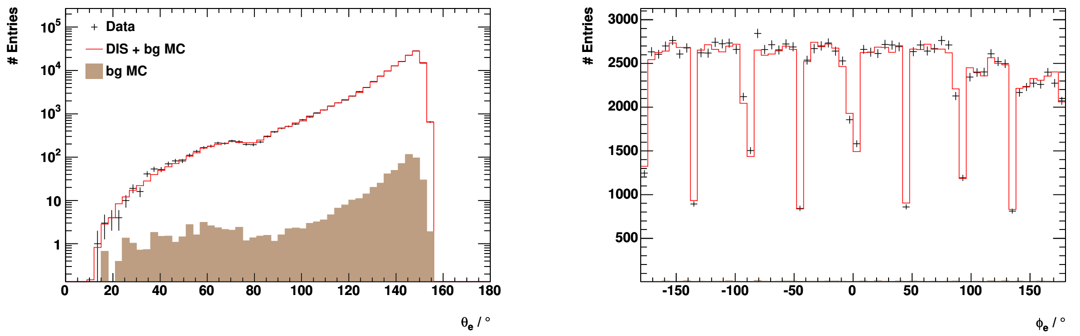

(a) (b)

Figure 8.7: The distribution of the polar, (a) and azimuthal, (b), angles of the scattered electron.

The hadronic energy calibration is described in section 6.2.3. The control of the hadronic final state is demonstrated in figure 8.9. Both the $p_{T,h}/p_{T,e}$ distribution and the $E - p_z$ distribution are well described by the Monte Carlo. In particular, the $p_{T,h}/p_{T,e}$ distribution is well simulated even at low values, where the hadronic final state is not well contained by the detector.

The $e\Sigma$ method is used to reconstruct the kinematic variables in this analysis, since it

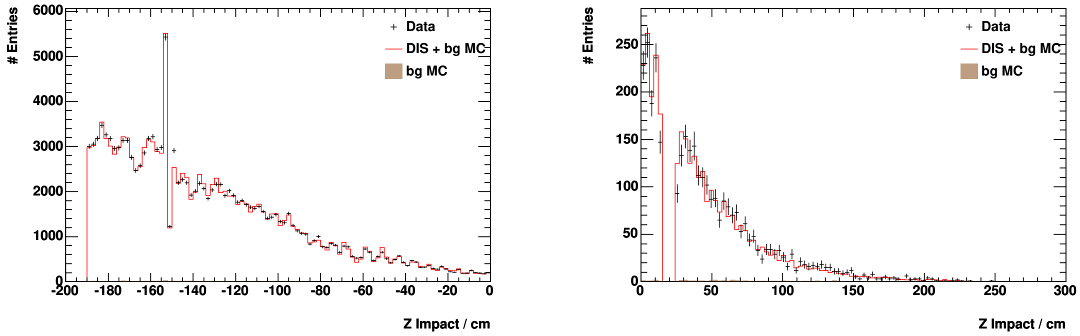

(a) (b)

Figure 8.8: The z impact position of the scattered electron in the LAr calorimeter. The distribution is shown in the range (a) $-200 < z_{LAr} < 0$ cm, and (b) $0 < z_{LAr} < 300$ cm.

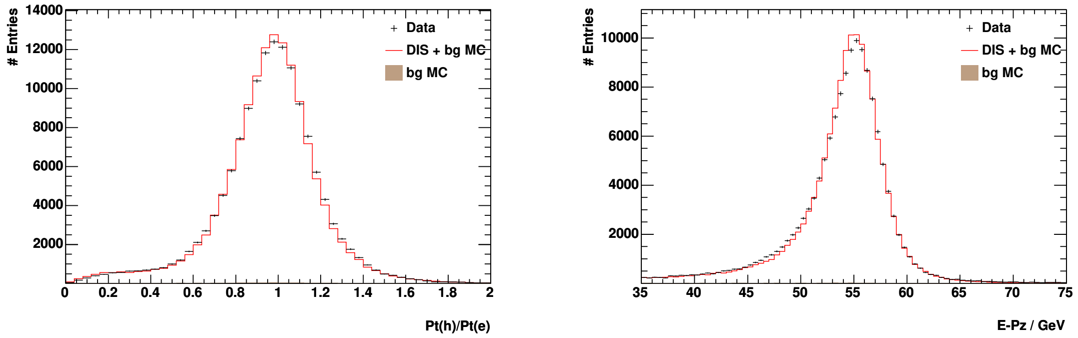

(a) (b)

Figure 8.9: (a) Distribution of transverse momentum balance, $p_{T,h}/p_{T,e}$, for the complete NC sample. (b) Distribution of "longitudinal momentum balance", $E - p_z$, for the complete sample.

gives the best resolution at both high and low y. The kinematic variables $Q^2_{e\Sigma} = Q^2_e$, $x_{e\Sigma} = x_\Sigma$ and $y_{e\Sigma} = \frac{Q^2_e}{x_\Sigma s}$, as defined in equation 4.7, are presented in figure 8.10.

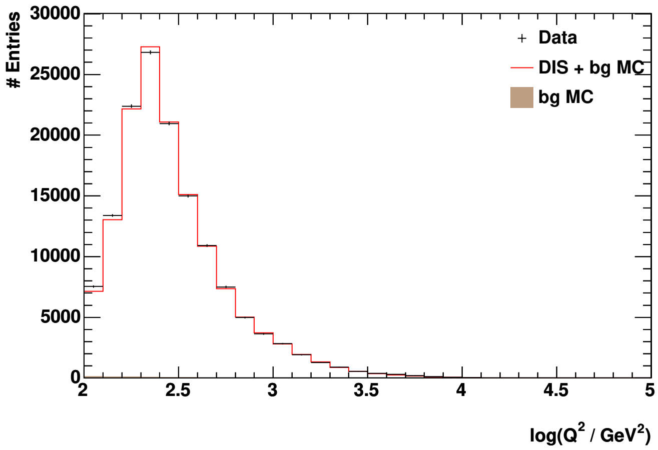

(a)

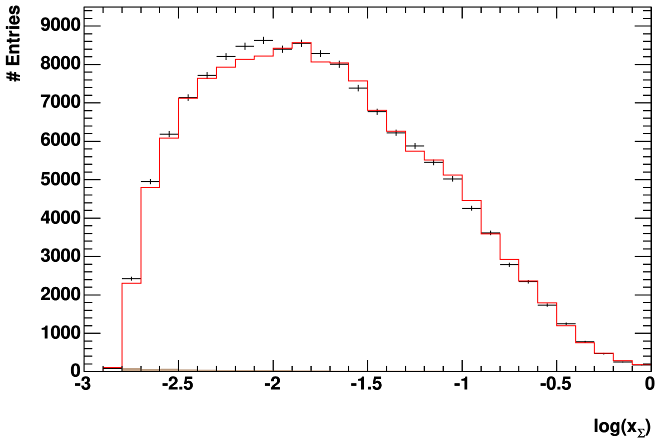

(b)

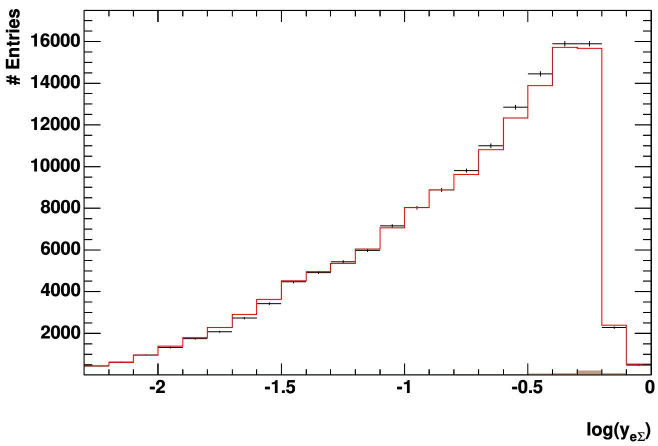

(c)

Figure 8.10: The reconstruction of the kinematic variables by the $e\Sigma$ method: (a) $\log{(Q_e^2)}$, (b) $\log{(x_\Sigma)}$, (c) $\log{(y_{e\Sigma})}$ in the complete inclusive NC sample.

Chapter 9

Cross Section Measurement Procedure

The procedure used for determination of the cross section is described in this chapter. First, the kinematic plane is divided in x and Q^2. The bin sizes are determined by the required statistical precision and resolution. The acceptance, purity and stability quantify the migrations from bin to bin. The procedure for extracting the cross section in each bin taking into account corrections for acceptance, radiative effects and bin size is described. Finally, the systematic uncertainties on the measurement are quoted and discussed.

9.1 Bin Selection

The cross section measurement in this analysis is performed in bins of x and Q^2. The binning used, shown in figure 9.1, was developed in NC analyses at HERA I [75]. There are ten bins per decade in Q^2, except at $Q^2 > 3000$ GeV^2 where the bin width is doubled due to limited statistics. There are five bins per decade in x, except at $Q^2 < 500$ GeV^2 and $x > 0.1$ where the bins are coarser due to the degraded x resolution at low y. The resolution is always better than the bin width, as can be seen in figure 9.1.

The values of the bin boundaries and bin centres can be found in [83].

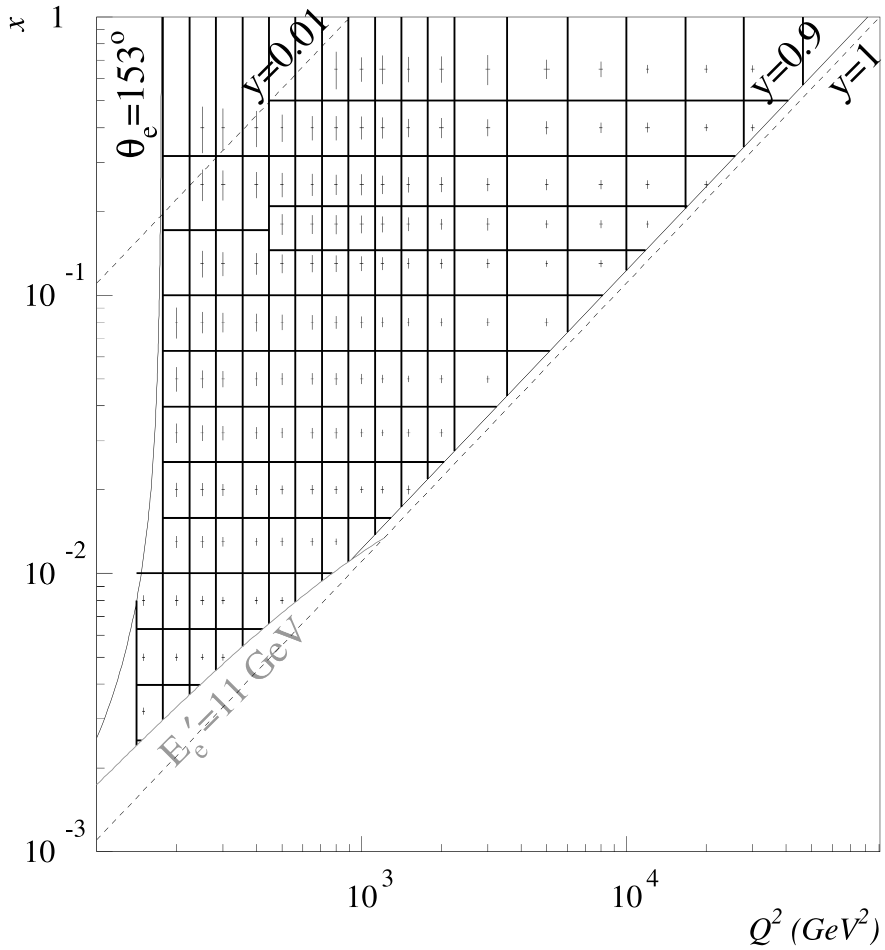

Figure 9.1: The bin boundaries in Q^2 and x for the NC measurement. Also shown are the upper $y = 0.9$ cut and the lines of constant $\theta = 153°$ and $E'_e = 11$ GeV, which define the measured phase space. The lines of constant $y = 0.01$ and $y = 1$ are shown for reference. The length of the horizontal and vertical cross bar indicates the Q^2 and x resolution, respectively. The electron energy cut, $E'_e > 11$ GeV (chosen to ensure optimal trigger efficiencies in this analysis, see section 8.2.2), corresponds to a cut $Q^2_e > 890$ GeV^2 $\;||\;$ $\mathrm{y_e} < 0.63$ in the kinematic plane.

9.2 Acceptance, Purity and Stability

A bin must satisfy certain quality criteria to be used in this measurement. The Acceptance, $\mathcal{A}$, Purity, $\mathcal{P}$, and Stability, $\mathcal{S}$, are calculated using the MC and are defined as:

$$\mathcal{A}_i = \frac{N_i^{rec}}{N_i^{gen}} \tag{9.1}$$

$$\mathcal{P}_i = \frac{N_i^{gen,rec}}{N_i^{rec}} \tag{9.2}$$

$$\mathcal{S}_i = \frac{N_i^{gen,rec}}{N_i^{gen,sel}} \quad , \tag{9.3}$$

where

- N_i^{gen} is the number of events generated in bin i;
- $N_i^{gen,rec}$ is the number of events generated and reconstructed in the bin i;
- N_i^{rec} is the total number of events reconstructed in bin i;
- $N^{gen,sel}$ is the number of events generated in bin i that survive the event selection.

The acceptance automatically accounts for the selection efficiency of the measurement. The acceptance, purity and stability in each $x-Q^2$ bin are shown in figure 9.2. The cross section measurement is performed only for bins in which the acceptance exceeds 20% and the purity and stability are larger than 30%.

9.3 Radiative Corrections

Radiative corrections in DIS arise from the exchange or emission of additional bosons, and from the self-energies of the particles involved. The effect of real photon emissions, either from initial state or final state leptons, is dependent on the acceptance of the detector and the experimental method. It is convenient to separate the radiative corrections into two contributions: those from electromagnetic processes and those involving weak ones,

$$1 + \delta^{RC} = (1 + \delta^{QED})(1 + \delta^{weak}) \quad . \tag{9.4}$$

The δ^{QED} term depends on the detector acceptance while the δ^{weak} term is independent of the experimental procedure. The allocation of radiative corrections to each term is to some degree arbitrary. The exact details on the separation of radiative corrections can be found in [89].

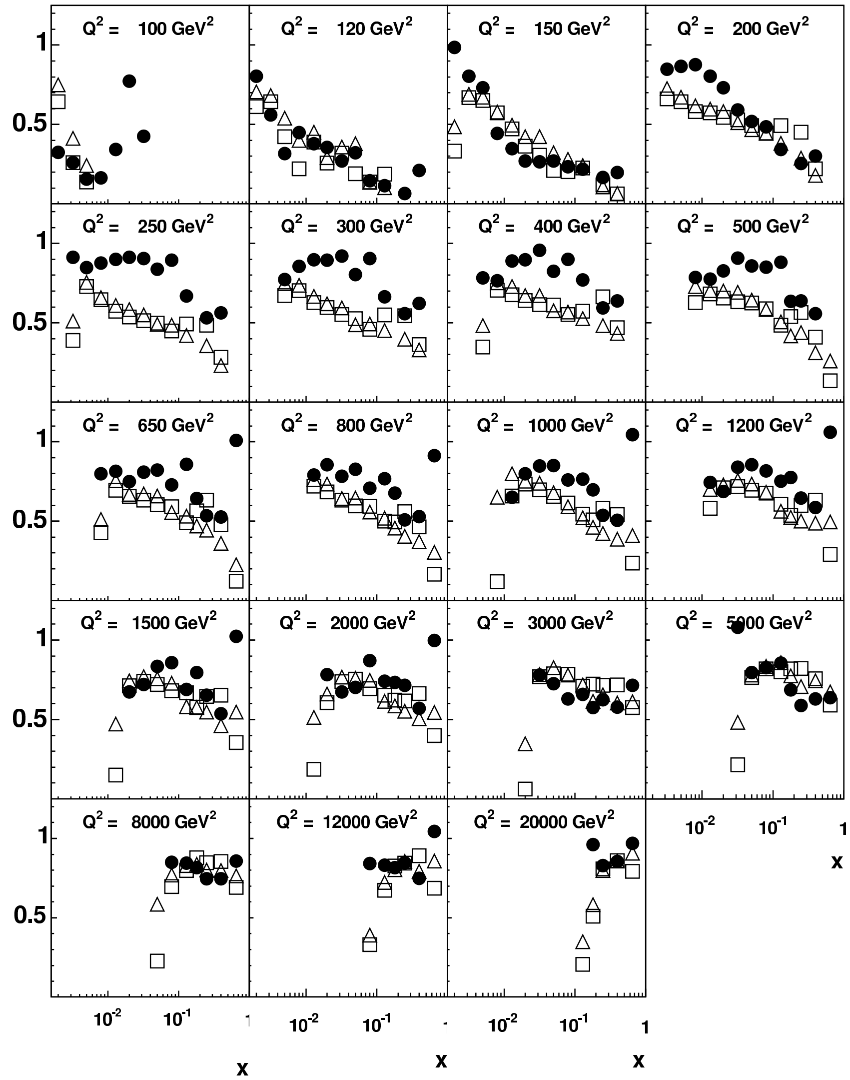

Figure 9.2: Acceptance (full circles), Purity (open squares) and Stability (open triangles) for each bin in the NC measurement.

In order to compare with analytically calculated predictions of the Standard Model cross section, only acceptance-dependent corrections need to be applied to the measured cross section. The purely weak correction, δ^{weak}, arises primarily from the self-energies of the particles involved. It must be applied when extracting structure functions from the cross section. A discussion of the treatment of radiative corrections in the NC measurement can be found in [75].

9.4 Cross Section Extraction

The cross section measured in a single bin in x and Q^2 can be extracted using

$$\frac{\mathrm{d}^2\sigma}{\mathrm{d}x\mathrm{d}Q^2} = \frac{N^{data} - N^{bg}}{\mathcal{L} \cdot \mathcal{A}} . \delta^{bc} . \frac{1}{1 + \delta^{QED}} \tag{9.5}$$

where

- N^{data} is the number of selected events in the bin;
- N^{bg} is the number of background events estimated by MC;
- $\mathcal{L}$ is the total integrated luminosity (see section 3.6);
- $\mathcal{A}$ is the detector acceptance, defined in equation 9.1, determined from a MC which includes radiative effects;
- the radiative correction factor,

  $$\delta^{QED} = \frac{\sigma^{theo}}{\sigma^{nonrad}} - 1, \tag{9.6}$$

  is estimated by the DJANGO MC. Here σ^{theo} is the cross section obtained using a MC simulation which includes radiative effects and σ^{nonrad} is the prediction without;
- δ^{bc} is the correction from the cross section in a bin of finite size, ($\Delta x = x_{max} - x_{min}, \Delta Q^2 = Q^2_{max} - Q^2_{min}$) to the bin centre at (x_c, Q^2_c):

  $$\delta^{bc} = \frac{\frac{\mathrm{d}^2\sigma}{\mathrm{d}x\mathrm{d}Q^2}\big|_{x_c,Q^2_c}}{\int_{x_{min}}^{x_{max}} \int_{Q^2_{min}}^{Q^2_{max}} \frac{\mathrm{d}^2\sigma}{\mathrm{d}x\mathrm{d}Q^2} \mathrm{d}x\mathrm{d}Q^2} = \frac{\sigma^{theo} \cdot \mathcal{L}_{\mathcal{MC}}}{N^{gen}}, \tag{9.7}$$

  where $\mathcal{L}_{\mathcal{MC}}$ is the integrated luminosity of the NC Monte Carlo.

Since the acceptance, radiative and bin-centre corrections are all estimated using the DJANGO Monte Carlo, equation 9.5 can be simplified using equations 9.1, 9.6 and 9.7 to:

$$\frac{\mathrm{d}^2\sigma}{\mathrm{d}x\mathrm{d}Q^2} = \frac{(N^{data} - N^{bg})}{N^{MC}} \frac{\mathrm{d}^2\sigma^{nonrad}}{\mathrm{d}x\mathrm{d}Q^2} \tag{9.8}$$

where N^{MC} is the MC prediction of the number of events reconstructed in the bin for the data luminosity, $N^{MC} = N^{rec}\frac{L}{L_{MC}}$.

The non-radiative cross section is calculated, σ^{nonrad} using the H1 2000 PDF fit [3] to HERA I data.

9.4.1 Reduced NC Cross Section

For the subsequent presentation of the double differential cross section measurement, it is convenient to define the "reduced NC cross section":

$$\tilde{\sigma}^{+}_{NC} = \frac{xQ^4}{2\pi\alpha^2}\frac{1}{Y_+}\frac{\mathrm{d}^2\sigma}{\mathrm{d}x\mathrm{d}Q^2} = \frac{1}{Y_+}\phi^{+}_{NC}(1+\delta^{weak}), \tag{9.9}$$

which is closely related to the structure function terms (see equations 2.6 and 2.7). The definition of the reduced NC cross section does not require the assumption of any electroweak parameters apart from the precisely known fine structure constant, α.

9.4.2 Single Differential Cross Sections

The single differential cross sections in x or Q^2 are defined as

$$\frac{\mathrm{d}\sigma}{\mathrm{d}x} = \int_{Q^2_{min}}^{Q^2_{max}} \frac{\mathrm{d}^2\sigma}{\mathrm{d}x\mathrm{d}Q^2}\mathrm{d}Q^2 \qquad \text{and} \qquad \frac{\mathrm{d}\sigma}{\mathrm{d}Q^2} = \int_{x_{min}}^{x_{max}} \frac{\mathrm{d}^2\sigma}{\mathrm{d}x\mathrm{d}Q^2}\mathrm{d}x. \tag{9.10}$$

They can be measured using equation 9.8, suitably adapted. The limits in x and Q^2 are chosen to be the highest and lowest bin edges in x and Q^2 from the double differential measurement, respectively.

9.5 Systematic uncertainties

The systematic uncertainties on the measurement are listed below, and the resulting typical relative error on the cross section is given where appropriate. Further detail on the studies related to each source of systematic uncertainty can be found in the noted sections. The systematic errors are assumed to be symmetric following the analysis of HERA I data [3].

Systematic uncertainties may be categorised as correlated from bin to bin or uncorrelated. A discussion of the classification of systematic errors at HERA I can be found in [3,75,83].

- **Luminosity uncertainty** - §3.6
  There is a global uncertainty of 1.3% on the luminosity measurement.

- **The electron energy measurement** - §6.1
  The total uncertainty on the electron energy is 1% in the BBE, CB1 and CB2, 2% in the CB3 wheel and 3% in the forward wheels. This estimate includes a 0.5% correlated error attributed to the uncertainty in the calibration method [75]. The remainder is treated as uncorrelated, since it originates primarily from limited statistics in the calibration and from local effects in some calorimeter regions. The uncertainty on the cross section resulting from this source rises with x and Q^2, from $\lesssim 1\%$ at the lowest Q^2 to $\gtrsim 10\%$ at the highest Q^2.

- **The electron polar angle measurement** - §7.4.3
  The uncorrelated uncertainty on the electron polar angle, arising from the residual mis-alignment of the LAr calorimeter to the trackers, is 3 mrad. A further correlated uncertainty of 3 mrad is attributed to the z resolution of the central tracker. The resulting uncertainty on the cross section is typically $< 2\%$, but rises to $\gtrsim 4\%$ at high x.

- **The electron azimuthal angle measurement** - §7.4.3
  An uncertainty of 2 mrad is assigned to the measurement of the azimuthal angle of the electron. This has a small effect on the cross section, typically a few per mille, and enters through ϕ-crack cuts.

- **The uncertainty on the electron identification** - §7.1.1
  A 1% uncorrelated error is assigned on the electron finding efficiency.

- **The uncertainty on the vertex reconstruction efficiency** - §7.2.1
  An uncorrelated uncertainty of 0.5% (2%) is assigned on the central vertex reconstruction efficiency at high y_h (low y_h).

- **The uncertainty on the track-cluster linking efficiency** - §7.3
  An uncorrelated uncertainty of 2% is assigned on the efficiency of the validation of the scattered electron by a linked track.

- **The hadronic energy scale** - §6.2.3
  A 2% uncertainty is assigned to the hadronic energy scale. The uncertainty on the cross section is largest at high x, where it is typically $\simeq 5\%$.

- **The hadronic polar angle measurement** - §7.4.3
  A 4 mrad uncertainty is assigned to the polar angle measurement of the hadronic

final state. The resulting error on the cross section is small at low x but increases to $\approx 5-6\%$ at high x.

- **Noise subtraction in the LAr calorimeter** - §6.2.1
  A 10% uncertainty is assigned on the amount of noise identified in the LAr calorimeter. The effect is largest at high x, where it can reach $10-20\%$ of the cross section.

- **Background subtraction** - §6.1.1 and §8.3.2
  The correlated uncertainties on the subtracted backgrounds as estimated by MC are:

  - 30% for photoproduction;
  - 50% for QED Compton scattering and lepton-pair production.

  The resulting uncertainty is smaller than 1% in every $x-Q^2$ bin.

- **Trigger efficiency uncertainty** - §8.2.1
  A 0.5% uncorrelated error is assigned on the determined trigger efficiency.

- **Radiative Corrections**
  A 1% uncertainty is assigned to the estimation of QED radiative corrections by the signal MC. This is based on comparisons between the corrections predicted by the signal Monte Carlo, DJANGO, and those calculated by HECTOR and EPRC [90]. This error also includes a small contribution missing from DJANGO from the exchange of two or more photons between the lepton and the quark line.

The systematic errors are added in quadrature to the statistical error. The fractional errors are shown in figure 9.3 for each measured bin in x and Q^2. The systematic errors dominate for $Q^2 < 500$ GeV^2. The statistical errors dominate in all bins above $Q^2 = 1000$ GeV^2.

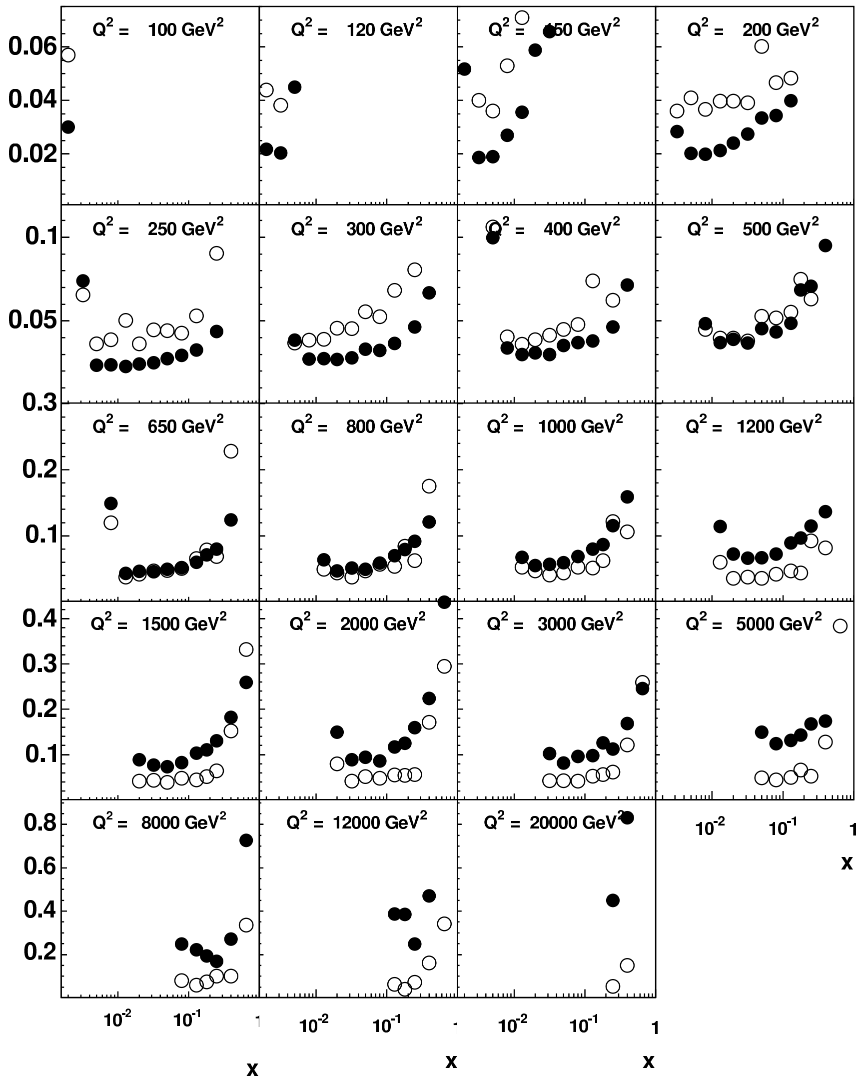

Figure 9.3: Fractional statistical (full circles) and systematic (open circles) errors on the NC measurement.

Chapter 10

Results

The results of this analysis are presented in this section. The cross sections for $e^+p \rightarrow e^+X$ are presented double differentially, in x and Q^2, and single differentially, in each of these variables. The measured cross sections are compared with the Standard Model predictions calculated, including polarisation effects according to equation 2.19, from the H1 2000 PDF fit (see section 2.3 and [3]).

All measurements are presented for both LH polarised positrons, with $P_e = -40.2 \pm 1.1\%$, and RH polarised positrons, $P_e = +33.6 \pm 0.7\%$. Finally, the polarisation asymmetry at very high Q^2 is discussed.

10.1 The Double Differential Cross Section $\mathrm{d}^2\sigma/\mathrm{d}x\mathrm{d}Q^2$

The double differential NC reduced cross section, $\tilde{\sigma}_{NC}$ (defined in equation 9.9), is shown in figure 10.1 for LH polarised positrons and 10.2 for RH polarised positrons. The LH measurement covers the range of 100 GeV^2 $\leq$ Q^2 $\leq$ 12000 GeV^2 and $0.002 < x < 0.65$, while the RH measurement covers the range of 100 GeV^2 $\leq$ Q^2 $\leq$ 20000 GeV^2 and $0.002 < x < 0.65$. The measured data are presented as a function of x in bins of Q^2. The data with both helicities exhibit similar features and are well described by the predictions of the H1 2000 PDF fit.

The reduced cross section exhibits a strong rise with decreasing x. This behaviour can be interpreted as originating from the rise of the sea quark distribution at low x, to which the proton structure function $\tilde{F}_2$ is sensitive (see equation 2.16). This rising sea quark

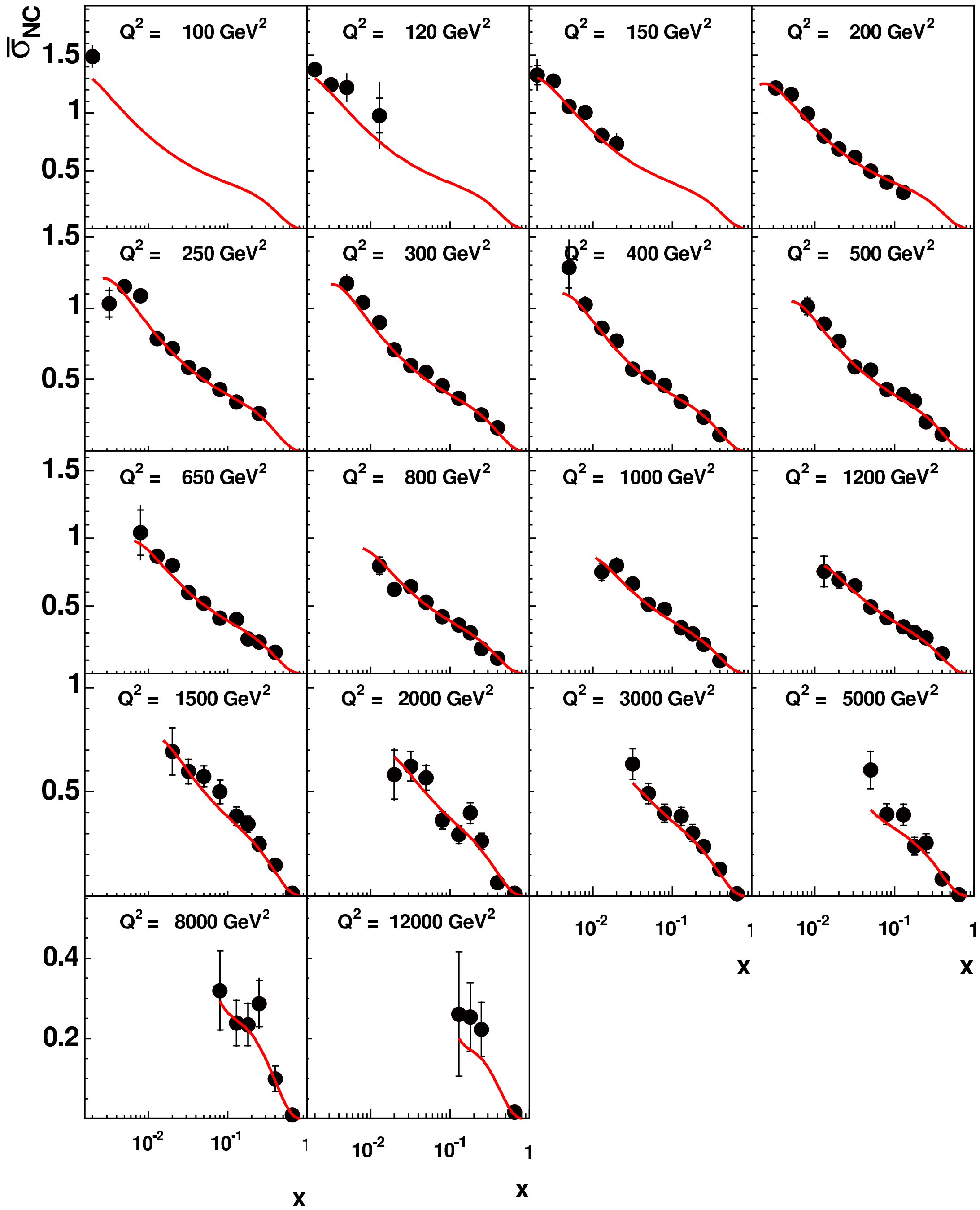

Figure 10.1: NC reduced cross section, $\tilde{\sigma}_{NC}$ for the LH e^+p 2003-04 data taken with mean $P_e = -40.2 \pm 1.1\%$ at $\sqrt{s} = 319$ GeV. The data (full points) are compared to the predictions from the H1 2000 PDF fit (solid curve). The inner and outer error bars represent the statistical and total errors, respectively. The 1.3% luminosity error is not included in the error bars.

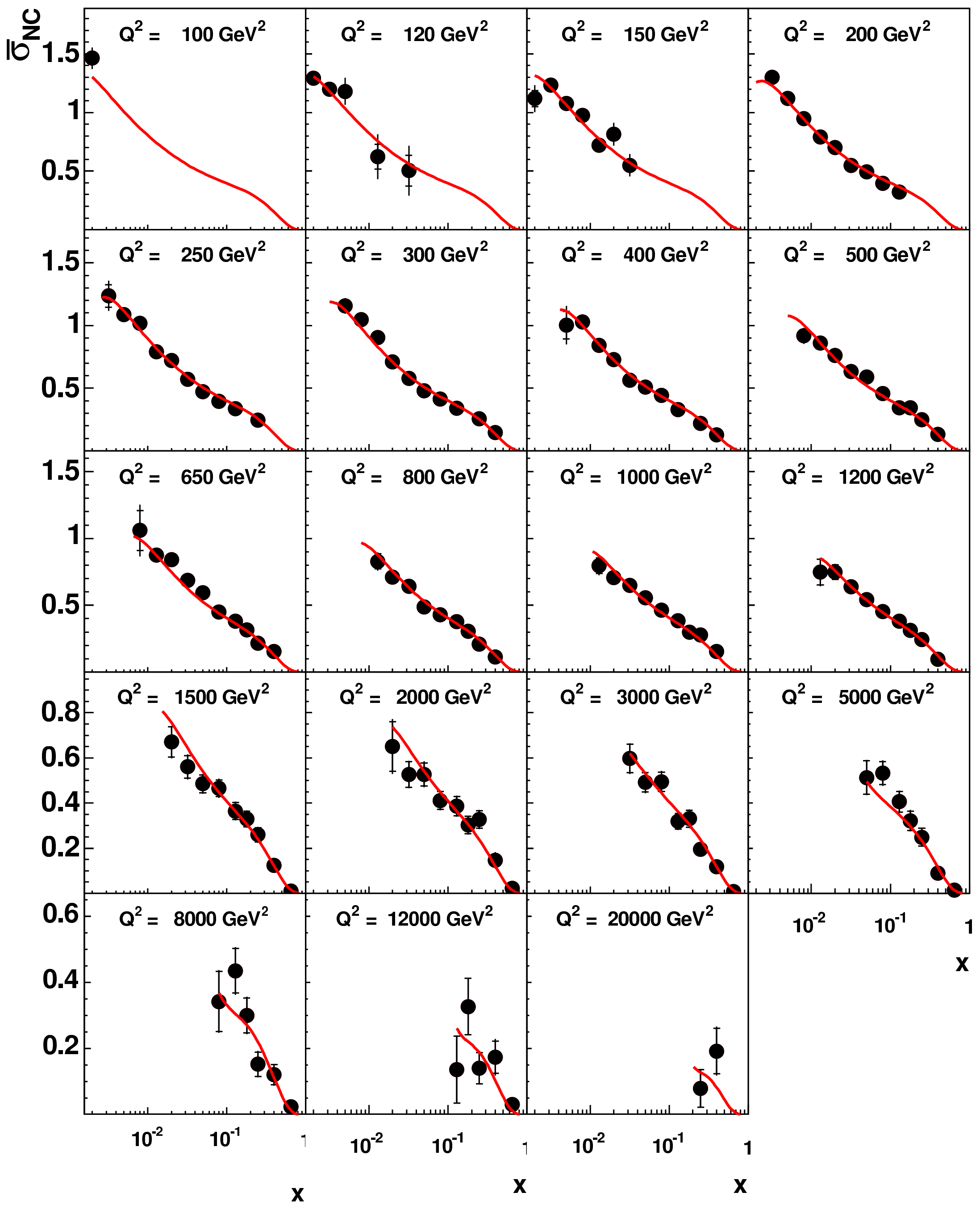

Figure 10.2: NC reduced cross section, $\tilde{\sigma}_{NC}$ for the RH e^+p 2003-04 data taken with mean $P_e = +33.6 \pm 0.7\%$ at $\sqrt{s} = 319$ GeV. The data (full points) are compared to the predictions from the H1 2000 PDF fit (solid curve). The inner and outer error bars represent the statistical and total errors, respectively. The 1.3% luminosity error is not included in the error bars.

distribution is in turn driven by the dominant gluon density at low x [3]. The rise with decreasing x becomes stronger as Q^2 increases.

10.2 The Single Differential NC Cross Section $d\sigma/dx$

The single differential e^+p cross sections $d\sigma/dx$ (defined in equation 9.10) are shown in figure 10.3 for both LH and RH data. The cross sections are measured for both $Q^2 > 1000$ GeV^2 and $y < 0.9$, and for $Q^2 > 10000$ GeV^2 and $y < 0.9$. Performing the measurement with these Q^2 cuts enhances the sensitivity to weak effects and hence to polarisation effects. All cross sections rise towards low x except at the lowest x values, where the cross section falls due to the kinematic cut at $y = 0.9$. Above $Q^2 > 10000$ GeV^2, contributions from Z^0 exchange and γZ^0 interference play a role and the SM expectation differs noticeably between LH and RH helicity states. However, the statistical errors on the measurement, which are typically 25% in the RH dataset and exceed 30% in the LH dataset, require that more data must be collected before the measurement can challenge the prediction.

10.3 The Single Differential NC Cross Section $d\sigma/dQ^2$

The single differential cross section $d\sigma/dQ^2$ for $y < 0.9$ is shown in figure 10.4 for both LH and RH data. The cross sections fall dramatically over the measured Q^2 range due to the dominating photon exchange cross section with the $1/Q^4$ dependence in the propagator term (see equation 2.18). The LH NC cross section is measured in the range 200 GeV^2 $\leq$ Q^2 $\leq$ 12000 GeV^2, while the RH NC cross section is measured in the range 200 GeV^2 $\leq$ Q^2 $\leq$ 20000 GeV^2. Both are well described by the predictions of the H1 2000 PDF fit.

The measured cross sections have a total error of $3-4\%$ in the lower Q^2 bins, primarily arising from the systematic error. The contribution from the statistical errors increases with increasing Q^2 and dominates the total error above $Q^2 \simeq 1000$ GeV^2.

Figure 10.5 shows the ratios of the $d\sigma/dQ^2$ measurements to the Standard Model expectation for the cross section with unpolarised positrons. The prediction including the polarisation-dependent component of the cross section is also shown for each helicity. The NC cross section is predicted to shift by $\approx 10\%$ at $Q^2 \simeq 10000$ GeV^2. The total errors on the measurement in this region, primarily arising from the statistical error, are

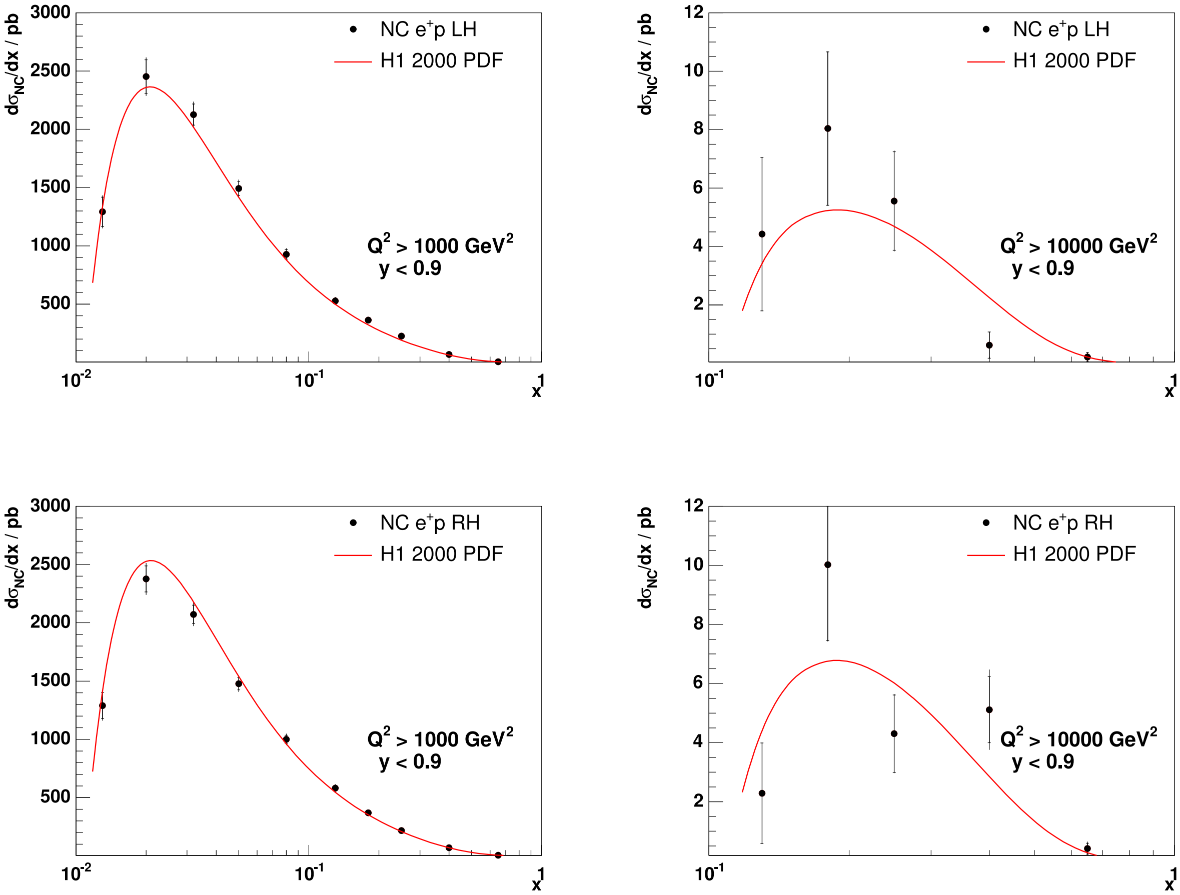

Figure 10.3: The x dependence of the NC cross section $\mathrm{d}\sigma/\mathrm{d}x$ for $y < 0.9$ and $Q^2 > 1000$ GeV^2 (left) and $Q^2 > 10000$ GeV^2 (right). The cross sections are shown for LH positrons (top) and for RH positrons (bottom). The data (full points) are compared to the predictions from the H1 2000 PDF fit (solid curve). The inner and outer error bars represent the statistical and total errors, respectively. The 1.3% luminosity error is not included in the error bars.

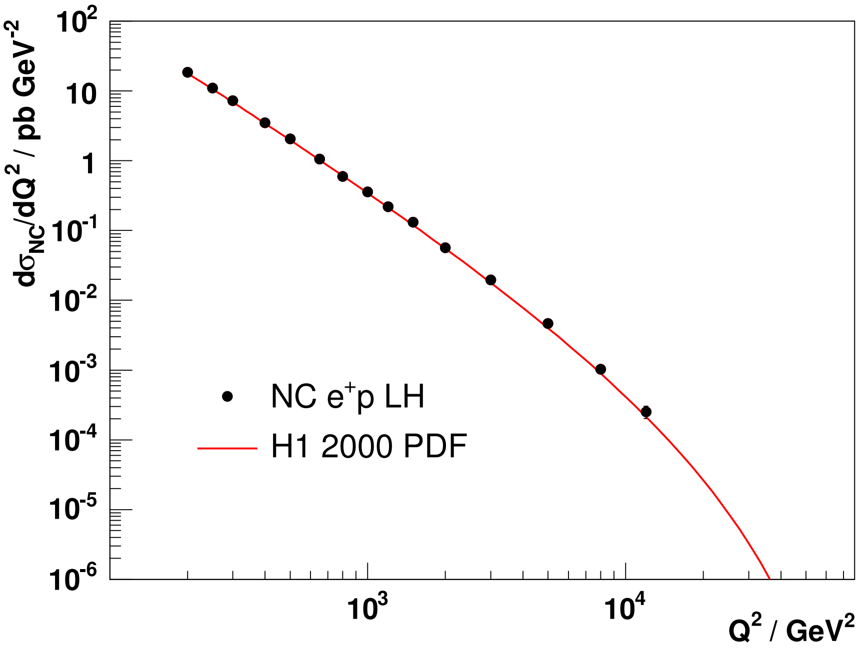

(a)

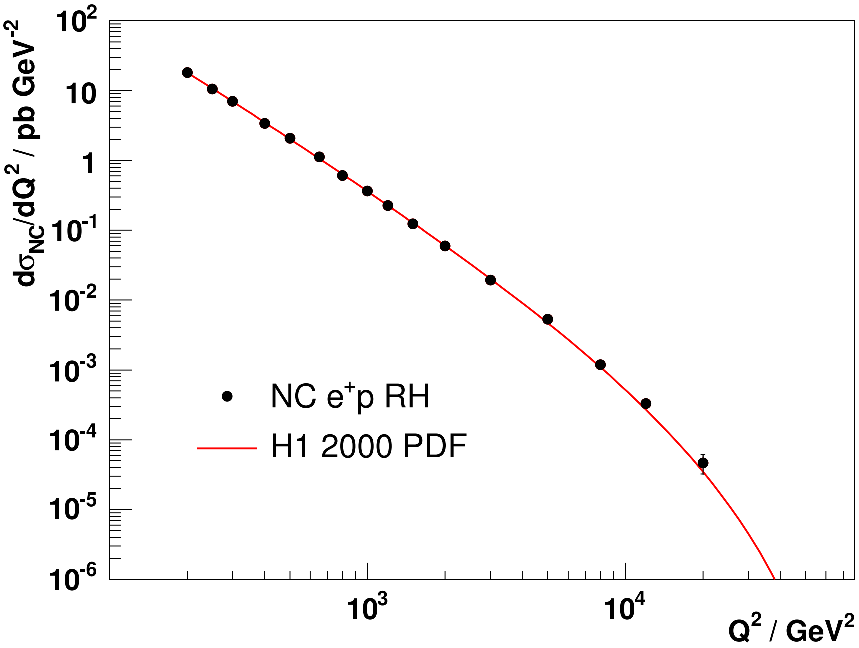

(b)

Figure 10.4: The Q^2 dependence of the LH (a) and RH (b) cross sections, $\mathrm{d}\sigma/\mathrm{d}Q^2$ for $y < 0.9$. The data (full points) are compared to the predictions from the H1 2000 PDF fit (solid curve). The inner and outer error bars represent the statistical and total errors, respectively. The 1.3% luminosity error is not included in the error bars.

$10-20\%$. Although the RH data lie higher than the LH data in this region, the statistical uncertainties so far preclude firm conclusions on the polarisation dependence.

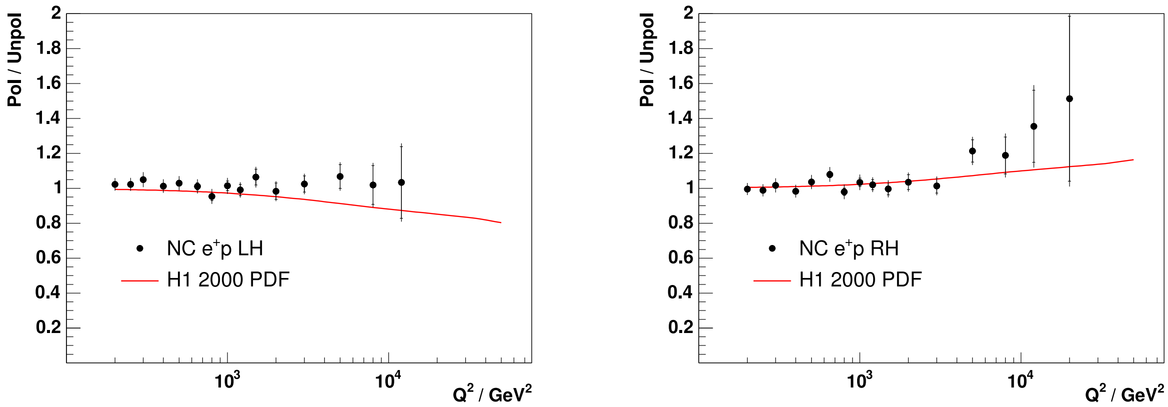

(a) (b)

Figure 10.5: The ratio of the 2003-04 LH (a) and RH (b) $\mathrm{d}\sigma/\mathrm{d}Q^2$ data to the Standard Model expectation for unpolarised positrons. The ratio of the predicted cross section to the unpolarised expectation for each helicity is also shown, demonstrating the rise of the polarisation-dependent part of the cross section with Q^2. The inner and outer error bars represent the statistical and total errors, respectively. The 1.3% luminosity error is not considered in the error bars.

10.3.1 The Polarisation Asymmetry

The polarisation asymmetry between the single differential cross sections, $A(\mathrm{d}\sigma/\mathrm{d}Q^2)$ defined by analogy with equation 2.19, is measured at very high Q^2, where statistical errors dominate.

$$A(\mathrm{d}\sigma/\mathrm{d}Q^2) = \frac{\mathrm{d}\sigma^{RH}/\mathrm{d}Q^2 - \mathrm{d}\sigma^{LH}/\mathrm{d}Q^2}{\mathrm{d}\sigma^{RH}/\mathrm{d}Q^2 + \mathrm{d}\sigma^{LH}/\mathrm{d}Q^2} \tag{10.1}$$

The polarisation asymmetry is measured in two bins at the 1σ level and in agreement with the prediction, tentatively confirming the Standard Model predictions of the polarisation dependence of the NC cross section at high Q^2. The asymmetry measurement is presented in table 10.1.

	$A(\mathrm{d}\sigma/\mathrm{d}Q^2)$	Prediction
$Q^2 = 8000$ GeV^2	$0.077 \pm 0.070 \quad (stat.)$	0.10
$Q^2 = 12000$ GeV^2	$0.134 \pm 0.123 \quad (stat.)$	0.117

Table 10.1: The polarisation asymmetry, $A(\mathrm{d}\sigma/\mathrm{d}Q^2)$, is presented in two Q^2 bins along with the accompanying statistical error and compared to the Standard Model prediction calculated from the H1 2000 PDF fit.

Chapter 11

Summary and Future Prospects

11.1 Summary of the Analysis

In this thesis a measurement of the neutral current cross sections in e^+p scattering at a centre of mass energy of $\sqrt{s} = 319$ GeV with polarised positrons has been presented. The measurements were performed at high Q^2 using data recorded by the H1 Detector at HERA in 2003 and 2004. This is the first analysis of NC DIS using data taken at the upgraded H1 detector at HERA II. In total 20.72 ± 0.27 pb^{-1} of left-handed (LH) polarised e^+p data has been taken with a mean polarisation of $P_e = -40.2 \pm 1.1\%$ and 26.91 ± 0.35 pb^{-1} of right-handed (RH) polarised e^+p data with a mean polarisation of $33.6 \pm 0.7\%$. The results are briefly summarised as follows:

- The NC cross sections for LH e^+p (RH e^+p) are measured in the range 100 GeV^2 $\leq$ Q^2 $\leq$ 12000 GeV^2 (100 GeV^2 $\leq$ Q^2 $\leq$ 20000 GeV^2) and $0.002 < x < 0.65$. The precision of the double differential cross section is at the level of a few per cent at low Q^2, where the systematic error dominates, but is limited by the statistical precision of the data at very high Q^2;

- The single differential cross section $\mathrm{d}\sigma/\mathrm{d}x$ has been measured for $y < 0.9$ and $Q^2 > 1000$ GeV^2 and $Q^2 > 10000$ GeV^2 for both helicities. The $Q^2 > 10000$ GeV^2 measurement, where the predicted cross section differs for the LH and RH data due to electroweak effects, is found to be consistent with the prediction, but statistically limited;

- The single differential cross section $\mathrm{d}\sigma/\mathrm{d}Q^2$ has been measured for $y < 0.9$ in the range $200 \leq Q^2 \leq 12000$ GeV^2 ($200 \leq Q^2 \leq 20000$ GeV^2) for LH e^+p (RH e^+p). The predicted cross sections diverge from the cross section for unpolarised e^+p DIS by approximately 10% at very high $Q^2 \simeq 10000$ GeV^2. The asymmetry between the LH and RH cross sections has been measured (at the 1σ level, due to the large statistical errors) providing tentative confirmation of the polarisation dependence of the NC cross section.

11.2 Future Prospects for the Analysis

It is clear that the main requirement for an improved measurement is increased statistics. In addition, there are several areas where the systematic errors on the measurement could be improved in future.

- Further development of the alignment of the LAr calorimeter to the central tracking system together with the study of the z measurement in the Central Tracking Detector would allow a significant reduction of the systematic uncertainty on the polar angle measurement. This may be coupled to a better measurement of central vertices and a better modelling of the vertex finding efficiency by the simulation.
- Significant progress has been made in the understanding of the forward tracking detector at HERA II. The inclusion of forward vertices would improve the efficiency at low y and the use of forward tracks may improve the scattered electron measurement at the highest Q^2.

11.3 Future Prospects for NC Cross Sections

Since the completion of the first period of e^+p data taking at HERA II, H1 has been recording data from e^-p collisions. H1 has accumulated 30 pb^{-1} of RH e^-p data with a mean polarisation of 37% and 70 pb^{-1} of LH e^-p data with a mean polarisation of -27%. This exceeds the unpolarised e^-p dataset of 16.4 pb^{-1} collected at HERA I. The cross sections for electron scattering can be compared with the cross sections for positron scattering to determine the structure function $x\tilde{F}_3$, which provides information on the valence quark density in the proton. The NC DIS cross section for polarised electrons is enhanced by up to a factor of three compared to the cross section for polarised positrons at very high Q^2 (as illustrated in figure 2.2).

An additional $200 - 300$ pb^{-1} is expected to be delivered to H1 by the end of HERA II. It will be possible to combine the HERA I and HERA II datasets, and even to combine with ZEUS data, to maximise statistics and to improve the understanding of some of the systematic errors on the measurement. In particular higher statistics will allow the electron energy scale to be studied in greater detail in the forward region. The statistical errors will be driven down as the luminosity taken increases so that the measurement will become systematically limited at higher values of Q^2, where interesting electroweak effects are strongest. Thus, continued efforts to control the sources of systematic uncertainties are necessary for this analysis. The neutral current cross sections measured with all four combinations of lepton charge and helicity can be exploited to precisely determine the structure function $F_2^{\gamma Z}$ and, hence, to constrain the u/d ratio in the proton at high x. Finally, the measured cross sections may be used to extract the axial and vector couplings of the light quarks, the u and the d, to the Z^0 boson (see equations 2.16 and 2.17). With a sizeable HERA dataset it may be possible to determine $\nu_{u,d}$ and $a_{u,d}$ with a precision that rivals the measurement of the heavy quark couplings from LEP [91].

Bibliography

[1] M. Gell-Mann, Phys. Lett. **8**, 214 (1964).

[2] R. Beyer, E. Elsen, S. Riess, F. Zetsche, and H. Spiesberger, Prepared for Workshop on Future Physics at HERA (Preceded by meetings 25-26 Sep 1995 and 7-9 Feb 1996 at DESY), Hamburg, Germany, 30-31 May 1996.

[3] H1 Collaboration, C. Adloff *et al.*, Eur. Phys. J. **C30**, 1 (2003), hep-ex/0304003.

[4] M. Klein, Prepared for 9th International Workshop on Deep Inelastic Scattering (DIS 2001), Bologna, Italy, 27 Apr - 1 May 2001.

[5] P. Newman, private communication.

[6] H1 Collaboration, A. Nikiforov, H1prelim-05-042.

[7] H1 Collaboration, S. Schmitt, H1prelim-04-141.

[8] ZEUS Collaboration, ZEUS-prel-05-017.

[9] ZEUS Collaboration, ZEUS-prel-04-030.

[10] Y. L. Dokshitzer, Sov. Phys. JETP **46**, 641 (1977).

[11] V. N. Gribov and L. N. Lipatov, Sov. J. Nucl. Phys. **15**, 438 (1972).

[12] V. N. Gribov and L. N. Lipatov, Sov. J. Nucl. Phys. **15**, 675 (1972).

[13] G. Altarelli and G. Parisi, Nucl. Phys. **B126**, 298 (1977).

[14] A. D. Martin, R. G. Roberts, W. J. Stirling, and R. S. Thorne, Eur. Phys. J. **C23**, 73 (2002), hep-ph/0110215.

[15] J. Pumplin *et al.*, JHEP **07**, 012 (2002), hep-ph/0201195.

[16] H1 Collaboration, H1 Internal Note H1-10/97-531.

[17] H1 Collaboration, available at https://www-h1.desy.de/idet/upgrade/.

[18] A. A. Sokolov and I. M. Ternov, Phys. Dokl. **8**, 1203 (1964).

[19] V. Andreev *et al.*, H1 Internal Note H1-02/99-565.

[20] H1 Background Working Group, V. Andreev *et al.*, H1 Internal Note H1-10/02-606.

[21] H1 Background Working Group, V. Andreev *et al.*, H1 Internal Note H1-01/03-607.

[22] H1 Collaboration, I. Abt *et al.*, Nucl. Instrum. Meth. **A386**, 310 (1997).

[23] H1 Collaboration, I. Abt *et al.*, Nucl. Instrum. Meth. **A386**, 348 (1997).

[24] D. Pitzl *et al.*, Nucl. Instrum. Meth. **A454**, 334 (2000), hep-ex/0002044.

[25] W. Eick *et al.*, Nucl. Instrum. Meth. **A386**, 81 (1997).

[26] W. Braunschweig *et al.*, H1 Internal Note H1-02/99-563.

[27] H1 Collaboration, DESY Proposal PRC 98/06.

[28] M. Cuje *et al.*, H1 Internal Note H1-01/98-535.

[29] M. Urban, *The new CIP2k z-Vertex Trigger for the H1 Experiment at HERA*, PhD thesis, Zurich, 2004.

[30] H. Beck, H1 Internal Note H1-05/96-479.

[31] H. Wellisch, J. Kubenka, H. Oberlack, and P. Schacht, H1 Internal Note H1-02/94-346.

[32] H1 Calorimeter Group, B. Andrieu *et al.*, Nucl. Instrum. Meth. **A336**, 460 (1993).

[33] H1 Calorimeter Group, B. Andrieu *et al.*, Nucl. Instrum. Meth. **A350**, 57 (1994).

[34] H1 Calorimeter Group, B. Andrieu *et al.*, Nucl. Instrum. Meth. **A336**, 499 (1993).

[35] H1 SPACAL Group, R. D. Appuhn *et al.*, Nucl. Instrum. Meth. **A386**, 397 (1997).

[36] D. Reyna, H1 Internal Note H1-11/98-555.

[37] H1 SPACAL Group, T. Nicholls *et al.*, Nucl. Instrum. Meth. **A374**, 149 (1996).

[38] A. Beglarian, J. Dainton, M. Fleischer, and C. Wissing, ToF Group note.

[39] H. Bethe and W. Heitler, Proc. Roy. Soc. Lond. **A146**, 83 (1934).

[40] V. Andreev *et al.*, H1 Internal Note H1-06/98-544.

[41] V. Andreev *et al.*, Nucl. Instrum. Meth. **A494**, 45 (2002).

[42] S. Levonian, The status of the H1 luminosity system, Talk given at the H1 Collaboration Meeting, La Roche-en-Ardenne, September 2005.

[43] J. Bracinik, at the H1 Trigger Meeting 20th Jan, 2003.

[44] T. Carli *et al.*, H1 Internal Note H1-07/95-445.

[45] J. C. Bizot *et al.*, H1 Internal Note H1-02/92-212.

[46] J. C. Bizot *et al.*, H1 Internal Note H1-01/97-508.

[47] J. H.Kohne *et al.*, H1 Internal Note H1-01/97-509.

[48] A. Baird *et al.*, IEEE Trans. Nucl. Sci. **48**, 1276 (2001), hep-ex/0104010.

[49] The H1 Collaboration, available at https://www-h1.desy.de/icas/imanuals/h1rec/h1rec9/h1rec.html.

[50] R. Brun and F. Rademakers, Nucl. Instrum. Meth. **A389**, 81 (1997), available at http://root.cern.ch.

[51] The H100 Group, available at https://www-h1.desy.de/icas/oop/current/oo/.

[52] P. Thompson, private communication.

[53] P. Laycock, *A Measurement of the Diffractive Reduced Cross-Section $\sigma_r^D(3)$ at High Q^2 with the H1 Detector at HERA*, PhD thesis, Liverpool, 2003.

[54] N. Werner, *Measurement of the Charged Current Cross Section in Positron-Proton Collisions at HERA*, PhD thesis, Zurich, 2004.

[55] E. Woehrling, *High Q^2 Neutral Current Interactions at H1 and an Extraction of xF_3*, PhD thesis, Birmingham, 2004.

[56] A. Blondel and F. Jacquet, in *Proc. of the "Study of an ep Facility for Europe."*, edited by U. Amaldi, volume DESY 79/48, p. 391, 1979.

[57] U. Bassler and G. Bernardi, Nucl. Instrum. Meth. **A426**, 583 (1999), hep-ex/9801017.

[58] U. Bassler and G. Bernardi, Nucl. Instrum. Meth. **A361**, 197 (1995), hep-ex/9412004.

[59] S. Bentvelsen *et al.*, Reconstruction of (x, Q^2) and extraction of structure functions in neutral current scattering at hera, in *Proc. of the Workshop "Physics at HERA"*, edited by W. Buchmuller and G. Ingelmann, volume 1, pp. 23–40, DESY, 1992.

[60] S. Youssef, F. James, and R. Cousins, Eur. Phys. J. **C15**, 202 (2000).

[61] R. Brun, F. Bruyant, M. Maire, A. C. McPherson, and P. Zanarini, CERN-DD/EE/84-1.

[62] G. A. Schuler and H. Spiesberger, In *Hamburg 1991, Proceedings, Physics at HERA, vol. 3* 1419-1432. (see HIGH ENERGY PHYSICS INDEX 30 (1992) No. 12988).

[63] A. Kwiatkowski, H. Spiesberger, and H. J. Mohring, Comp. Phys. Commun. **69**, 155 (1992).

[64] G. Ingelman, A. Edin, and J. Rathsman, Comput. Phys. Commun. **101**, 108 (1997), hep-ph/9605286.

[65] T. Sjostrand and M. Bengtsson, Comput. Phys. Commun. **43**, 367 (1987).

[66] B. Andersson, G. Gustafson, G. Ingelman, and T. Sjostrand, Phys. Rept. **97**, 31 (1983).

[67] A. D. Martin, W. J. Stirling, and R. G. Roberts, Talk given at Leipzig Workshop on Quantum Field Theory Theoretical Aspects of High Energy Physics, Bad Frankenhausen, Germany, 20-24 Sep 1993 and at Topical Meeting on QCD at HERA, Durham, Eng., Mar 22-26, 1993.

[68] T. Sjostrand, L. Lonnblad, and S. Mrenna, (2001), hep-ph/0108264.

[69] M. Gluck, E. Reya, and A. Vogt, Phys. Rev. **D46**, 1973 (1992).

[70] C. Berger and P. Kandel, Prepared for Workshop on Monte Carlo Generators for HERA Physics (Plenary Starting Meeting), Hamburg, Germany, 27-30 Apr 1998.

[71] V. Lenderman, *Measurement of the QED Compton Scattering Cross Section with the H1 Detector at HERA*, PhD thesis, Dortmund, 2001.

[72] J. A. M. Vermaseren, Nucl. Phys. **B229**, 347 (1983).

[73] S. P. Baranov, O. Duenger, H. Shooshtari, and J. A. M. Vermaseren, In *Hamburg 1991, Proceedings, Physics at HERA, vol. 3* 1478-1482. (see HIGH ENERGY PHYSICS INDEX 30 (1992) No. 12988).

[74] U. Baur, J. A. M. Vermaseren, and D. Zeppenfeld, Nucl. Phys. **B375**, 3 (1992).

[75] B. Heinemann, *Measurement of Charged Current and Neutral Current Cross Sections in Positron Proton Collisions at* $\sqrt{s} \approx 300\ GeV^2$, PhD thesis, Hamburg, 1999.

[76] U. Bassler and G. Bernardi, Z. Phys. **C76**, 223 (1997), hep-ex/9707024.

[77] M. Peez, B. Portheault, and E. Sauvan, H1 Internal Note H1-01/05-616.

[78] J. Cao and Z. Zhang, H1 Internal Note H1-12/99-580.

[79] S. D. Ellis and D. E. Soper, Phys. Rev. **D48**, 3160 (1993), hep-ph/9305266.

[80] P. Bruel, *Recherche d'interactions au-dela du Modele Standard a HERA*, PhD thesis, Orsay, 1998.

[81] A. Mehta, New Track Based Electron Finder, Talk given at the High Q^2 Analysis meeting, Hamburg, October 2003.

[82] A. Nikiforov, private communication.

[83] A. Dubak, *Measurement of the e+p Neutral Current DIS Cross Section and the F2, FL, xF3 Structure Functions in the H1 Experiment at HERA*, PhD thesis, Munich, 2003.

[84] B. Portheault, *Premiere mesure des sections efficaces de courant charge et neutre avec le faisceau de positrons polarise a HERA II et analyses QCD-electrofaibles*, PhD thesis, Orsay, 2005.

[85] N. Malden, private communication.

[86] A. Bunyatyan, DQ checks of ToF, Talk given at the Data Quality Meeting, Hamburg, February 2004.

[87] C. Veelken, H1 Internal Note H1-09/02-603.

[88] A. Mehta, private communication.

[89] G. Kramer and H. Spiesberger, In *Hamburg 1991, Proceedings, Physics at HERA, vol. 2* 789- 797. (see HIGH ENERGY PHYSICS INDEX 30 (1992) No. 12988).

[90] H. Spiesberger, Prepared for Workshop on Future Physics at HERA (Preceded by meetings 25-26 Sep 1995 and 7-9 Feb 1996 at DESY), Hamburg, Germany, 30-31 May 1996.

[91] R. J. Cashmore *et al.*, Prepared for Workshop on Future Physics at HERA, Hamburg, Germany, 30-31 May 1996.

Acknowledgements

As always, the difficulty is knowing where to start and where to end. This can not be and is not a comprehensive list of those who have contributed to my doctorate, this thesis or to any part of the last four years. Nor will I attempt to begin to credit the lecturers/tutors/project supervisors that somehow brought me through my undergraduate degree without destroying my love for physics.

In what has now become an H1 Brum tradition, I had a tag-team of supervisors through my PhD: Eram Rizvi, who continued in this role even after executing a flawless escape plan, and Paul Newman, who took up the baton with relish once I returned to Birmingham. Paul Thompson completed the set by sharing thesis-reading duties.

It was the H1UK extended family that brought most to my time in Germany, both in and out of the office. Of course, it helped that Hamburg was such an outstanding city to begin with. But making the DESY canteen bearable (and sometimes even enjoyable) was no small achievement. If I am to follow the family analogy to its logical conclusion, then the postdocs were surely the wise uncles. In which case, Paul Laycock and David "babys hand" South had the (occasionally unwelcome) distinction of honorary surrogate-unclehood long before they had it in fact. Other notables (more or less office by office) include Ethan Woehrling (who had been hoping for my data), Chris "genius" Wigmore, Yves Fleming, Andy Rimmer, Christian Veelken, Carl Gwilliam, Mudhahir Ismail, Matt Beckingham, Dan Traynor, Nick Malden and Andy Mehta. E&OE.

I'd also like to thank the fellow travellers I met at various summer schools for the inspiration, affirmation and confirmation, and the organisers for making it possible.

Once back in Birmingham, I was happy to find that a well-spring of surrogate friends in and around the physics department (most of my Better Friends (TM) having moved away). They all fulfilled their role admirably but special mention must go to Yves Coppens, for his uniquely Yveish encouragement, and Tamsin Moye, for treats and rides (not actually euphemisms). Of my better friends - best defined as everyone (or most everyone) who's ever passed through 10 Bournbrook Road - I'd like to give particular thanks to those who managed to make it to the Andrewcons (for the chance to relax during my final year, and for the mutually assured cheese-struction) and to assorted medics (chiefly for not batting an eyelid when I drifted in and out of their lives).

Finally, I'm hella grateful to my family for all their support, ever.